UNIVERSITÀ DELLA CALABRIA

Dottorato di Ricerca in Scienze e Tecnologie Fisiche, Chimiche e dei Materiali

XXXII CICLO

Tesi di dottorato

Optimal design and numerical modelling of imperfection sensitive shell structures

SSD ICAR/08 Scienza delle Costruzioni

Supervisore
prof. Giovanni Garcea

Dottorando
ing. Francesco Salvatore Liguori

Francesco Salvatore Liguori

Coordinatore
prof. Roberto Bartolino

Novembre 2019

Dedicated to Eulalia

ACKNOWLEDGEMENTS

I would like to express my sincere gratitude to my supervisor, Prof Giovanni Garcea. A special recognition for their collaboration is due to the rest of the research group, Dr Leonardo Leonetti, Dr Antonio Madeo and Dr Domenico Magisano. Lastly, I sincerely thank Prof Paul M. Weaver for having included me in his team during my research at University of Limerick and Dr Giovanni Zucco for his great support.

ABSTRACT

A brand-new design philosophy tends to harness the load-carrying capacity hidden beyond the onset of buckling phenomena in shell structures. However, when designing in the postbuckling range, among other effects, attention should be given at imperfection sensitivity which may generate catastrophic and unexpected consequences on the optimised structures. Therefore, what would be necessary is an optimisation strategy able to deal with the complex geometries of full-scale structures and, meanwhile, efficiently gather the complexity of their postbuckling response. The aim of this work is to meet this demand by proposing numerical methods that face the problem from different sides, namely the geometrically nonlinear description of the shell, the solution algorithm and the optimisation strategy.

As a starting point, a convenient format to describe geometrically nonlinear shell structures is identified in the solid-shell model. On the basis of this model, a discretised environment is constructed using isogeometric analysis (IGA) that, by taking advantage from the high continuity of the interpolation functions, leads to a reduced number of variables with respect to standard finite elements. Afterwards, an IGA-based multimodal Koiter's method is proposed to solve the geometrically nonlinear problem. This method meets the aforementioned requirements of efficiency, accuracy and is capable of providing information on the worst-case imperfection with no extra computational cost with respect to the analysis of a perfect structure. Additionally, a new strategy for improving the accuracy of the standard version of Koiter's algorithm in the presence of geometrical imperfections is devised. The last part of the thesis concerns the optimal design of full-scale structures undergoing buckling phenomena. In particular, the design focuses on variable angle tow laminates, namely multi-layered composites in which fibre tows can describe curvilinear paths, thereby providing great stiffness-tailoring capacity. Two optimisation strategies are proposed, both based on the use of Koiter's method to evaluate the postbuckling response. The first one makes use of a fibre path parameterisation and stochastic Monte Carlo random search as a global optimiser. The second one is based on direct stiffness modelling using lamination parameters as intermediate optimisation variables that lead to a reduction of the nonlinearity of the optimisation problem and remove the direct dependence from the number of layers.

SOMMARIO

La progettazione di strutture a guscio attualmente tende a sfruttare la capacità portante ancora disponibile dopo l'insorgere di fenomeni di buckling. Contemporaneamente però, è importante che le procedure di ottimizzazione tengano sotto controllo la sensibilità alle imperfezioni al fine di evitare l'insorgere di fenomeni potenzialmente catastrofici nella strutture ottimizzate. Di conseguenza, è di primaria importanza disporre di algoritmi di ottimizzazione che siano applicabili alle complesse geometrie che caratterizzano le strutture in scala reale e che, nel contempo, colgano la complessità della loro risposta post-critica. L'obiettivo di questo lavoro va in tale direzione, proponendo procedure numeriche che affrontino il problema nelle sue costituenti fondamentali, ossia la descrizione geometricamente nonlineare delle strutture a guscio, gli algortimi di soluzione del problema e le strategie di ottimizzazione.

In dettaglio, è stato identificato nel modello solid-shell un formato conveniente per la descrizione di strutture a guscio soggette a fenomeni di nonlinearità geometrica. È proposto un modello isogeometrico che, essendo basato su funzioni di interpolazione ad alta continuità, sia in grado di ridurre le variabili del problema rispetto ad elementi finiti tradizionali. Per valutare la risposta postcritica si ricorre ad un algoritmo multimodale di Koiter. Tale strumento rispetta i requisiti di efficienza richiesti e, nel contempo, riesce a garantire accuratezza e affidabilità nella stima dell'iniziale percorso postcritico. Inoltre, esso consente di avere informazioni sull'imperfezione peggiore senza sostanziali incrementi nel costo computazionale complessivo dell'analisi. A tal fine, è proposto un nuovo algoritmo per valutare l'effetto di imperfezioni geometriche, incrementando i livelli di accuratezza delle precedenti implementazioni. L'ultima parte del lavoro riguarda gli algoritmi di ottimizzazione. In particolare, oggetto dell'ottimizzazione sono laminati *variable angle tow*, cioè materiali compositi le cui fibre possono seguire percorsi curvilinei. Sono proposte due differenti strategie, entrambe basate sul metodo di Koiter per valutare la risposta strutturale. La prima, efficace quando il numero di variabili da ottimizzare è limitato, utilizza algoritmi stocastici, mentre la seconda usa parametri di laminazione ed è particolarmente conveniente in presenza di molte variabili da ottimizzare in quanto riduce la non convessità del problema e ne rimuove la diretta dipendenza dal numero di strati.

CONTENTS

1 INTRODUCTION

When in the forties of the previous century W. Koiter was founding the modern theory of elastic stability [1], buckling phenomena were considered as sources of catastrophic failure and a commonly accepted design philosophy dictated to preserve lightweight structures within their linear-elastic range. This was mainly due to the lack of knowledge of geometric nonlinearities that have been a key topic for the scientific community for many years [2, 3]. The research advanced and phenomena like multimodal interaction, imperfection sensitivity, branch-switching shed light to the nonlinear structural behaviour that was, let us say, mysterious until that time [4–6]. Simultaneously, the computational capability of calculators improved and so did the manufacturing technology, leading to the wide range of design possibilities the industry has got today. This should be framed in a context where the need for reducing cost come up beside the structural safety and increasing demand for lighter weight shell structures is observed in fields as structural, mechanical and, especially, aerospace engineering. Consequently, today one is facing a paradigm shift. Structures are allowed to enter the postbuckling regime during service because in that region hidden load-carrying capacity could be harnessed [7]. This mainly happens when the structure is characterised by a stable initial postbuckling behaviour and the loss in stiffness due to buckling phenomena is limited. Conversely, designers usually tend to avoid unstable postbuckling behaviours and imperfection sensitivity needs to be kept under control [8]. Actually, there are cases when instabilities are designed to happen, as it is in morphing structures [9]. The implications are huge and brought the topic of geometric nonlinearities at the centre of the scientific community again. What would be necessary is a numerical tool able to provide an optimal design of full-scale structures dealing with geometrical nonlinearities. To comply with this demand, three main points should be addressed.

The first one concerns the mechanical and numerical modelling of complex shell structural systems. Classical shell theories can be adopted to this scope [10], as well as other structural models derived from the three-dimensional continuum [11]. The use of classical shell theories for geometrically nonlinear problems suffers from the complications given by the required treatment of finite rotations. Conversely, models derived from the three-dimensional continuum as degenerated shells and solid-shells possess translational degrees of freedom only and this feature notably simplifies the formulation. Additionally, they have the advantage of allowing a three-dimensional description of the body, with increased accuracy in the modelling of connections. After the definition of the structural model, it is necessary to define a numerical strategy to discretise the continuum problem. The Finite Element Method (FEM) is the most common strategy that has been continuously improved over the years and today guarantees versatility and robustness. However, new discretisation methodologies have been proposed, such as the Particle Method, the Extended Finite Element Method (XFEM), the Virtual Element Method and the Isogeometric Analysis (IGA). Among them, IGA [12] has been enthusiastically welcomed because of the many advantages provided over the traditional FEM, specifically in the context of geometrically nonlinear structures. The main idea of the IGA technique consists of building a discretised structural model that shares the interpolation functions of the unknown fields with the Computer Aided Design (CAD) model. Such functions are Non Rational B-Splines (NURBS), characterised by accuracy in representing complex shapes and high continuity. If the integration between structural analysis and CAD gives advantages in terms of saving modelling time, the high continuity guarantee computational efficiency. In fact, by exploiting the high continuity, a low number of control points govern the interpolation and, consequently, the number of variables reduces with respect to standard interpolations. Let us now reconsider geometric nonlinearities in the elastic range. The problem is characterised by high continuity of the displacement fields and of stresses and strains and, then, the use of IGA within this context seems to be promising [13]. However, there are still issues in IGA it is needed to deal with, such as locking phenomena, time-consuming integration procedures and difficulties in formulating efficient mixed formulations required to ensure robustness at the nonlinear analysis [14].

Moving on to the second point required by a satisfactory design strategy, one arrives at the solution method for solving the nonlinear system of equilibrium equations. First of all, one desires that it is accurate up to the design level. It can be an equilibrium configuration far from the initial state, if one is dealing with multistable structures, or the initial postbuckling behaviour, if one is interested in standard structural applications. Another important requirement is its relative efficiency, because the analysis is likely to be repeated many times until an optimal solution is found. Lastly, the method should be able to include information about the effect of unavoidable uncertainties affecting an actual structural problem. It is well-known, indeed, how even small imperfections can substantially modify the structural behaviour and, consequently, ignoring them could produce a naive optimised structure that exhibits the desired structural response only if perfectly manufactured [6].

Finally, a third point one needs to address is the optimisation strategy used to obtain an optimal design. Its choice depends on the nature of the variables of the optimisation and we end up into a heterogeneous space made up of novel materials and manufacturing technologies. Within this area we can found composite materials, toward which high attention is given today. Together with standard multilayered carbon fibre composites it is looked at new technologies, like Variable Angle Tow (VAT), carbon nanotubes, variable thickness laminates, bio composite materials. For each of them, a proper strategy should be selected, but what is commonly needed is good convergence properties, efficiency, robustness and the ability to include constraints of different natures.

The points made above draw the desired features of an optimal design strategy of geometrically nonlinear structures. The purpose of this work consists in trying to provide an answer, such that it can represent a small fraction of the research that will make the postbuckling optimisation a standard in the nearest future. All three discussed aspects will be addressed. Hereafter, the main contributions of this work are presented. We identify in the solid-shell concept a convenient format to construct an efficient mechanical model to be discretised using IGA. NURBS functions are employed to interpolate geometry and displacement fields and a peculiar description for the stresses is chosen following a strategy named Mixed Integration Point (MIP), necessary to solve a well-known problem known as extrapolation locking [15, 16]. Green-Lagrange strain measure and Total Lagrangian description are adopted [17]. Together with the mixed description of solid-shell IGA, they guarantee a cubic dependence of the strain energy from the unknown variables. On the basis of this discretisation, the geometrically nonlinear analysis is performed by developing a reduced order model inspired by Koiter's theory of elastic stability [1, 3], which meets the requirements of efficiency and accuracy. A strategy to account for geometrical imperfections within Koiter's analysis is developed. It gives us the chance to detect the worst-case imperfection shape with basically no extra-cost of the overall geometrically nonlinear analysis. Tuning up the nonlinear analysis of imperfection sensitive shells using the IGA based Koiter's method is a crucial step for the development of an optimisation framework. In particular, we focus on the selection of the best stacking sequence and ply orientations of composite structures using both non-conventional laminates and VAT. Two strategies are proposed, the first one is based on stochastic simulations and the second one on lamination parameters and a gradient-based optimiser.

The work is structured in chapters. Chapter 2 presents the solid-shell model and the advantages of its use in the context of geometrically nonlinear structures are described. Chapter 3 regards the solution methods of the nonlinear problem, focusing on the arc-length strategy and Koiter's method for solid-shell. In chapter 4 we present the solid-shell IGA model. Results are given regarding classical benchmark problems to assess the effectiveness of the remedies against locking phenomena. Shell obstacle courses are besides analysed to highlight the advantages of the proposed IGA framework within arc-length methods and, finally, the robustness of Koiter's method is tested. In chapter 5 a new formula for evaluating the effect of geometrical imperfections within Koiter's analysis is presented and validated by numerical results. The optimisation strategies are presented in chapter 6. Afterwards, the approach is tested on a series of optimisation problems, among which the optimal design of a full-scale VAT composite wingbox. Eventually, conclusions are drawn in chapter 7.

2 MODELLING A SHELL STRUCTURE

Shell structures are commonly employed in a wide range of engineering applications. Especially due to the flexibility of composite materials, shells are nowadays preferred as primary structural components in the most heavily loaded parts, as happens in new generation wings [18]. The pursue of saving weight leads to optimised structures whose thickness is significantly smaller than the other dimensions. This results in a spread of slender structures that exhibit large deformations while the material still behaves linearly elastic. To simulate this mechanical behaviour one can make use of many structural models. Chronologically, the first shell theory to provide good results is the Kirchhoff-Love model. This model is based on a kinematics described by displacements and their first-order derivatives and neglects the effect of shear deformations. The classical lamination theory shares with the Kirchhoff-Love model many hypotheses and is employed to describe laminated shells. Even if the model is successfully employed to obtain semi-analytical solutions [19], it is not frequently used in discretised problems due to the C^1 continuity over the domain required by the weak formulation. The Mindlin-Reissner model has been then often preferred also when the Kirchhoff hypothesis are likely to be verified. Its kinematics is described by mid-plane displacements and rotations and laminate composites can be described using the first order shear deformation theory [10]. The main difficulty in using Mindlin shells in large deformation problems resides in the need of handling finite rotations. For this reason, alternative formulations have been investigated. Among them is the solid-shell model, that consists in a solid model able to obtain the shell solution by a relatively simple interpolation through the thickness. Being based on a solid model, this strategy uses displacement degrees of freedom only and the simple Green-Lagrange strain measure can be adopted [17]. Displacements and rotations of the Mindlin model are replaced with displacements of the top and bottom surfaces in solid-shells. Because the Green-Lagrange measure establishes a quadratic relation between displacements and strains, when displacements and stresses are chosen as independent variables the strain energy is a cubic polynomial. This aspect has positive implications on the easiness of the operators involved and on the accuracy and efficiency of a geometrically nonlinear formulation, how will be clarified with the advancement of the chapters. Ultimately, the aforementioned advantages make the use of solid-shell models of great attractiveness for the purposes of this work. Hereafter, insights are given on the solid-shell model and a discrete formulation is presented.

2.1 SOLID-SHELL MODEL

This section is aimed at describing the solid-shell model, which has been identified as a convenient format for the geometrically nonlinear analysis. Starting from a nonlinear three-dimensional continuum which uses Green-Lagrange strain measure, the kinematics of solid-shell is derived by through-the-thickness interpolation. Afterwards, generalised strain and stresses are identified, leading to a description in terms of stress resultants similar to that given by classical shells. Defining a homogeneised constitutive matrix allows us to write the strain and complementary energy of the system. Finally, a discretised formulation is obtained.

2.1.1 Kinematics of solid-shells

Convective curvilinear shell coordinates $\boldsymbol{\zeta} = [\zeta_1, \zeta_2, \zeta_3]$ are employed, with (ζ_1, ζ_2) representing middle surface coordinates and $\zeta_3 \in [-1, 1]$ being aligned with the shell thickness direction, cf Fig. 2.1. The position of material points $\mathbf{x}(\boldsymbol{\zeta})$ in the current configuration is given in terms of their position vector $\mathbf{X}(\boldsymbol{\zeta})$ in the reference configuration and the displacement $\mathbf{d}(\boldsymbol{\zeta})$, namely

$$\mathbf{x}(\boldsymbol{\zeta}) = \mathbf{X}(\boldsymbol{\zeta}) + \mathbf{d}(\boldsymbol{\zeta}). \tag{2.1}$$

The covariant basis vectors in the undeformed and deformed configuration are obtained from the corresponding partial derivatives of the position vectors $\mathbf{X}$ and $\mathbf{x}$, respectively

$$\mathbf{G}_i = \mathbf{X}_{,i}\,, \qquad \mathbf{g}_i = \mathbf{x}_{,i} = \mathbf{G}_i + \mathbf{d}_{,i} \qquad \text{with } \; i = 1,2,3\,, \tag{2.2}$$

where $()_{,i}$ denotes the partial derivative with respect to ith components of $\boldsymbol{\zeta}$. The contravariant basis vectors follow from the dual basis condition

$$\mathbf{g}_i \cdot \mathbf{g}^j = \mathbf{G}_i \cdot \mathbf{G}^j = \delta_i^j \qquad \text{with } \; i = 1,2,3$$

where δ_i^j is one if $i = j$, zero otherwise. The metric coefficients are

$$g_{ij} = \mathbf{g}_i \cdot \mathbf{g}_j, \quad G_{ij} = \mathbf{G}_i \cdot \mathbf{G}_j.$$

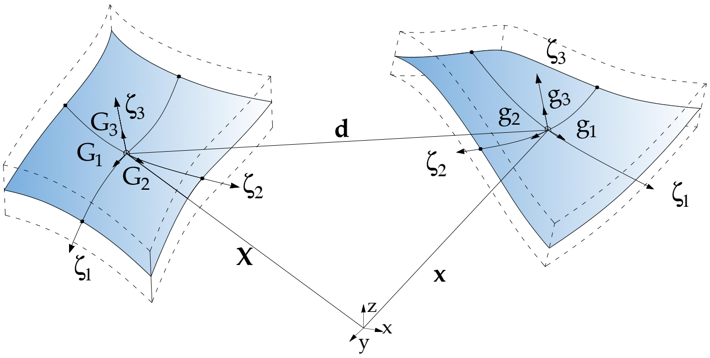

Figure 2.1: Undeformed and deformed shell geometry.

The motion of material points from the initial reference configuration to the current configuration is described by the deformation map $\mathbf{F} : \mathbf{x} \to \mathbf{X}$

$$\mathbf{F} = \frac{\partial \mathbf{x}}{\partial \mathbf{X}} = \mathbf{g}_i \otimes \mathbf{G}^i. \tag{2.3}$$

Using the deformation gradient in Eq.(2.3) and the metric tensor G_{ij}, the Green-Lagrange strain tensor can be expressed as

$$\mathbf{E} = \frac{1}{2}\left(\mathbf{F}^T\,\mathbf{F} - \mathbf{I}\right) = \bar{E}_{ij}\,\mathbf{G}^i \otimes \mathbf{G}^j \tag{2.4}$$

where

$$\bar{E}_{ij} = \frac{1}{2}\left(\mathbf{X}_{,i} \cdot \mathbf{d}_{,j} + \mathbf{d}_{,i} \cdot \mathbf{X}_{,j} + \mathbf{d}_{,i} \cdot \mathbf{d}_{,j}\,\right),$$

and $(\cdot)$ means scalar product.

The solid-shell concept consists in identifying a preferential direction along which assuming a simple description of the three-dimensional continuum. Accordingly, a linear through-the-thickness interpolation is assumed and the position vector is expressed as

$$\mathbf{X} = \frac{1}{2}\left(\mathbf{X}[\zeta_+] + \mathbf{X}[\zeta_-]\right) + \frac{\zeta_3}{2}\left(\mathbf{X}[\zeta_+] - \mathbf{X}[\zeta_-]\right), \tag{2.5}$$

where

$$\zeta_+ = [\zeta_1, \zeta_2, 1], \quad \zeta_- = [\zeta_1, \zeta_2, -1].$$

express respectively the top and bottom layer of the shell. Analogously, the displacement field is described as

$$\mathbf{d} = \frac{1}{2}\left(\mathbf{d}[\zeta_+] + \mathbf{d}[\zeta_-]\right) + \frac{\zeta_3}{2}\left(\mathbf{d}[\zeta_+] - \mathbf{d}[\zeta_-]\right). \tag{2.6}$$

Collecting the covariant strain components in Eq.(2.4) in the vector

$$\bar{\mathbf{E}} = \left[\bar{E}_{11}, \bar{E}_{22}, 2\bar{E}_{12}, \bar{E}_{33}, 2\bar{E}_{23}, 2\bar{E}_{13}\right]^T,$$

it can be linearised with respect to ζ_3 as

$$\bar{\mathbf{E}} \approx \begin{bmatrix} \bar{\mathbf{e}}[\zeta_0] + \zeta_3\, \bar{\chi}[\zeta_0] \\ \bar{E}_{33}[\zeta_0] \\ \bar{\gamma}[\zeta_0] \end{bmatrix}, \tag{2.7}$$

where

$$\begin{aligned} \bar{\mathbf{e}}[\zeta_0] &\equiv \begin{bmatrix} \bar{E}_{11}[\zeta_0] \\ \bar{E}_{22}[\zeta_0] \\ 2\bar{E}_{12}[\zeta_0] \end{bmatrix}, \quad \bar{\chi}[\zeta_0] \equiv \begin{bmatrix} \bar{E}_{11,3}[\zeta_0] \\ \bar{E}_{22,3}[\zeta_0] \\ 2\bar{E}_{12,3}[\zeta_0] \end{bmatrix}, \\ \bar{\gamma}[\zeta_0] &\equiv \begin{bmatrix} 2\bar{E}_{23}[\zeta_0] \\ 2\bar{E}_{13}[\zeta_0] \end{bmatrix} \end{aligned} \tag{2.8}$$

with $\zeta_0 = [\zeta_1, \zeta_2, 0]$ identifying the shell mid-surface. The covariant generalised strains are collected in the vector $\bar{\varepsilon}[\zeta_0] \equiv \left[\bar{\mathbf{e}}, \bar{E}_{33}, \bar{\chi}, \bar{\gamma}\right]^T$.

2.1.2 Generalised stresses

The generalised stress components, once the kinematic model is assumed, are automatically given by assuring the invariance of the internal work. Introducing the contravariant stress components

$$\bar{\mathbf{S}} \equiv \left[\bar{S}_{11}, \bar{S}_{22}, \bar{S}_{12}, \bar{S}_{33}, \bar{S}_{23}, \bar{S}_{13}\right]^T,$$

and denoting with V the volume of the solid and Ω the middle plane area, the strain work $\mathcal{W}$ can be expressed as

$$\begin{aligned} \mathcal{W} &= \int_V \bar{\mathbf{S}}^T \bar{\mathbf{E}}\, dV = \int_\Omega \left(\bar{\mathcal{N}}^T \bar{\mathbf{e}} + \bar{\mathcal{M}}^T \bar{\chi} + \bar{s}_{33} \bar{E}_{33} + \bar{\mathcal{T}}^T \bar{\gamma}\right) d\Omega \\ &= \int_\Omega \bar{\sigma}^T \bar{\varepsilon}\, d\Omega, \end{aligned} \tag{2.9}$$

where the generalised stresses are $\bar{\boldsymbol{\sigma}} \equiv \left[\bar{\mathcal{N}}, \bar{s}_{33}, \bar{\mathcal{M}}, \bar{\mathcal{T}}\right]^T$ and can be consequently evaluated as

$$\begin{aligned} \bar{\mathcal{N}} &\equiv \frac{1}{2}\int_{-1}^{1} \bar{\boldsymbol{\sigma}}_p \, d\zeta_3 \qquad & \bar{\mathcal{M}} &\equiv \frac{1}{2}\int_{-1}^{1} \zeta \bar{\boldsymbol{\sigma}}_p \, d\zeta_3 \\ \bar{s}_{\zeta\zeta} &\equiv \frac{1}{2}\int_{-1}^{1} \bar{S}_{\zeta\zeta} d\zeta_3 \qquad & \bar{\mathcal{T}} &\equiv \frac{1}{2}\int_{-1}^{1} \bar{\boldsymbol{\tau}} d\zeta_3 \end{aligned} \tag{2.10}$$

2.1.3 Mapping between parametric and physical domains

The relation between the contravariant stresses and covariant strains in tensor notation and the corresponding Cartesian ones is

$$\mathsf{E} = \mathbf{J}^{-1}\bar{\mathsf{E}}\mathbf{J}^{-T} \quad \text{and} \quad \mathsf{S} = \mathbf{J}^{T}\bar{\mathsf{S}}\mathbf{J}, \tag{2.11}$$

that in Voigt notation can be written as

$$\mathbf{E} = \mathbf{T}_E \bar{\mathbf{E}} \quad \text{and} \quad \mathbf{S} = \mathbf{T}_S \bar{\mathbf{S}} \tag{2.12}$$

with $\mathbf{T}_S = \mathbf{T}_E^{-T}$.

From Eq. (2.5), $\mathbf{J} = \mathbf{J}_0[\zeta_0] + \zeta_3 \mathbf{J}_n[\zeta_0]$ and its inverse can be linearised with respect to ζ_3 as

$$\mathbf{J}^{-1}[\zeta_0] = \mathbf{J}_0^{-1}[\zeta_0] + \zeta_3 \mathbf{J}_n^{-1}[\zeta_0] \tag{2.13}$$

where it is possible to obtain $\mathbf{J}_n^{-1}$ by satisfying the condition $\mathbf{J}\mathbf{J}^{-1} = \mathbf{I}$ up to the first order in ζ_3, namely

$$\mathbf{J}_n^{-1} = \mathbf{J}_0^{-1}\mathbf{J}_n\mathbf{J}_0^{-1}.$$

Substituting Eq.(2.13) in Eq.(2.12) and maintaining only the linear terms in ζ_3 we obtain the linearised expression of $\mathbf{T}_E = \mathbf{T}_{E0} + \zeta_3 \mathbf{T}_{En}$. In particular, letting

$$\mathbf{T}_{E0} = \begin{bmatrix} \mathbf{T}^0_{ee} & \mathbf{T}^0_{e\zeta} & \mathbf{T}^0_{e\gamma} \\ \mathbf{T}^0_{\zeta e} & T^0_{\zeta\zeta} & \mathbf{T}^0_{\zeta\gamma} \\ \mathbf{T}^0_{\gamma e} & \mathbf{T}^0_{\gamma\zeta} & \mathbf{T}^0_{\gamma\gamma} \end{bmatrix}, \qquad \mathbf{T}_{En} = \begin{bmatrix} \mathbf{T}^n_{ee} & \mathbf{T}^n_{e\zeta} & \mathbf{T}^n_{e\gamma} \\ \mathbf{T}^n_{\zeta e} & T^n_{\zeta\zeta} & \mathbf{T}^n_{\zeta\gamma} \\ \mathbf{T}^n_{\gamma e} & \mathbf{T}^n_{\gamma\zeta} & \mathbf{T}^n_{\gamma\gamma} \end{bmatrix}$$

we have, maintaining the linear terms in ζ_3 only,

$$\mathbf{E} = \mathbf{T}_E \bar{\mathbf{E}} \approx \begin{bmatrix} \boldsymbol{e} + \zeta_3 \boldsymbol{\chi} \\ E_{\zeta\zeta} \\ \boldsymbol{\gamma} \end{bmatrix}. \tag{2.14}$$

Eq. (2.12) can be expressed in terms of the generalised strains as

$$\boldsymbol{\varepsilon} = \mathbf{T}_{\epsilon}\,\bar{\boldsymbol{\varepsilon}} \tag{2.15}$$

where $\boldsymbol{\varepsilon} = [\boldsymbol{e}, E_{\zeta\zeta}, \boldsymbol{\chi}, \boldsymbol{\gamma}]^{\mathsf{T}}$ and

$$\mathbf{T}_{\epsilon} = \begin{bmatrix} \mathbf{T}^{0}_{ee} & \mathbf{T}^{0}_{e\zeta} & 0_{3\times 3} & \mathbf{T}^{0}_{e\gamma} \\ \mathbf{T}^{0}_{\zeta e} & T^{0}_{\zeta\zeta} & 0_{1\times 3} & \mathbf{T}^{0}_{\zeta\gamma} \\ \mathbf{T}^{n}_{ee} & \mathbf{T}^{n}_{e\zeta} & \mathbf{T}^{0}_{ee} & \mathbf{T}^{n}_{e\gamma} \\ \mathbf{T}^{0}_{\gamma e} & \mathbf{T}^{0}_{\gamma\zeta} & 0_{2\times 3} & \mathbf{T}^{0}_{\gamma\gamma} \end{bmatrix},$$

and in terms of generalised stress as

$$\boldsymbol{\sigma} = \mathbf{T}_{\epsilon}^{-\mathsf{T}}\,\bar{\boldsymbol{\sigma}}, \tag{2.16}$$

where $\boldsymbol{\sigma} \equiv \left[\mathcal{N}, s_{33}, \mathcal{M}, \mathcal{T}\right]^{\mathsf{T}}$ follows from the energy equivalence

$$\int_{\Omega} \bar{\boldsymbol{\sigma}}^{\mathsf{T}}\,\bar{\boldsymbol{\varepsilon}}\,d\Omega = \int_{\Omega} \boldsymbol{\sigma}^{\mathsf{T}}\,\boldsymbol{\varepsilon}\,d\Omega.$$

2.1.4 Homogenised constitutive matrix

Multi-layered composites can be modelled using layer-wise interpolations [20, 21] which provide accurate inter-laminar stress reconstructions or homogenisation techniques usually more efficient and suitable for predicting global behaviours accurately. When a linear through-the-thickness interpolation is adopted, the achieved accuracy is that provided by first order shear deformation theory.

When a linear through-the-thickness interpolation is adopted, a generalised constitutive law of the multi-layered composite can be obtained following [11, 17]. It consists of a homogenization technique which imposes a constant with ζ_3 stress S_{33} in order to eliminate thickness locking and obtain an accurate prediction of stresses and displacements. The material law of the generic lamina, assumed to be orthotropic elastic, can be conveniently expressed in a suitable reference system $\{\boldsymbol{e}_1, \boldsymbol{e}_2, \boldsymbol{e}_3\}$ according to the fibre direction as

$$\hat{\mathbf{S}} = \hat{\mathbf{C}}\hat{\mathbf{E}} \quad \text{with} \quad \hat{\mathbf{C}} = \begin{bmatrix} \hat{\mathbf{C}}_{pp} & \hat{\mathbf{C}}_{p3} & 0 \\ \hat{\mathbf{C}}^{\mathsf{T}}_{p3} & \hat{C}_{33} & 0 \\ 0 & 0 & \hat{\mathbf{C}}_{t} \end{bmatrix} \tag{2.17}$$

which furnishes, exploiting the decoupling of the transverse shear components, the inverse law as

$$\begin{bmatrix}\hat{\mathbf{E}}_p \\ \hat{E}_{33}\end{bmatrix} = \begin{bmatrix}\hat{\mathbf{F}}_{pp} & \hat{\mathbf{F}}_{p3} \\ \hat{\mathbf{F}}_{p3}^T & \hat{F}_{33}\end{bmatrix}\begin{bmatrix}\hat{\mathbf{S}}_p \\ \hat{S}_{33}\end{bmatrix} \tag{2.18}$$

where symbol $(\hat{\ })$ denotes Cartesian components expressed with respect to $\{\mathbf{e}_1, \mathbf{e}_2, \mathbf{e}_3\}$ with $\mathbf{e}_3$ aligned to ζ_3 and $\hat{\mathbf{E}}_p = \hat{\mathbf{e}} + \zeta_3\, \hat{\boldsymbol{\chi}}$. Eq.(2.18) can be rewritten as

$$\begin{aligned}\hat{\mathbf{S}}_p &= \mathbf{S}\hat{\mathbf{E}}_p + \mathbf{D}\hat{S}_{33} \\ \hat{E}_{33} &= -\mathbf{D}^T\hat{\mathbf{E}}_p + R\hat{S}_{33}\end{aligned} \quad \text{with} \quad \begin{cases} R = \hat{F}_{33} + \hat{\mathbf{F}}_{p3}^T\mathbf{D} \\ \mathbf{D} = -(\hat{\mathbf{F}}_{pp})^{-1}\hat{\mathbf{F}}_{p3} \\ \mathbf{S} = (\hat{\mathbf{F}}_{pp})^{-1}. \end{cases}$$

The constitutive law in terms of the quantities $\hat{\mathcal{N}}$ and $\hat{\mathcal{M}}$ is then obtained, integrating along ζ_3 and imposing a constant with ζ_3 stress $\hat{S}_{33} = \hat{s}_{33}$, as

$$\begin{aligned}\begin{bmatrix}\hat{\mathcal{N}} \\ \hat{E}_{33} \\ \hat{\mathcal{M}}\end{bmatrix} &= \frac{1}{2}\int_{-1}^{1}\begin{bmatrix}\mathbf{S} & \mathbf{D} & \zeta_3\mathbf{S} \\ -\mathbf{D} & R & -\zeta_3\mathbf{D} \\ \zeta_3\mathbf{S} & \zeta_3\mathbf{D} & \zeta_3^2\mathbf{S}\end{bmatrix} d\zeta \begin{bmatrix}\hat{\mathbf{e}} \\ \hat{s}_{33} \\ \hat{\boldsymbol{\chi}}\end{bmatrix} \\ &= \begin{bmatrix}\mathbf{S}_0 & \mathbf{D}_0 & \mathbf{S}_1 \\ -\mathbf{D}_0 & R_0 & \mathbf{D}_1 \\ \mathbf{S}_1 & \mathbf{D}_1 & \mathbf{S}_2\end{bmatrix}\begin{bmatrix}\hat{\mathbf{e}} \\ \hat{s}_{33} \\ \hat{\boldsymbol{\chi}}\end{bmatrix}\end{aligned}$$

which furnishes the thickness locking free generalised constitutive law

$$\hat{\boldsymbol{\sigma}}[\zeta_0] = \hat{\mathbf{C}}_\epsilon\, \hat{\boldsymbol{\varepsilon}}[\zeta_0] \tag{2.19}$$

where

$$\hat{\mathbf{C}}_\epsilon \equiv \begin{bmatrix}\mathbf{S}_0 + \mathbf{D}_0\mathbf{D}_0^T/R_0 & \mathbf{D}_0/R_0 & \mathbf{S}_1 + \mathbf{D}_0\mathbf{D}_1^T/R_0 & \mathbf{0} \\ \mathbf{D}_0^T/R_0 & 1/R_0 & \mathbf{D}_1^T/R_0 & \mathbf{0} \\ (\mathbf{S}_1 + \mathbf{D}_0\mathbf{D}_1^T/R_0)^T & \mathbf{D}_1/R_0 & \mathbf{S}_2 + \mathbf{D}_1\mathbf{D}_1^T/R_0 & \mathbf{0} \\ \mathbf{0} & \mathbf{0} & \mathbf{0} & \hat{\mathbf{C}}_{t0}\end{bmatrix}$$

and

$$\hat{\mathbf{C}}_{t0} = \int_{-1}^{1}\hat{\mathbf{C}}_t\, d\zeta_3.$$

The modified generalised constitutive matrix in the global system $\{X, Y, Z\}$ is obtained as $\mathbf{C} = \mathbf{R}_\epsilon^T\hat{\mathbf{C}}_\epsilon\mathbf{R}_\epsilon$ with $\mathbf{R}_\epsilon$ a suitable rotation matrix.

2.1.5 Energy

The mixed energy of the system can be expressed as

$$\Phi = \int_\Omega \boldsymbol{\sigma}^T \boldsymbol{\varepsilon} d\Omega - \frac{1}{2}\int_\Omega \boldsymbol{\sigma}^T \mathbf{C}^{-1} \boldsymbol{\sigma} d\Omega, \tag{2.20}$$

If one assumes as independent variables of the nonlinear problem displacements and stresses, it is possible to clearly notice from Eq.(2.20) how the the mixed strain energy has a cubic dependence only from them. Conversely, a displacement-based formulation, that assumes only displacements as variables and for which the energy can be written as

$$\Phi = \frac{1}{2}\int_\Omega \boldsymbol{\varepsilon}^T \mathbf{C} \boldsymbol{\varepsilon} d\Omega, \tag{2.21}$$

is a fourth-order polynomial.

2.1.6 Discretised solid-shell model

The domain can be discretised in elements having area Ω_e, obtaining the following expression for the integrals above

$$\Phi = \sum_{e=1}^{ne} \Phi_e = \sum_{e=1}^{ne} \int_{\Omega_e} \left(\boldsymbol{\sigma}^T \boldsymbol{\varepsilon} - \frac{1}{2} \boldsymbol{\sigma}^T \mathbf{C}^{-1} \boldsymbol{\sigma} \right) d\Omega_e. \tag{2.22}$$

The geometry is interpolated as

$$\mathbf{X}[\zeta] = \mathbf{N}_d[\zeta]\mathbf{X}_e \tag{2.23}$$

where $\mathbf{d}_e = [\mathbf{d}_{0e}, \mathbf{d}_{ne}]$ collects the geometrical discrete variables. The matrix $\mathbf{N}_p[\zeta]$ collects the interpolation functions of the middle surface coordinates only. The displacement fields are as

$$\mathbf{d}[\zeta] = \mathbf{N}_d[\zeta]\mathbf{d}_e \tag{2.24}$$

where $\mathbf{X}_e = [\mathbf{X}_{0e}, \mathbf{X}_{ne}]$ collects the discrete variables for displacements related to the eth element. Analogously, the stresses are interpolated $\mathbf{N}_s[\zeta]$ as

$$\boldsymbol{\sigma}[\zeta] = \mathbf{N}_s[\zeta]\boldsymbol{\beta}_e \tag{2.25}$$

where $\boldsymbol{\beta}_e$ collects the discrete stresses.

The Green-Lagrange covariant strain components in Eq.(2.4), exploiting Eq.(2.23) and Eq.(2.24), become

$$\bar{\mathbf{E}} = \left(\mathcal{L}[\zeta] + \frac{1}{2}\mathcal{Q}[\zeta, \mathbf{d}_e]\right)\mathbf{d}_e, \tag{2.26}$$

where $\mathcal{L}[\zeta] \equiv \mathcal{Q}[\zeta, \mathbf{X}_e]$ and $\mathcal{Q}[\zeta, \mathbf{d}_e]$ has a linear dependence from $\mathbf{d}_e$, namely

$$\mathcal{Q}[\zeta, \mathbf{d}_e] \equiv \begin{bmatrix} \mathbf{d}_e^T \mathbf{N}_{d,\xi}^T \mathbf{N}_{d,\xi} \\ \mathbf{d}_e^T \mathbf{N}_{d,\eta}^T \mathbf{N}_{d,\eta} \\ \mathbf{d}_e^T (\mathbf{N}_{d,\xi}^T \mathbf{N}_{d,\eta} + \mathbf{N}_{d,\eta}^T \mathbf{N}_{d,\xi}) \\ \mathbf{d}_e^T \mathbf{N}_{d,\zeta}^T \mathbf{N}_{d,\zeta} \\ \mathbf{d}_e^T (\mathbf{N}_{d,\zeta}^T \mathbf{N}_{d,\eta} + \mathbf{N}_{d,\eta}^T \mathbf{N}_{d,\zeta}) \\ \mathbf{d}_e^T (\mathbf{N}_{d,\xi}^T \mathbf{N}_{d,\zeta} + \mathbf{N}_{d,\zeta}^T \mathbf{N}_{d,\xi}) \end{bmatrix}. \tag{2.27}$$

The elemental mixed energy becomes

$$\begin{aligned} \Phi_e =& \int_{\Omega_e} \left(\boldsymbol{\sigma}[\boldsymbol{\beta}_e]^T \boldsymbol{\varepsilon}[\mathbf{d}_e] - \frac{1}{2}\boldsymbol{\sigma}[\boldsymbol{\beta}_e]^T \mathbf{C}^{-1} \boldsymbol{\sigma}[\boldsymbol{\beta}_e]\right) d\Omega_e \\ =& \boldsymbol{\beta}_e^T \left(\mathbf{L}_e + \frac{1}{2}\mathbf{Q}_e[\mathbf{d}_e]\right)\mathbf{d}_e - \frac{1}{2}\boldsymbol{\beta}_e^T \mathbf{H}_e \boldsymbol{\beta}_e \end{aligned} \tag{2.28}$$

where

$$\begin{aligned} \mathbf{H}_e =& \int_{\Omega_e} \mathbf{N}_s \mathbf{T}_s^T \mathbf{C}^{-1} \mathbf{T}_s \mathbf{N}_s d\Omega_e \\ \mathbf{L}_e =& \int_{\Omega_e} \mathbf{N}_s^T \mathcal{L}[\zeta] d\Omega_e \\ \mathbf{Q}_e =& \int_{\Omega_e} \mathbf{N}_s^T \mathcal{Q}[\zeta, \mathbf{d}_{(k)}[\zeta]] d\Omega_e. \end{aligned}$$

Conversely, the discretised matrix for a displacement-based formulation is

$$\begin{aligned} \Phi_e =& \int_{\Omega_e} \boldsymbol{\varepsilon}[\mathbf{d}_e]^T \mathbf{C} \boldsymbol{\varepsilon}[\mathbf{d}_e] d\Omega_e \\ =& \mathbf{d}_e^T \left(\mathbf{L}_e + \frac{1}{2}\mathbf{Q}_e[\mathbf{d}_e]\right)^T \mathbf{H}_e^{-1} \left(\mathbf{L}_e + \frac{1}{2}\mathbf{Q}_e[\mathbf{d}_e]\right)\mathbf{d}_e. \end{aligned} \tag{2.29}$$

In this case, the stresses are not independent variables, but are evaluated using the constitutive relation in Eq.(2.19).

3 SOLUTION STRATEGIES

This chapter concerns the strategies to solve the geometrically nonlinear problem. Two methods are identified, namely path-following and asymptotic techniques. Path-following methods aim at drawing the equilibrium path step-by step. Their main advantage is represented by the possibility of exactly evaluate a set of equilibrium points within a given tolerance. In the presence of multiple branches of the equilibrium manifold, a standard path-following strategy will follow one them, depending from the step-size and from the imperfections on the structural model. Obviously, there is no guarantee that the evaluated equilibrium path is the worst one, in terms of safety or design requirements. As well it is not possible to guarantee that the real structure will follow that path because of the presence of unavoidable imperfections. An alternative strategy is offered by generalised path-following methods [22–24] that include in the nonlinear problem an additional set of nonlinear equilibrium equations to explore the entire equilibrium manifold. The result is an interesting strategy that gives a wider information on the structural behaviour even if at an increased computational cost and overall complexity. The computational cost itself is the main issue for path-following strategies and the reason why they are not frequently employed in contexts that require many analyses to be executed. This is the case, for instance, of imperfection sensitivity analyses and postbuckling optimisation. In such cases an alternative is represented by asymptotic methods. Such methodologies are based on asymptotic expansions of the equilibrium condition, that is valid for the estimate of the initial postbuckling behaviour. Many of them [10, 14, 17, 25–32] are inspired from Koiter's theory of elastic stability [1] of which represent extensions and generalisations. In particular, interesting proposals are the FE implementations of Koiter's theory [2, 15, 33–41], that combine the flexibility of FE discretisations with the computational efficiency of asymptotic expansions. Among them, an accurate FE implementation of Koiter's algorithm has been proposed by Casciaro [3]. It consists of the construction of a reduced model, in which the FE model is replaced by its second order asymptotic expansion using the initial path tangent, m buckling modes and the corresponding second order modes, named quadratic correctives. In this way, once the reduced model is built, the equilibrium path of the structure can be obtained by solving the non-linear reduced system of m equations in $m+1$ unknowns, which represent the modal amplitudes and the load factor. The coefficients of the reduced system are evaluated using strain energy variations up to the 4rd order. Shell structures can require a very large number of FE DOFs to avoid significant discretisation errors, while m is usually at most a few tens. The convenience of the method with respect to the standard path-following strategy is evident.

Since its first implementations, [33, 42, 43], the method and has been continuously enhanced in terms of both accuracy and computational efficiency. In particular, a mixed (stress-displacement) formulation has been proved to be necessary in order to avoid a locking phenomenon in the evaluation of the coefficients of the reduced system [5, 42–45] and to make the asymptotic expansion accurate for a wider range [14, 15]. Geometrically exact shells and beams [46, 47] or corotational approaches [29, 48] have been proposed to achieve structural model objectivity. Both strategies make explicit use of the rotation tensor and its highly non-linear representation. Alternatively, the method has been implemented exploiting the non-linear Cauchy continuum based on a Green strain measure [14, 17]. In this way the mixed strain energy has a third order polynomial dependence on the FE DOFs with the zeroing of all the fourth order strain energy variations. The resulting asymptotic formulation appears accurate, efficient and simple.

Koiter's method provides an additional result that is of paramount importance. In fact, it allows to evaluate the effect of imperfections by a-posteriori adding a scalar term to the reduced model. In this way, the reduced order model, whose construction represents the time consuming part of the analysis, is conducted one and for all for the structure without imperfections. Afterwards, the imperfection term, whose evaluation is computationally inexpensive, can be added to the reduced order equilibrium equations. In this way, the effect of an extremely large number of imperfections can be analysed at the time of a single analysis, with important implications. The worst-shape imperfection can be readily detected , for instance by employing Monte Carlo random search [8].

After the analysis framework is drawn, the arc-length method and Koiter's method for mixed soli-shells are presented in the following sections.

3.1 NONLINEAR ANALYSIS FRAMEWORK

The equilibrium of slender hyperelastic structures subject to conservative loads $f[\lambda]$ proportionally increasing with the amplifier factor λ is expressed by the virtual work equation

$$\Phi[u]'\,\delta u - \lambda f\,\delta u = 0 \quad , \quad u \in \mathcal{U}\,,\ \delta u \in \mathcal{T} \tag{3.1}$$

where $u \in \mathcal{U}$ is the field of configuration variables, $\Phi[u]$ denotes the strain energy, $\mathcal{T}$ is the tangent space of $\mathcal{U}$ at u and a prime is used to express the Fréchet derivative with respect to u. $\mathcal{U}$ is a linear manifold so that its tangent space $\mathcal{T}$ is independent of u. The discrete counterpart of Eq.(3.1) is

$$\mathbf{r}[\mathbf{u},\lambda] \equiv \mathbf{s}[\mathbf{u}] - \lambda\,\mathbf{f} = \mathbf{0}, \quad \text{with} \quad \begin{cases} \mathbf{s}^T\delta\mathbf{u} \equiv \Phi'[u]\delta u \\ \mathbf{f}^T\delta\mathbf{u} \equiv f\,\delta u \end{cases} \tag{3.2}$$

where $\mathbf{r} : \mathbb{R}^{N+1} \to \mathbb{R}^N$ is a nonlinear vectorial function of the vector $\mathbf{z} \equiv \{\mathbf{u}, \lambda\} \in \mathbb{R}^{N+1}$, collecting the configuration $\mathbf{u} \in \mathbb{R}^N$ and the load multiplier $\lambda \in \mathbb{R}$, $\mathbf{s}[\mathbf{u}]$ is the *internal force vector* and $\mathbf{f}$ the *reference load vector*. Eq.(5.6) represents a system of N-equations and $N+1$ unknowns and its solutions define the *equilibrium paths* as curves in $\mathbb{R}^{N+1}$ from a known initial configuration $\mathbf{u}_0$, corresponding to $\lambda = 0$. We also define the tangent stiffness matrix as

$$\delta\mathbf{u}^T\mathbf{K}[\mathbf{u}]\tilde{\mathbf{u}} = \Phi''[u]\tilde{u}\delta u \ \ , \ \ \forall\,\delta\mathbf{u}, \tilde{\mathbf{u}} \tag{3.3}$$

where δu and $\tilde{u}$ are generic variations of the configuration field u and $\delta\mathbf{u}$ and $\tilde{\mathbf{u}}$ the corresponding discrete vectors.

3.2 PATH-FOLLOWING STRATEGIES

Path-following methods aim at drawing the equilibrium path step-by step. Starting from a known equilibrium point, it is searched for a successive one by an iterative process. The simpler path-following technique is represented by the load-controlled method. It defines an increment to the loading multiplier and looks for the set of variables that satisfy the equilibrium within a certain tolerance. Its main issue is represented by the loss of convergence near a limit point, that represents a serious limitation. To overcome this drawback, the commonly accepted solution can be found in the work of Riks [4] who proposed the arc-length strategy. It represents a generalisation of Newton's method in which an additional condition is included to overcome the convergence issues. In the following subsection, details on the arc-length methods are given for the case of mixed solid-shell model.

3.2.1 Arc-length method

The Riks approach [4] is the preferred strategy for solving Eq. (5.6) by adding a constraint of the shape $g[\mathbf{u},\lambda]-\xi=0$, which defines a surface in $\mathbb{R}^{N+1}$. Assigning successive values to the control parameter $\xi=\xi_{(k)}$ the solution of the nonlinear system

$$\mathbf{R}[\xi]\equiv\begin{bmatrix}\mathbf{r}[\mathbf{u},\lambda]\\ g[\mathbf{u},\lambda]-\xi\end{bmatrix}=0 \tag{3.4}$$

defines a sequence of points (steps) $\boldsymbol{z}_{(k)}\equiv\{\mathbf{u}_{(k)},\lambda_{(k)}\}$ belonging to the equilibrium path. Starting from a known equilibrium point $\boldsymbol{z}^0\equiv\boldsymbol{z}_{(k)}$, the new one $\boldsymbol{z}_{(k+1)}$ is evaluated correcting a first extrapolation $\boldsymbol{z}^1=\{\mathbf{u}^1,\lambda^1\}$ by a sequence of estimates $\boldsymbol{z}^j$ (loops) by a Newton iteration

$$\begin{cases}\bar{\mathbf{J}}\dot{\boldsymbol{z}}=-\mathbf{R}^j\\ \boldsymbol{z}^{j+1}=\boldsymbol{z}^j+\dot{\boldsymbol{z}}\end{cases} \tag{3.5a}$$

where $\mathbf{R}^j\equiv\mathbf{R}[\boldsymbol{z}^j]$ and $\bar{\mathbf{J}}$ is the Jacobian of the nonlinear system (3.4) at $\boldsymbol{z}^j$ or a suitable estimate. The simplest choice for $g[\mathbf{u},\lambda]$ is the linear constraint corresponding to the orthogonal hyperplane

$$\mathbf{n}_u^T(\mathbf{u}-\mathbf{u}^j)+n_\lambda\,(\lambda-\lambda^j)=\Delta\xi \quad \text{where} \quad \begin{cases}\mathbf{n}_u\equiv\mathbf{M}\,(\mathbf{u}^j-\mathbf{u}_{(k)})\\ n_\lambda\equiv\mu\,(\lambda^j-\lambda_{(k)})\end{cases} \tag{3.5b}$$

$\mathbf{M}$ and μ being some suitable metric factors [49, 50], $\Delta\xi$ an assigned increment of ξ and

$$\bar{\mathbf{J}}\approx\left[\frac{\partial\mathbf{R}[\boldsymbol{z}]}{\partial\boldsymbol{z}}\right]_{\boldsymbol{z}^j}=\begin{bmatrix}\bar{\mathbf{K}} & -\mathbf{f}\\ \mathbf{n}_u^T & n_\lambda\end{bmatrix}. \tag{3.5c}$$

The load-controlled scheme is obtained assuming $g[\mathbf{u},\lambda]=\lambda$ (see [49] for further details) while keeping $\bar{\mathbf{K}}=\mathbf{K}[\mathbf{u}^1]$ we have the modified Newton scheme. The solution of Eq.(3.5) is conveniently performed as follows

$$\begin{cases}\dot{\lambda}=\dfrac{\mathbf{n}_u^T\bar{\mathbf{K}}\mathbf{r}^j}{n_\lambda+\mathbf{n}_u^T\bar{\mathbf{K}}\mathbf{f}}\\ \bar{\mathbf{K}}\dot{\mathbf{u}}=\dot{\lambda}\mathbf{f}-\mathbf{r}^j.\end{cases} \tag{3.6}$$

3.2.2 Convergence of the arc-length scheme.

The convergence of the iterative process (3.5) has been widely discussed by Garcea et al. [49] and can be expressed by the condition

$$\mathbf{R}_{j+1} = \left(\mathbf{I} - \mathbf{J}_s \tilde{\mathbf{J}}^{-1}\right) \mathbf{R}_j \tag{3.7}$$

where $\mathbf{I}$ is the identity matrix and

$$\mathbf{J}_s \equiv \int_0^1 \mathbf{J}[\mathbf{z}_j + t(\mathbf{z}_{j+1} - \mathbf{z}_j)]\, dt$$

the secant Jacobian matrix. The iteration converges if in some norm we have

$$\left\| \mathbf{I} - \mathbf{J}_s \tilde{\mathbf{J}}^{-1} \right\| < 1$$

and it will be as fast as $\tilde{\mathbf{J}}$ is close to $\mathbf{J}_s$. Also note that the convergence condition for a load controlled scheme is obtained by replacing $\tilde{\mathbf{J}}$ and $\mathbf{J}_s$ with $\tilde{\mathbf{K}}$ and $\mathbf{K}_s$ respectively. For the displacement format in the case of positive definite $\tilde{\mathbf{K}}$ the convergence condition can be simplified as

$$0 < \mathbf{u}^T \mathbf{K}_s \mathbf{u} < 2\mathbf{u}^T \tilde{\mathbf{K}} \mathbf{u}, \quad \forall \mathbf{u} \tag{3.8}$$

A convergence condition similar to Eq.(3.8) but limited to the subspace of nonsingular values of $\tilde{\mathbf{K}}$ holds also for the arc-lenght scheme [49] that, like for the load controlled case, is as faster as

$$\mathbf{u}^T \mathbf{K}_s \mathbf{u} \approx \mathbf{u}^T \tilde{\mathbf{K}} \mathbf{u}, \quad \forall \mathbf{u} \tag{3.9}$$

and it converges in a single iteration when $\mathbf{K}_s = \tilde{\mathbf{K}}$ because of the linearity of Eq.(3.5b).

The arc-length scheme provides a simple way to overcome limit points because $\tilde{\mathbf{J}}$ is not singular even when $\tilde{\mathbf{K}}$ is singular. The convergence is, however, strongly affected by the variables chosen to describe the problem since a smoother representation of the equilibrium path makes it easy to fulfil the condition (3.9) allowing large steps and few loops. In the following we will show that this desirable behaviour occurs in the case of a mixed description while the displacement-based one, for any discretised model, is affected by an extrapolation locking that could produce a pathological reduction in the step size (increase in iterations) and, in some cases, loss of convergence.

3.2.3 Advantages of the mixed format

The efficiency and the robustness of a nonlinear analysis is strongly dependent on the iterative effort, namely the capability of converging using a low number of iterations and to withstand large step sizes (increments). In many works [14, 49], it is shown that the path-following techniques exhibits slow convergence when any purely displacement-based formulation is adopted. This could be considered as a sort of *locking* of the iterative method, since its performance gets worse when the slenderness of the structures increases. This fact is unrelated to the accuracy of the interpolation and always occurs in displacement formulations where the stresses used to evaluate the tangent matrix are forced to satisfy the constitutive equations at each iteration.

Conversely, mixed (stress-displacement) formulations are not affected by this phenomenon, because the stresses are directly extrapolated and corrected in the iterative process, allowing a faster convergence of the Newton method and very large steps, independently of the slenderness of the structure. We refer readers to [14, 49] for further details on this phenomenon.

3.2.4 Remarks on the computational cost

The computational cost of the iterative method is directly proportional to the number of iterations for the full versions and almost directly proportional to the number of steps for the modified version. When the number of DOFs increases, the cost of an entire step of the modified version tends to the cost of a single iteration of the full method.

3.3 KOITER'S METHOD

Let us consider a slender hyperelastic structure subject to conservative nominal loads $\hat{p}$ proportionally increasing with the amplifier factor λ. The equilibrium is expressed by the virtual work in Eq. (3.1) Due to the assumed 3rd order polynomial dependence of $\Phi[u]$ on u, it can be exactly replaced with its 3rd order Taylor expansion from a given configuration $u = u_0$, that is

$$\Phi'[u]\delta u := \left(\Phi'_0 + \Phi''_0(u - u_0) + \frac{1}{2}\Phi'''(u - u_0)^2\right)\delta u, \quad \forall \delta u \in \mathcal{T}, \tag{3.10}$$

where a subscript denotes, from now on, the point in which the quantities are evaluated, i.e. $\Phi_0' \equiv \Phi'[u_0]$ and so on, while the quantity Φ''' is constant with u.

3.3.1 Fundamental path.

The method starts with the evaluation of the *fundamental path* $u_f[\lambda]$ assumed as analytical in λ and approximated with its tangent in the (known) equilibrium configuration $(u_0, \lambda_0 = 0)$ as $u_f = u_0 + \lambda\hat{u}$. It is evaluated through a first order Taylor expansion in λ of Eq.(3.1), that is

$$\Phi_0''\hat{u}\delta u - \hat{p}\delta u = 0, \quad \forall \delta u \in \mathcal{T}. \tag{3.11}$$

3.3.2 Buckling loads and modes.

With the adopted linear extrapolation in λ of the fundamental path, it is possible to evaluate the bifurcation condition, that is the singularity of the second strain energy variation, as

$$\Phi''[u_f[\lambda]]\dot{v}_i\delta u \equiv (\Phi_0'' + \lambda\Phi'''\hat{u})\dot{v}_i\delta u = 0 \; \forall \delta u \in \mathcal{T} \tag{3.12}$$

where $\dot{v}_i$ and λ_i are the bifurcation modes and loads. Note that the expression in Eq.(3.12) is exact, due to the zeroing of all the higher order energy terms, and so the buckling condition is exactly a linear eigenvalue problem [14], which provides the m bifurcation loads and modes, orthogonalised according to

$$\Phi'''\hat{u}\dot{v}_i\dot{v}_k = -\delta_{ik} \tag{3.13}$$

with δ_{ik} the Kronecker symbol.

3.3.3 The reduced model of the perfect structure.

According to a Lyapunov-Schmidt decomposition [51], $\mathcal{U}$ is decomposed as a direct sum of the critical subspace $\mathcal{V}$ and its orthogonal complement $\mathcal{W}$, defined as

$$\mathcal{U} = \mathcal{V} \oplus \mathcal{W}, \qquad \begin{cases} \mathcal{V} = \{v : \; v = \sum_{i=1}^{m} \xi_i \dot{v}_i\} \\ \mathcal{W} = \{w : \; \Phi'''\hat{u}\dot{v}_i w = 0\} \end{cases} \tag{3.14}$$

where ξ_i, with $i = 1 \cdots m$ are the buckling mode amplitudes.

The space of admissible configurations, following a Galerkin approach, is limited to

$$u_d = u_f[\lambda] + v[\xi_i] + w[\lambda, \xi_i] \tag{3.15}$$

where the corrective term $w \in \mathcal{W}$ is assumed to be at least quadratic in λ and ξ_i and the compact notation $f[\xi_i]$ is used to denote the dependence of function f on all the ξ_i.

Using a Ritz-Galerkin approach the equilibrium equation is imposed assuming $\dot{v}_i$ and δw as test functions, and the configuration defined by u_d, that is

$$\begin{aligned} r_w[\lambda, \xi_i] \equiv& \{\Phi'[u_d] - \lambda \hat{p}\}\delta w = 0 \\ r_k[\lambda, \xi_i] \equiv& \{\Phi'[u_d] - \lambda \hat{p}\}\dot{v}_k = 0. \end{aligned} \tag{3.16}$$

From the condition $r_w[\lambda, \xi_i] = 0$ and using a Taylor expansion up to the 2th order in $\lambda, \xi_1, \cdots \xi_m$ we obtain the quadratic correctives (see [17])

$$w = \frac{1}{2}\lambda^2 \hat{\hat{w}} + \frac{1}{2}\sum_{ij} \xi_i \xi_j w_{ij} \quad \begin{cases} \Phi_b'' \hat{\hat{w}} \delta w = -\Phi''' \hat{u}^2 \delta w \\ \Phi_b'' w_{ij} \delta w = -\Phi''' \dot{v}_i \dot{v}_j \delta w \end{cases} \quad \forall \delta w \in \mathcal{W} \tag{3.17}$$

where the subscript b denotes quantities evaluated in $\lambda_b \hat{u}$ and λ_b is a suitable reference value of the bifurcation load (the first bifurcation load or a mean value of the bifurcation cluster).

From the condition $r_k[\lambda, \xi_i] = 0$ we obtain the reduced nonlinear system which defines the equilibrium path

$$\begin{aligned} r_k[\lambda, \xi_i] \equiv \mu_k[\lambda] + (\lambda_k - \lambda)\xi_k - \frac{1}{2}\lambda^2 \sum_{i=1}^{m} \xi_i \mathcal{C}_{ik} + \frac{1}{2}\sum_{i,j=1}^{m} \xi_i \xi_j \mathcal{A}_{ijk} \\ + \frac{1}{6}\sum_{i,j,h=1}^{m} \xi_i \xi_j \xi_h \mathcal{B}_{ijhk} = 0, \quad k = 1 \cdots m \end{aligned} \tag{3.18}$$

where

$$\begin{aligned} \mathcal{A}_{ijk} =& \Phi''' \dot{v}_i \dot{v}_j \dot{v}_k \\ \mathcal{C}_{ik} =& \Phi_b'' \hat{\hat{w}} w_{ik} \\ \mathcal{B}_{ijhk} =& -\Phi_b''(w_{ij} w_{hk} + w_{ih} w_{jk} + w_{ik} w_{jh}) \\ \mu_k[\lambda] =& \frac{1}{2}\lambda^2 \Phi''' \hat{u}^2 \dot{v}_k. \end{aligned} \tag{3.19}$$

Eqs.(3.18) are an algebraic nonlinear system of m equations in the $m+1$ variables λ, $\xi_1 \cdots \xi_m$ that, due to the small size of the system, can be efficiently solved using specialised variants of the arc–length scheme. Second and third order variations of the strain energy are required for the evaluation of coefficients in Eq.(3.19).

3.3.4 Standard a-posteriori account of geometrical imperfections.

Small imperfections, expressed by an initial displacement $\tilde{u}$, can easily be considered in the asymptotic analysis. In the current proposal [5, 33, 43, 44] the following coefficients

$$\tilde{\mu}_k := \lambda \Phi''' \hat{u} \tilde{u} \dot{v}_k \tag{3.20}$$

are added to Eq.(3.18), that is

$$r_k + \tilde{\mu}_k = 0 \tag{3.21}$$

and the reduced model is corrected by adding $\tilde{u}$ to the expression (3.15)

$$u_d = \tilde{u} + u_f[\lambda] + v[\xi_i] + w[\lambda, \xi_i]. \tag{3.22}$$

So, once the steps in Eqs.(3.11), (3.12), (3.17), (3.19) of the analysis have been performed, once and for all, small imperfections in the geometry can be taken into account by adding a few additional terms in the expression of r_k. The computational extra-cost is negligible since just the reduced nonlinear equations Eq.(3.18) have to be solved again for each new imperfection. In this way the method allows a low cost imperfection sensitivity analysis. In particular the reader is referred to [52] where the imperfection sensitivity analysis is performed by means of a Monte Carlo simulation showing how thousands of geometrical imperfections can be analysed in a few minutes in order to detect the worst imperfection shape.

However, comparisons with standard path-following analyses show that the accuracy of this approach is limited to small imperfection amplitudes and structures with an almost linear pre-critical behaviour. In the following chapter, it will be proposed a solution to improve its accuracy, making the approach suitable for a wider range of practical problems.

3.3.5 Advantages of the mixed format

As already highlighted, the model derived from the three-dimensional continuum using the Green strain measure has a low order dependence on the strain energy from the discrete parameters. In detail, when a mixed format is adopted, the strain energy has got a cubic polynomial dependence from displacements and stresses, namely just one order more than in the linear elastic case. The consequences of this occurrence are essentially two. The first one concerns the fact that the buckling condition is exactly linear, and the accuracy is not influenced by the closeness of the buckling loads or from the magnitude of $(\lambda_i - \lambda_b)$. Consequently, the coherence of the method is enlarged with respect to the general case in which the buckling condition is linearised. The second aspects regards the zeroing of the fourth-order variations. In fact, the evaluation of the fourth-order variations represents the most challenging task for geometrically exact shell and beam models [46, 47] and for those based on corotational approaches [10, 29, 48], that explicitly make use of the rotation tensor and its highly nonlinear representation. In such cases, the strain energy is infinitely differentiable with respect to its parameters and leads to very complex expressions for the energy variations with a high computational burden of path following and much more of asymptotic analyses. In this last case the high order strain energy variations become so complex that often "ad hoc" assumptions are required to make the solution process effective (see section 4.3 of [48]).

However, the main advantage in using a mixed formulation is its capability to rectify an important but underhand locking effect, called *extrapolation locking* [15, 49]. The nature of the phenomenon is the same than that discussed in the previous section about the path-following technique. But, if the mistaken extrapolation during path-following iterations penalises the performance of the algorithm, in the case of Koiter's method the accuracy is influenced. In fact, in the case of displacement-based formulations and relatively slender structures, a completely wrong estimate of the equilibrium path is given, because Koiter's method directly uses the extrapolated quantities for the construction of the reduced system of equilibrium equations. The mixed formulation naturally prevents extrapolation locking, and its use is a mandatory requirement for formulating an accurate Koiter's method. We refer to the work by Garcea et al. for insights on the matter [14, 15, 49].

3.3.6 Koiter's FE algorithm

The asymptotic approach is based on a third order Taylor expansion of Eq.(3.1), in terms of load factor λ and modal amplitudes ξ_i. We refer readers to [17, 53] for recent developments of the method and more detail.

Letting $u_i \in \mathcal{T}$ be a generic variation of the displacement field and denoting with a bold symbol the discrete FEM counterpart of the continuum quantities, and referring to the solid-shell finite element model presented in [17], the construction of the reduced model of the *perfect structure* consists of the following steps.

1. The fundamental path is evaluated as

$$\mathbf{u}^f[\lambda] = \mathbf{u}_0 + \lambda\hat{\mathbf{u}} \ , \ \ \mathbf{K}_0\,\hat{\mathbf{u}} = \mathbf{f} \ , \ \ \mathbf{K}_0 \equiv \mathbf{K}[\mathbf{u}_0] \tag{3.23a}$$

where $\mathbf{K}_0$ and $\mathbf{f}$ are obtained from the following energy equivalence

$$\mathbf{u}_1^T\mathbf{K}_0\mathbf{u}_2 := \Phi_0''u_1u_2 \qquad \mathbf{u}_1^T\mathbf{f} = p\,u_1.$$

and requires the solution of a linear system to evaluate the initial path tangent $\hat{\mathbf{u}}$. A subscript will denote, from now on, the point in which the quantities are evaluated, i.e. $\Phi_0'' \equiv \Phi''[u_0]$ and so on.

2. The buckling modes and loads are obtained from the linearised critical condition consisting of the eigenvalue problem

$$\mathbf{K}[\lambda]\dot{\boldsymbol{v}} \equiv (\mathbf{K}_0 + \lambda\mathbf{K}_1[\hat{\mathbf{u}}])\dot{\boldsymbol{v}} = 0 \tag{3.23b}$$

where $\mathbf{K}_1$ is obtained from the following energy equivalence

$$\mathbf{u}_1^T\mathbf{K}_1\mathbf{u}_2 = \Phi_0'''\hat{u}u_1u_2.$$

3. The $(m \times (m+1))/2 + 1$ quadratic corrective FE vectors $\boldsymbol{w}_{ij}, \hat{\hat{\boldsymbol{w}}}$ are obtained by the solution of the linear systems

$$\begin{aligned} &\mathbf{K}_b\hat{\hat{\boldsymbol{w}}} + \hat{\hat{\mathbf{f}}} + \sum_{k=1}^{m} c_k\hat{\mathbf{f}}_k = 0 \qquad \text{with} \quad c_k = \dot{\boldsymbol{v}}_k^T\hat{\hat{\mathbf{f}}} \\ &\mathbf{K}_b\boldsymbol{w}_{ij} + \mathbf{f}_{ij} + \sum_{k=1}^{m} c_k\hat{\mathbf{f}}_k = 0 \quad \text{with} \quad c_k = \dot{\boldsymbol{v}}_k^T\mathbf{f}_{ij} \end{aligned} \tag{3.23c}$$

in which $\mathbf{K}_b \equiv \mathbf{K}_0 + \lambda_b\mathbf{K}_1$, $\hat{\mathbf{f}}_k = \mathbf{K}_1\dot{\boldsymbol{v}}_k$, λ_b is a reference value of the bifurcation cluster, usually the first buckling load and $\mathbf{f}_{ij}, \mathbf{f}_{00}$ are defined as a function of modes $\dot{\boldsymbol{v}}_i$ and $\hat{\mathbf{u}}$ by the energy equivalences

$$\begin{aligned} \delta\boldsymbol{w}^T\mathbf{f}_{ij} &= \Phi'''\dot{v}_j\dot{v}_j\delta w \\ \delta\boldsymbol{w}^T\hat{\hat{\mathbf{f}}} &= \Phi'''\hat{u}^2\delta w \end{aligned}$$

4. The construction of the reduced system of equations

$$r_k[\lambda,\xi_i] \equiv \mu_k[\lambda] + (\lambda_k - \lambda)\xi_k - \frac{1}{2}\lambda^2 \sum_{i=1}^{m} \xi_i \mathcal{C}_{ik} + \frac{1}{2}\sum_{i,j=1}^{m} \xi_i\xi_j \mathcal{A}_{ijk} + \frac{1}{6}\sum_{i,j,h=1}^{m} \xi_i\xi_j\xi_h \mathcal{B}_{ijhk} = 0, \quad k = 1\cdots m \tag{3.23d}$$

is carried out by evaluating the energy terms for $i, j, h, k = 1\cdots m$ as sum of element contributions

$$\begin{aligned} \mathcal{A}_{ijk} =& \Phi'''\dot{v}_i\dot{v}_j\dot{v}_k \\ \mathcal{C}_{ik} =& \Phi''_b\hat{w}w_{ik} \\ \mathcal{B}_{ijhk} =& -\Phi''_b(w_{ij}w_{hk} + w_{ih}w_{jk} + w_{ik}w_{jh}) \\ \mu_k[\lambda] =& \frac{1}{2}\lambda^2\Phi'''\hat{u}^2\dot{v}_k \end{aligned}$$

where

$$\Phi''_b u_1 u_2 = (\Phi''_0 + \lambda_b\Phi'''\hat{u})u_1u_2 \quad \forall u_1, u_2.$$

The evaluation of the equilibrium path, to be repeated for each additional imperfection, is obtained by solving the modified reduced system

$$r_k[\lambda,\xi_i] + \tilde{\mu}_k[\lambda,\xi_i] = 0,$$

where $\tilde{\mu}_k$ represents the effect of the imperfection.

4 ISOGEOMETRIC MODEL

In recent years, an increasing amount of research has aimed at developing new efficient solid-shell FEs [11, 54–57] for nonlinear analysis of thin structures. This is due to the advantages of these kinds of elements in comparison to classical shell ones, as discussed in chapter 2 and 3. Solid-shell elements are often based on a linear displacement interpolation in order to achieve computational efficiency and then exhibit shear locking, also present in traditional shell elements, and trapezoidal and thickness locking, typical of solid elements [58]. These kinds of locking are usually sanitised by means of Assumed Natural Strain (ANS), Enhanced Assumed Strain (EAS) [59, 60] and mixed (hybrid) formulations [11, 61, 62]. Solid-shells have been used to model composites or laminated beams [55, 61, 63] and shell structures in both the linear [56, 59, 64] and nonlinear [11, 54, 60] range. Among the most effective and interesting proposals are the mixed solid-shell elements of Sze and co-authors [11] which extend the initial PT18β hybrid element of Pian and Tong [65] to thin shells and eliminate thickness locking by means of a modified generalised constitutive matrix. This approach makes it possible, as opposed to EAS, to avoid the introduction of additional degrees of freedom (DOFs) and to obtain good predictions for multi-layered composites. Although there is the effective elimination of the interpolation locking, low order solid-shell elements exhibit a poor behaviour when analysing curved geometries. High order Lagrangian interpolations, on the other hand, have been little used due to the high number of DOFs and computational cost for the integration and assembly of the quantities [66].

The isogeometric analysis (IGA) [12, 67] represents a good alternative to high order Lagrangian FEs. The main reason for its success is, in our opinion, the way it makes it possible to elevate the order of the shape functions while practically maintaining the same number of DOFs of linear Lagrangian interpolations. Another notable feature is that the high order continuity of the shape functions allows the total number of integration points to be reduced significantly as shown in [68, 69] compensating for the computational cost of the assembly of the discrete operators. Finally, the geometry is reproduced exactly, regardless of the mesh adopted and a simple link between CAD and structural analysis is available.

These considerations make IGA very attractive, particularly in geometrically nonlinear analysis where a highly continuous solution is often expected [45, 53, 70]. However, there are some difficulties associated with IGA with respect to traditional finite elements. The use of very high order shape functions eliminates interpolation locking but, at the same time, increases the computational effort for the integration and the assembly of the discrete quantities and for the solution of the discrete problem because of the decrease in the stiffness matrix sparsity. For these reasons C^1 and C^2 NURBS interpolations are often preferred, even if they are not immune to locking phenomena. Due to the inter-element continuity of the interpolation, element-wise reduced integrations and strategies, like ANS [13], only alleviate, but do not eliminate locking, and so are not effective for very thin shells. For the same reason, mixed formulations with stress shape functions defined at element level are not able to prevent locking. Conversely, mixed formulations with continuous stress shape functions have been successfully proposed [71, 72]. However, in this way the total number of DOFs increases with respect to the initial displacement formulation and the static condensation of the stress variables, usually employed in FE analysis and performed at the element level, can be carried out only at patch level and as a result is not convenient because it produces a full condensed stiffness matrix. An interesting alternative is the use of displacement formulations with patch-wise reduced integration rules [68]. These have been shown to alleviate and, in some cases, eliminate interpolation locking in linear elastic problems [69] employing a low number of integration points and so significantly improve the computational efficiency. This strategy seems more attractive than the mixed formulation, since it preserves the stiffness matrix sparsity without introducing additional unknowns and allows a more efficient integration.

However, it has been discussed in chapter 3, how the mixed formulation has superior performance than displacement-based ones in path-following analyses and Koiter's method, due to the extrapolation locking [14, 49]. To preserve the advantage that IGA displacement-based formulations offer in terms of interpolation efficiency, the mixed formulation is formulated in the following way. Stresses are not interpolated, but are taken as independent variables at each integration point. The resulting discrete model maintains the same accuracy of displacement-based formulation, but the extrapolation locking is eliminated. This strategy has been recently adopted [16] under the name of Mixed Integration Point (MIP).

In this chapter, the isogeometric solid-shell interpolation is adopted to obtain an efficient discretised solid-shell model. The interpolation functions are NURBS of generic order, controlled by control points, each of them equipped with six

DOFs. Shear and membrane locking, which already occur in linear elastic problems for low order NURBS [73], are even heavier in the nonlinear range when large displacements occur. Different patch-wise reduced integration rules [68, 69], previously proposed for linear analyses, are investigated in large deformation problems with the aim of eliminating interpolation locking and increasing the computational efficiency in the proposed solid-shell model when C^1 and C^2 NURBS are adopted. The displacement-based solid-shell formulation so obtained seems able to provide accurate solutions, practically unaffected by locking, without the need of a mixed formulation and the corresponding, previously discussed, drawbacks. The MIP strategy is extended to the proposed IGA framework with the aim of reducing the iterative effort and making it independent of the slenderness of the structure.

4.1 NURBS BASIS

A B-Spline curve is represented as

$$\mathbf{c}[\xi] = \sum_{i=1}^{n} N_i^p[\xi]\mathbf{P}_i = \mathbf{N}[\xi]\mathbf{P} \tag{4.1}$$

where $\mathbf{P}_i$, $i = 1 \cdots n$ are control points and $N_i^p(\xi)$ are the set of B-Spline basis functions, which are piecewise polynomial functions of order p. The latter are defined by a set of non-decreasing real numbers $\Xi = [\xi_1, \xi_2, ..., \xi_{n+p+1}]$ known as knot vector. More details on the B-Spline parameterisation can be found in [74]. B-spline basis functions are calculated recursively by using the formula

$$N_i^p[\xi] = \frac{\xi - \xi_i}{\xi_{i+p} - \xi_i} N_i^{p-1}[\xi] + \frac{\xi_{i+p+1} - \xi}{\xi_{i+p+1} - \xi_{i+1}} N_{i+1}^{p-1}[\xi]$$

for $p \geqslant 1$ and starting from piecewise constant functions ($p = 0$) defined as

$$N_i^0[\xi] = \begin{cases} 1, & \text{if} \quad \xi_i \leqslant \xi \leqslant \xi_{i+1} \\ 0, & \text{otherwise.} \end{cases}$$

B-Spline basis functions have attractive properties: they satisfy the partition of unity that makes them suitable for discretisation methods, have a compact support and are non-zero and non-negative within the knot interval $[\xi_i, \xi_{i+p+1}]$. The regularity r between two parametric or physical elements is described by the multiplicity of the associated knot in Ξ. The regularity is given by $r = p - s$

where p and s are the order used for the basis functions and the multiplicity of the knot ξ_i respectively.

Since B-splines are polynomial functions they are not able to represent circular arcs and conic sections exactly. For this reason NURBS extend the B-spline concept in order to represent these objects exactly. NURBS are obtained by a projective transformation of B-splines extending Eq.(4.1) by using

$$R_i^p[\xi] = \frac{N_i^p[\xi] w_i}{\sum_i^n N_i^p[\xi] w_i} \tag{4.2}$$

as shape functions. It is worth noting that all properties of B-Splines are maintained and, in particular, B-Splines are retrieved when all the weights are equal.

By applying the tensor product, the NURBS surface is constructed in a similar way to Eq.(4.1) as

$$\mathbf{s}[\xi,\eta] = \sum_{i=1}^{n} \sum_{j=1}^{m} R_i^p[\xi] M_j^q[\eta] \mathbf{P}_{ij} = \mathbf{N}[\xi,\eta]\mathbf{P} \tag{4.3}$$

where $\Xi = [\xi_1, \xi_2 ... \xi_{n+p+1}]$ and $\mathcal{H} = [\eta_1, \eta_2 ... \eta_{m+q+1}]$ are two knot vectors, R_i^p and M_j^q are the one-dimensional basis functions over these knot vectors and $\mathbf{P}_{ij}$ defines a set of $n \times m$ control points. The tensor product of the knot vectors Ξ and $\mathcal{H}$ defines a mesh of quadrilateral ”isogeometric elements”.

Weights, as well as control points of the initial geometry, are provided by the CAD model while suitable algorithms exist for the refinement required to approximate the unknown solution [12, 74]. The geometry is always represented exactly regardless the mesh adopted.

4.2 THE ISOGEOMETRIC SOLID-SHELL ELEMENT

The kinematics of the solid-shell model derived in chapter 2 allows a 2D description of the shell. Following the isogeometric concept, geometry and displacement field are interpolated, over the element, as follows

$$\begin{aligned} \mathbf{X}[\zeta] &= \mathbf{N}_d[\zeta]\mathbf{X}_e \\ \mathbf{d}[\zeta] &= \mathbf{N}_d[\zeta]\mathbf{d}_e \end{aligned} \tag{4.4}$$

where $\mathbf{d}_e = [\mathbf{d}_{0e}, \mathbf{d}_{ne}]$ and $\mathbf{X}_e = [\mathbf{X}_{0e}, \mathbf{X}_{ne}]$ collect the element control points for displacement and geometry. The matrix $\mathbf{N}_d[\zeta]$ collects the interpolation functions

$$\mathbf{N}_d[\zeta] \equiv \left[\mathbf{N}[\xi,\eta], \zeta\mathbf{N}[\xi,\eta]\right] \tag{4.5}$$

where $\zeta \in [-1,+1]$ and $\mathbf{N}[\xi,\eta]$ are bivariate NURBS (4.3), functions of the middle surface coordinates only. The integrals in Eq. (2.28) to compute the elemental strain energy is evaluated numerically. Following the MIP strategy, stresses are not interpolated, but taken as independent variable at each integration point. Consequently, the elemental energy is

$$\Phi_e[\mathbf{u}_e] = \sum_{g=1}^{n} \left(\boldsymbol{\sigma}_g^T \boldsymbol{\varepsilon}_g[\mathbf{d}_e] - \frac{1}{2} \boldsymbol{\sigma}_g^T \mathbf{C}_g^{-1} \boldsymbol{\sigma}_g \right) w_g, \tag{4.6}$$

where the quantities evaluated at the integration point are denoted with the subscript g and w_g is the weight. The integration rule in the case of IGA is discussed in the section 4.2.4. The elemental variables, collected in the vector $\mathbf{u}_e$ are displacements of the control points related to the element and the stresses at integration points, namely

$$\mathbf{u}_e = \begin{bmatrix} \boldsymbol{\sigma}_1 \\ \vdots \\ \boldsymbol{\sigma}_n \\ \mathbf{d}_e . \end{bmatrix} \tag{4.7}$$

4.2.1 Strain energy variations

In the following $\mathbf{u}_{ig} = \{\boldsymbol{\sigma}_{ig}, \mathbf{d}_{ie}\}$ will denote the vector representation on the integration point g of u_i.

The first variation of (4.6) is

$$\Phi_e' u_1 = \sum_{g=1}^{n} \begin{bmatrix} \boldsymbol{\sigma}_{1g} \\ \mathbf{d}_{1e} \end{bmatrix}^T \begin{bmatrix} \mathbf{s}_{g\sigma} \\ \mathbf{s}_{gd} \end{bmatrix} w_g \tag{4.8a}$$

with

$$\begin{cases} \mathbf{s}_{g\sigma} \equiv \boldsymbol{\varepsilon}_g[\mathbf{d}_e] - \mathbf{C}_g^{-1} \boldsymbol{\sigma}_g \\ \mathbf{s}_{gd} \equiv \mathbf{B}_g[\mathbf{d}_e]^T \boldsymbol{\sigma}_g . \end{cases} \tag{4.8b}$$

and $\mathbf{B}_g[\mathbf{d}_e] = \mathbf{L}_g + \mathbf{Q}_g[\mathbf{d}_e]$. The second variation of (4.6) is

$$\begin{aligned}\Phi''_e u_1 u_2 = \sum_{g=1}^{n} (&\boldsymbol{\sigma}_{1g}^T \mathbf{B}_g[\mathbf{d}_e]\mathbf{d}_{2e} + \boldsymbol{\sigma}_{2g}^T \mathbf{B}_g[\mathbf{d}_e]\mathbf{d}_{1e} + \\ &\boldsymbol{\sigma}_g^T \mathbf{Q}_g[\mathbf{d}_{1e}]\mathbf{d}_{2e}) w_g.\end{aligned} \tag{4.8c}$$

Letting

$$\varepsilon_{gk}^{Q} = \mathbf{d}_{1e}^T \boldsymbol{\Psi}_{gk} \mathbf{d}_{2e}.$$

the kth component of vector $\mathbf{Q}_g[\mathbf{d}_{1e}]\mathbf{d}_{2e}$ the following expression holds

$$\boldsymbol{\sigma}_g^T \mathbf{Q}_g[\mathbf{d}_{1e}]\mathbf{d}_{2e} \equiv \sum_k \sigma_{gk}\, \varepsilon_{gk}^{Q} = \mathbf{d}_{1e}^T \mathcal{G}[\boldsymbol{\sigma}_g]\mathbf{d}_{2e}$$

with

$$\mathcal{G}[\boldsymbol{\sigma}_g] = \sum_k \sigma_{gk} \boldsymbol{\Psi}_{gk}. \tag{4.8d}$$

In matrix form the second variation of (4.6) then becomes

$$\begin{aligned}\Phi''_e u_1 u_2 &= \sum_{g=1}^{n} \begin{bmatrix} \boldsymbol{\sigma}_{1g} \\ \mathbf{d}_{1e} \end{bmatrix}^T \begin{bmatrix} -\mathbf{C}_g^{-1} & \mathbf{B}_g \\ \mathbf{B}_g^T & \mathcal{G}_g \end{bmatrix} \begin{bmatrix} \boldsymbol{\sigma}_{2g} \\ \mathbf{d}_{2e} \end{bmatrix} w_g \\ &= \sum_{g=1}^{n} \mathbf{u}_{1g}^T \mathbf{K}_g \mathbf{u}_{2g}\end{aligned} \tag{4.8e}$$

where $\mathcal{G}_g \equiv \mathcal{G}_e[\boldsymbol{\sigma}_g]$. The second variation can also be written in vector form introducing the incremental force vector so defined

$$\Phi''_e u_1 u_2 = \sum_{g=1}^{n} \mathbf{u}_{1g}^T \mathbf{s}'_g[\mathbf{u}_{2g}] \tag{4.8f}$$

with

$$\mathbf{s}'_g[\mathbf{u}_{2g}] \equiv \begin{bmatrix} -\mathbf{C}_g^{-1}\boldsymbol{\sigma}_{2g} + \mathbf{B}_g \mathbf{d}_{2e} \\ \mathbf{B}_g^T \boldsymbol{\sigma}_{2g} + \mathcal{G}_g \mathbf{d}_{2e} \end{bmatrix}$$

The third variation of the strain energy is

$$\begin{aligned}\Phi''_e u_1 u_2 u_3 = \sum_{g=1}^{n} (&\boldsymbol{\sigma}_{1g}^T \mathbf{Q}_g[\mathbf{d}_{3e}]\mathbf{d}_{2e} + \boldsymbol{\sigma}_{2g}^T \mathbf{Q}_g[\mathbf{d}_{3e}]\mathbf{d}_{1e} + \\ &\boldsymbol{\sigma}_{3g}^T \mathbf{Q}_g[\mathbf{d}_{1e}]\mathbf{d}_{2e}) w_g\end{aligned} \tag{4.8g}$$

that can also be written in vector form introducing the secondary force vector as

$$\Phi_e'''\delta u_1\delta u_2\delta u_3 = \sum_g \mathbf{u}_{1g}^T \mathbf{s}_g''[\mathbf{u}_{2g},\mathbf{u}_{3g}] \tag{4.8h}$$

with

$$\mathbf{s}_g''[\mathbf{u}_{2g},\mathbf{u}_{3g}] \equiv \begin{bmatrix} \mathbf{Q}_g[\mathbf{d}_{3e}]\mathbf{d}_{2e} \\ \mathbf{Q}_g[\mathbf{d}_{3e}]^T\boldsymbol{\sigma}_{2g} + \mathcal{G}_g[\boldsymbol{\sigma}_{3g}]\mathbf{d}_{2e} \end{bmatrix}$$

Finally, for each element vector $\boldsymbol{y}_e$ and matrix $\mathbf{Y}_e$ the global quantities are obtained using standard assemblage operations as

$$\boldsymbol{y} = \sum_e \mathcal{A}_e^T \boldsymbol{y}_e, \quad \mathbf{Y} = \sum_e \mathcal{A}_e^T \mathbf{Y}_e \mathcal{A}_e. \tag{4.9}$$

while scalar quantities are simply sums of element contributions.

4.2.2 Solutions in condensed form

The iterations of arc-length strategy and the steps of Koiter's algorithm can be written in condensed form, namely by static condensation of stress variables. In such a way the use of a mixed formulation does not imply an increase in global variables, but the computational cost of a displacement-based formulation is preserved.

In the following subsections the operations required by the solution strategies in chapter 3 are specified for the IGA MIP formulation.

4.2.3 Arc-length iteration

The linear system in Eq.(3.6), to be solved at each Newton iteration, can then be rewritten at the element level as

$$\begin{bmatrix} -\mathbf{C}_1^{-1}w_1 & & & \mathbf{B}_1 w_1 \\ & \ddots & & \vdots \\ & & -\mathbf{C}_n^{-1}w_n & \mathbf{B}_n w_n \\ \mathbf{B}_1^T w_1 & \dots & \mathbf{B}_n^T w_n & \sum_g^n \mathcal{G}_g w_g \end{bmatrix}^j \begin{bmatrix} \dot{\boldsymbol{\sigma}}_1 \\ \vdots \\ \dot{\boldsymbol{\sigma}}_n \\ \dot{\mathbf{d}}_e \end{bmatrix} = (\lambda^j + \dot{\lambda}) \begin{bmatrix} 0 \\ \vdots \\ 0 \\ \mathbf{f}_e \end{bmatrix} - \begin{bmatrix} \mathbf{s}_{1\sigma} w_1 \\ \vdots \\ \mathbf{s}_{n\sigma} w_n \\ \sum_g^n \left(\mathbf{B}_g^T \boldsymbol{\sigma}_g w_g\right) \end{bmatrix}^j \tag{4.10}$$

where the superscript on matrices denotes that they are evaluated during the iterative process at the current estimate $\mathbf{u}_e^j$.

By performing a static condensation of the stress correction $\dot{\boldsymbol{\sigma}}_g$, locally defined at the level of the integration point, we obtain

$$\dot{\boldsymbol{\sigma}}_g = \mathbf{C}_g \mathbf{B}^j_g \dot{\mathbf{d}}_e + \mathbf{C}_g \mathbf{s}^j_{g\sigma} = \mathbf{C}_g \mathbf{B}^j_g \dot{\mathbf{d}}_e + \mathbf{C}_g \boldsymbol{\varepsilon}^j_g - \boldsymbol{\sigma}^j_g \tag{4.11}$$

and, letting $\mathbf{r}_{ce}[\mathbf{d}^j_e] = \mathbf{s}_{ce}[\mathbf{d}^j_e] - \lambda^j \mathbf{p}_e$, the linear system in the condensed form becomes

$$\mathbf{K}_e[\mathbf{u}^j_e]\dot{\mathbf{d}}_e = -\mathbf{r}_{ce}[\mathbf{d}^j_e] + \dot{\lambda}\mathbf{f}_e \tag{4.12}$$

with

$$\mathbf{K}_e[\boldsymbol{\sigma}^j_g, \mathbf{d}^j_e] = \sum_{g=1}^{n} \left(\mathbf{B}_g[\mathbf{d}^j_e]^T \mathbf{C}_g \mathbf{B}_g[\mathbf{d}^j_e] + \mathcal{G}_g[\boldsymbol{\sigma}^j_g] \right) w_g \tag{4.13}$$

the condensed tangent stiffness matrix, that has the same expression as the classical displacement based one. However, this time it also depends on the independent stresses at the integration points, which are now directly extrapolated and corrected during the iterations.

4.2.3.1 *Fundamental path*

Eq.(3.23a) at the element level becomes

$$\begin{bmatrix} -\mathbf{C}_1^{-1} w_1 & & & \mathbf{L}_1 w_1 \\ & \ddots & & \vdots \\ & & -\mathbf{C}_n^{-1} w_n & \mathbf{L}_n w_n \\ \mathbf{L}_1^T w_1 & \dots & \mathbf{L}_n^T w_n & \mathbf{0} \end{bmatrix} \begin{bmatrix} \hat{\boldsymbol{\sigma}}_1 \\ \vdots \\ \hat{\boldsymbol{\sigma}}_n \\ \hat{\mathbf{d}}_e \end{bmatrix} = \begin{bmatrix} \mathbf{0} \\ \vdots \\ \mathbf{0} \\ \mathbf{f}_e \end{bmatrix} \tag{4.14}$$

By performing a static condensation of the stress correction $\dot{\boldsymbol{\sigma}}_g$, locally defined at the integration point, we obtain

$$\hat{\boldsymbol{\sigma}}_g = \mathbf{C}_g \mathbf{L}_g \hat{\mathbf{d}}_e \tag{4.15}$$

and then

$$\mathbf{K}^c_{0e} \hat{\mathbf{d}}_e = \mathbf{f}_e \quad \text{with} \quad \mathbf{K}^c_{0e} = \sum_{g=1}^{n} \left(\mathbf{L}_g^T \mathbf{C}_g \mathbf{L}_g \right) w_g \tag{4.16}$$

where the condensed element tangent stiffness matrix $\mathbf{K}^c_{0e}$ coincides with the classical displacement-based one

4.2.3.2 *Buckling problem*

The buckling problem can be written as

$$\begin{bmatrix} -\mathbf{C}_1^{-1} w_1 & & & (\mathbf{L}_1 + \lambda \mathbf{Q}_1[\hat{\mathbf{d}}_e]) w_1 \\ & \ddots & & \vdots \\ & & -\mathbf{C}_n^{-1} w_n & (\mathbf{L}_n + \lambda \mathbf{Q}_n[\hat{\mathbf{d}}_e]) w_n \\ (\mathbf{L}_1 + \lambda \mathbf{Q}_1[\hat{\mathbf{d}}_e])^T w_1 & \dots & (\mathbf{L}_n + \lambda \mathbf{Q}_n[\hat{\mathbf{d}}_e])^T w_n & \lambda \sum_g \mathcal{G}_g[\hat{\boldsymbol{\sigma}}_g] w_g \end{bmatrix} \begin{bmatrix} \dot{\boldsymbol{\sigma}}_1 \\ \vdots \\ \dot{\boldsymbol{\sigma}}_n \\ \dot{\mathbf{d}}_e \end{bmatrix} = \begin{bmatrix} 0 \\ \vdots \\ 0 \\ 0 \end{bmatrix} \tag{4.17}$$

and also in this case, eliminating the stresses of the integration points

$$\dot{\boldsymbol{\sigma}}_g = \mathbf{C}_g(\mathbf{L}_g + \lambda \mathbf{Q}_g[\hat{\mathbf{d}}_e]) \dot{\mathbf{d}}_e$$

and substituting in Eq.(4.17)

$$\left\{ \sum_g \left((\mathbf{L}_g + \lambda \mathbf{Q}_g)^T \mathbf{C}_g (\mathbf{L}_g + \lambda \mathbf{Q}_g) + \lambda \mathcal{G}_g[\hat{\boldsymbol{\sigma}}_g] \right) w_g \right\} \dot{\mathbf{d}}_e = 0,$$

we obtain the element contribution to the quadratic eigenvalue problem

$$\sum_g (\mathbf{K}_{0g}^c + \lambda \mathbf{K}_{1g}^c + \lambda^2 \mathbf{K}_{2g}^c) \dot{\mathbf{d}}_e = 0.$$

A linearized problem can also be obtained when the quadratic part of the strain along the fundamental path $\mathbf{Q}_g[\hat{\mathbf{d}}_e]$ is negligible and then

$$\left\{ \sum_g \left(\mathbf{L}_g^T \mathbf{C}_g \mathbf{L}_g + \lambda \mathcal{G}_g[\hat{\boldsymbol{\sigma}}_g] \right) w_g \right\} \dot{\mathbf{d}}_e = 0.$$

4.2.3.3 *Quadratic correctives*

Finally the linear system in Eq.(3.23c), letting $c_k = 0$ to simplify the writing, becomes

$$\begin{bmatrix} -\mathbf{C}_1^{-1} w_1 & & & \mathbf{B}_1 w_1 \\ & \ddots & & \vdots \\ & & -\mathbf{C}_n^{-1} w_n & \mathbf{B}_n w_n \\ \mathbf{B}_1^T w_1 & \dots & \mathbf{B}_n^T w_n & \sum_g \mathcal{G}_g w_g \end{bmatrix}_b \begin{bmatrix} \hat{\hat{\boldsymbol{\sigma}}}_1 \\ \vdots \\ \hat{\hat{\boldsymbol{\sigma}}}_n \\ \hat{\hat{\mathbf{d}}}_e \end{bmatrix} = - \begin{bmatrix} \mathbf{Q}_1[\hat{\mathbf{d}}_e]\hat{\mathbf{d}}_e \\ \vdots \\ \mathbf{Q}_n[\hat{\mathbf{d}}_e]\hat{\mathbf{d}}_e \\ \sum_g \left(\mathbf{Q}_g[\hat{\mathbf{d}}_e]^T \hat{\boldsymbol{\sigma}}_g + \mathcal{G}_g[\hat{\boldsymbol{\sigma}}_g]\hat{\mathbf{d}}_e \right) \end{bmatrix} \tag{4.18}$$

where subscript b on matrices denotes that they are evaluated in $\mathbf{u}_{bg} = \lambda_b\{\hat{\boldsymbol{\sigma}}_g, \hat{\mathbf{d}}_e\}$.

By condensing out the stress correction at the integration points

$$\hat{\hat{\boldsymbol{\sigma}}}_g = \mathbf{C}_g \mathbf{B}_g \hat{\hat{\mathbf{d}}}_e + \mathbf{C}_g \mathbf{Q}_g[\hat{\mathbf{d}}_e]\hat{\mathbf{d}}_e \tag{4.19}$$

we obtain the linear system in the condensed form

$$\mathbf{K}_{be}\hat{\hat{\mathbf{d}}}_e = -\hat{\hat{\mathbf{s}}}_c \tag{4.20}$$

with

$$\begin{aligned} \mathbf{K}_e[\hat{\mathbf{u}}_e] &= \sum_g \left(\mathbf{B}_g^T \mathbf{C}_g \mathbf{B}_g + \mathcal{G}_g[\boldsymbol{\sigma}_g]\right)_b w_g \\ \mathbf{s}_{ce}[\hat{\mathbf{u}}_e] &= \sum_g \left(\mathbf{Q}_g[\hat{\mathbf{d}}_e]^T \hat{\boldsymbol{\sigma}}_g + \mathcal{G}_g[\hat{\boldsymbol{\sigma}}_g]\hat{\mathbf{d}}_e + \mathbf{B}_g^T \mathbf{C}_g \mathbf{Q}_g[\hat{\mathbf{d}}_e]\hat{\mathbf{d}}_e\right) w_g \end{aligned} \tag{4.21}$$

as the condensed tangent stiffness matrix, that has the same expression as the classical displacement based one but directly depends on the stresses, and the condensed secondary forces respectively.

4.2.4 Locking and patch-wise reduced integrations

Note that the same NURBS interpolation is employed over the middle surface of the shell for all the displacement components. As is well known, this produces interpolation locking when low order interpolations are considered. The linear term in Eq.(2.26) can be plagued by standard shear and membrane locking, which then occurs even in small deformation problems. Furthermore, when a Total Lagrangian formulation is used to describe the nonlinear behaviour a more evident additional locking occurs as consequence of the different approximation of the linear and the quadratic Green-Lagrange strain contributions in Eq.(2.26).

Recently, patch-wise integration rules, which take into account the inter-element high continuity of the displacement interpolation have been proposed [68, 69] and applied to linear elastic problems. In our opinion, these works represent an important development in IGA. The d-dimensional target space, that is the space for the integration of the strain energy (as well as the stiffness matrix), of order p and regularity r, labelled as $\mathcal{S}_r^p$, is exactly integrated by a number of $\approx ((p-r)/2)^d$ integration points per element, distributed over the patch, significantly lower than in standard Gauss quadrature rules. For the full integration, due to the product of the shape functions and their derivatives,

p is twice the order of the splines and r is the continuity order minus one. This means that, for example, for C_1-quadratic and C_2-cubic splines the full integration spaces are $\mathcal{S}_0^4$ and $\mathcal{S}_1^6$ respectively.

Positions and weights of the integration points are not equal for each element, but are evaluated, once and for all, in a pre-processing phase and depend on r, p and patch mesh. The algorithms which provide these kinds of integration rules can be found in [68, 69] and are very efficient. Their computational burden is just a small fraction of the total cost of a linear analysis and negligible compared to a nonlinear analysis. We refer to [68, 69] for all the details.

The patch-wise exact integration of a given space $\mathcal{S}_r^p$ also opens up new possibilities for patch-wise reduced integration schemes. In fact p and r can be selected by the user and are not required to be those for the exact integration of the problem space. If the integration space presents spurious modes, more points than the minimum number strictly required by the space are utilised in order to remove them. In this case the approximation space is said to be over-integrated and labelled as $\bar{\mathcal{S}}_r^p$. The number of additional integration points is proportional to the number of boundary elements and, then, becomes negligible when the mesh gets finer. Again, we refer to [68, 69] for the details. With respect to the element-wise reduced integrations, an appropriate selection of the patch-wise reduced integration rules makes it possible to avoid spurious modes, alleviate or eliminate interpolation locking in the linear elastic range and further reduce the number of integration points.

It is worth noting that in patch-wise rules the number of integration points n can be different element-by-element, cf Eq.(4.6).

The use of a displacement-based IGA model is then theoretically accurate and efficient and represents, potentially, a reliable choice from the point of view of the discrete approximation and the efficiency of the integration with respect to standard FE interpolation of the same order if interpolation locking is avoided.

4.3 INTERPOLATION LOCKING TESTS

In the linear elastic range, low order NURBS interpolations usually exhibit shear and membrane locking. In the nonlinear range, when a Total Lagrangian formulation is adopted, other similar locking phenomena occur due to the different approximation of the linear and quadratic part of the Green-Lagrange strain components. This means that locking occurs in nonlinear analyses, even if the initial geometry is flat. In both linear and nonlinear cases, locking is related to the slenderness of the shell.

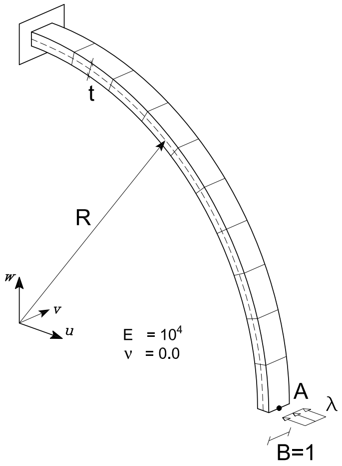

Figure 4.1: Curved bar: geometry and loads.

A series of patch-wise exact and reduced integration schemes for C^1 and C^2 NURBS basis are employed and compared. For the C^1 interpolation the comparison also includes element-wise reduced integration and the Assumed Natural Strain technique (ANS) [75], proposed for IGA in [13, 73].

4.3.1 Linear analysis

The first test is a classical benchmark to address membrane locking in the linear elastic range. It regards the clamped curved beam in Fig.4.1, which is considered a severe test to assess discrete formulations [13]. The normalised displacement at point A is reported in Fig.4.2 for an increasing slenderness and for the different interpolations and integration schemes. The reference value $u_{A,ref}$, from Bernoulli beam theory, is 0.942. A mesh of 10×1 elements is employed.

Concerning the C^1 interpolation, the full S_0^4 integration presents a very strong locking and provides bad results also for $R/t = 100$ and completely wrong results for $R/t = 1000$. The ANS technique gives good results for $R/t = 100$ slightly alleviating locking but it is not satisfactory for $R/t = 1000$. Furthermore the 2×2 Gauss element-wise reduced integration shows the identical results as ANS, which employs a grid of 3×3 Gauss points per element. The $\bar{S}_0^2$ reduced integration has the best performance and is almost insensitive to locking, a part from the extremely slender case $R/t = 10000$. From the computational point of

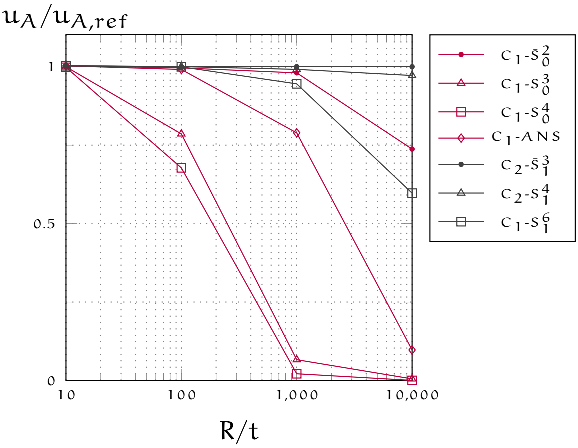

Figure 4.2: Curved bar: linear displacement for different slenderness ratio.

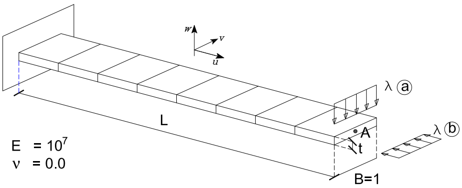

Figure 4.3: Cantilever beam under two load cases: geometry and loads.

view, it is worth noting that $\bar{S}^2_0$ uses about one integration point per element and is then more efficient than ANS and 2×2 reduced integration.

For the C^2 interpolation, the full integration S^6_1 is clearly affected by locking. On the contrary, both the integration schemes $\bar{S}^3_1$ and S^4_1 provide excellent results and are practically insensitive to locking. It is worth noting that $\bar{S}^3_1$ requires about one integration point per element, while S^4_1 about 2.25 integration points per element, so that both strategies are very efficient compared with Gauss rules.

4.3.2 Nonlinear analysis

In order to show the performances of the different strategies in dealing with locking, the simple cantilever beam depicted in Fig.4.3 is analyses with the proposed solid-shell model, for different values of the slenderness parameters $k = L/t$ and under two different load conditions.

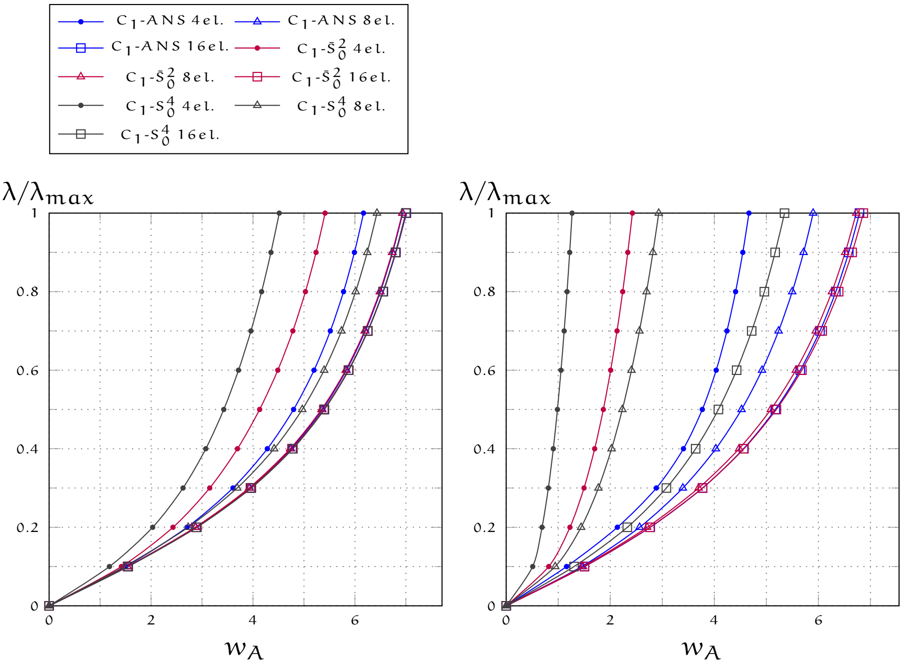

Figure 4.4: Cantilever beam under shear force: equilibrium path for C^1 and $L/h = 100$ (left) and $L/h = 1000$ (right).

For the shear load case, Fig.4.4 shows the equilibrium paths, up to the maximum value of the load $\lambda_{max} = 4 \cdot 10^7/k^3$, obtained with the C^1 interpolation for two different values of $k = 100$ and $k = 1000$ and different meshes. The full S_0^4 integration scheme provides bad results also for the smallest value of k, unless a large number of elements is used, and completely wrong results for $k = 1000$. The ANS technique gives good results for $k = 100$ slightly alleviating locking but it is not satisfactory for $k = 1000$. Furthermore, the 2×2 Gauss element-wise reduced integration shows the identical results as ANS (3×3 Gauss points per element) also in nonlinear context. The $\bar{S}_0^2$ reduced integration seems the best choice being almost insensitive to locking effects, except for the coarsest mesh, which is penalised by the over-integration required to avoid singularities. The general recommendation is to use it with at least 5 elements. $\bar{S}_0^2$ is also far more efficient than ANS and 2×2 reduced integration.

For the C^2 interpolation, the equilibrium paths of the cantilever beam under shear load discretised with 4 and 8 elements are reported in Fig.4.5. Also in

Table 4.1: Cantilever-beam: normalised end displacement at $\lambda/\lambda_{max} = 1$ for different interpolations and slenderness.

		4 elm.				8 elm.				16 elm.			
	L/h	$\bar{S}_0^2$	S_0^3	S_0^4	ANS	$\bar{S}_0^2$	S_0^3	S_0^4	ANS	$\bar{S}_0^2$	S_0^3	S_0^4	ANS
C^1	10^2	0,767	0,784	0,610	0,873	0,981	0,953	0,896	0,982	0,992	0,989	0,983	0,993
	10^3	0,343	0,315	0,164	0,661	0,952	0,511	0,385	0,835	0,972	0,828	0,722	0,961
	L/h	$\bar{S}_1^3$	S_1^4	S_1^5	S_1^6	$\bar{S}_1^3$	S_1^4	S_1^5	S_1^6	$\bar{S}_1^3$	S_1^4	S_1^5	S_1^6
C^2	10^2	0,977	0,992	0,988	0,961	0,999	1,000	1,000	0,998	1,000	1,000	1,000	1,000
	10^3	0,941	0,988	0,916	0,797	0,998	0,990	0,991	0,946	1,000	1,000	1,000	0,997

this case, the full integration S_1^6 exhibits locking. On the contrary, both the integration schemes $\bar{S}_1^3$ and S_1^4 provide very good results. S_1^4 is practically insensitive to locking effects for every mesh, while $\bar{S}_1^3$ is slightly penalised for the coarsest mesh due to the over integration required to avoid singularities.

In Table 4.1 the results previously described are summarised reporting the value of the end beam displacement w_A corresponding to a unitary load normalised with respect to the reference values w_A^{ref} obtained with C^2 interpolation, 32 elements and a S_1^4 integration. The table makes the comparison of the different strategies easy and highlights the great accuracy and insensitivity to locking of the C^2 interpolation when integrated with $\bar{S}_1^3$ and S_1^4 schemes and the enormous qualitative leap when passing from C^1 to C^2. Since the number of DOFs of the C^1 and the C^2 interpolation as well as the number of integration points, using the same mesh, is almost the same, the cost of the C^2 interpolation is just slightly higher than the C^1 one.

The second test regards the same cantilever beam under compression, i.e. a standard Euler cantilever beam. A very small shear imperfection load is added to avoid the jump of the bifurcation. The equilibrium path for different discretisations, integration schemes and slenderness ratios are reported in Fig.4.6 for the C^1 interpolation and in Fig.4.7 for the C^2 one. The load factor is normalised with respect to analytical buckling load λ_b. Similar comments to the previous test hold. In particular, the reduced integration schemes $\bar{S}_0^2$ for C^1 and $\bar{S}_3^1$ and S_1^4 for C^2 provide good predictions. However, as in the previous load case only the C^2 interpolation with S_1^4 integration is practically insensitive to k even for a very coarse mesh, where, conversely, the over-integrated schemes are penalised. Finally, the C^2 interpolation outperforms the C^1 one again in terms of accuracy, using the same mesh, and then employing a similar number of DOFs and integration points.

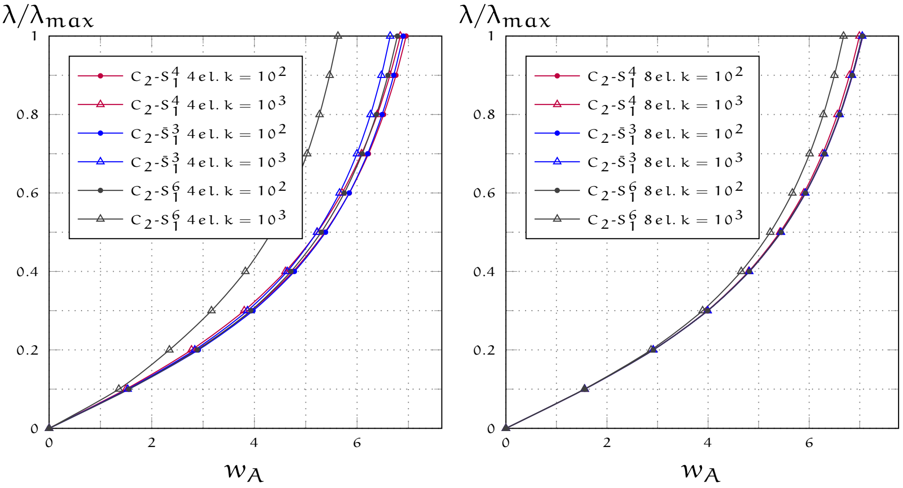

Figure 4.5: Cantilever beam under shear force: equilibrium path for C^2 and 4 e 8 elements.

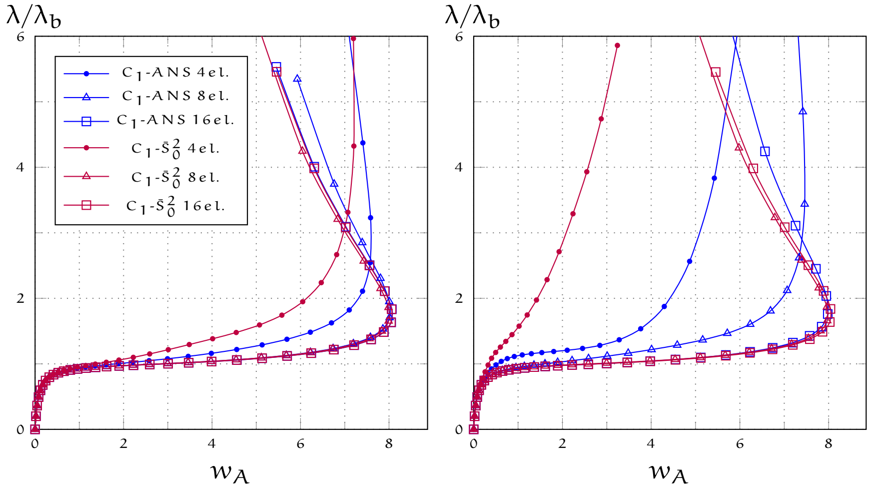

Figure 4.6: Euler beam under compression force: equilibrium path for C^1 and $L/h = 100$ (left) and $L/h = 1000$ (right).

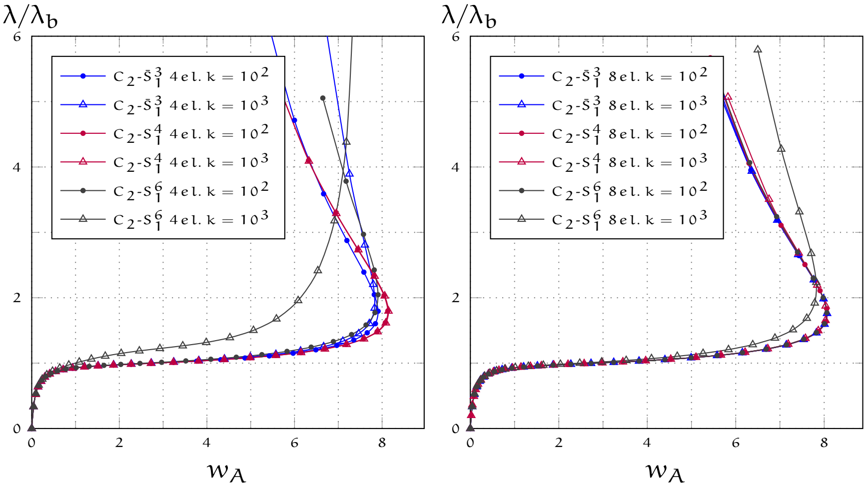

Figure 4.7: Euler beam under shear force: equilibrium path for C^2 and 4 e 8 elements.

Generally the C^2 interpolation seems preferable to the C^1 due to the possibility of also using coarse meshes, especially when integrated with the S_1^4 scheme, which is insensitive to locking, also for very slender structures and, in our opinion, is a more robust choice with respect to the $\bar{S}_1^3$ scheme. For these reasons, we recommend it among the strategies investigated. Other numerical tests will be presented in the next section to further validate this proposal.

4.4 SHELL OBSTACLE COURSES

In this section, the accuracy of the proposed isogeomentric solid-shell model with C^2 interpolation and S_1^4 patch-wise integration, labelled as C^2-S_1^4, is tested as well as the performances of the MIP strategy. Geometrically nonlinear problems are considered for shell structures in both isotropic and composite multi-layered materials. Some comparisons with FE results are reported. In particular we adopt the well-established hybrid stress linear FE of Sze [11] in the implementation proposed in [17], based on the Green-Lagrange strains, in order to avoid differences due to the strain measure. It is labeled as C^0-HS.

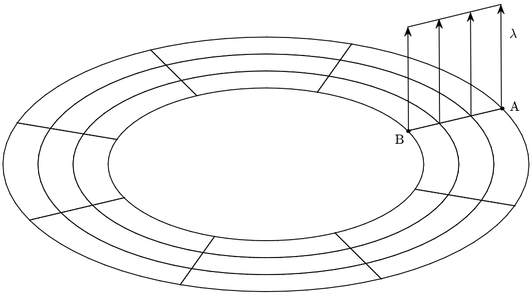

inner radius	6
external radius	10
thickness	0.03
E	$2.1 \cdot 10^3$
ν	0.0

Figure 4.8: Circular ring: geometry

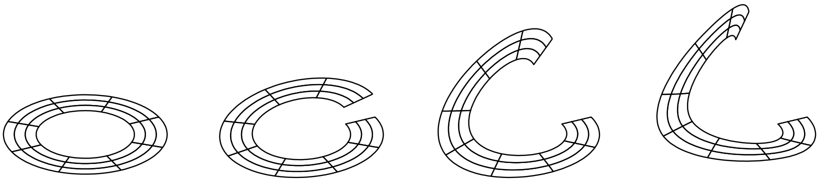

$\lambda = 0.00$ $\lambda = 0.04$ $\lambda = 0.36$ $\lambda = 0.64$

Figure 4.9: Circular ring: evolution of the deformed shape.

4.4.1 Slit annular plate subjected to line force

The first test is a circular ring undergoing large displacements, a very popular benchmark in geometrically nonlinear analysis [11, 13]. Geometry, load and boundary conditions are reported in Fig.4.8. Figure 4.10 shows the equilibrium path of the ring obtained using C^0-HS and C^2-S_1^4. Three meshes are considered for C^0-HS: 10×6 (420 DOFs), 20×6 (840 DOFs) and 30×6 (1260 DOFs) elements. The FE needs the finest mesh to obtain a converged curve, while C^2-S_1^4 provides the same curve with a mesh of 8×3 (576 DOFs). This is mainly due to an exact description of the circular geometry provided by the isogeometric formulation regardless of the mesh adopted. Conversely, the C^0-HS, in the case of curved shell, suffers when coarse meshes are employed, because of the linearised geometry. Observing the equilibrium path in Fig.4.10, obtained using a load-controlled scheme, as well as the evolution of the deformed configuration depicted in Fig.4.9, this nonlinear problem seems easy to solve. However, if we look at Table 4.2, reporting the total number of iterations vs the number

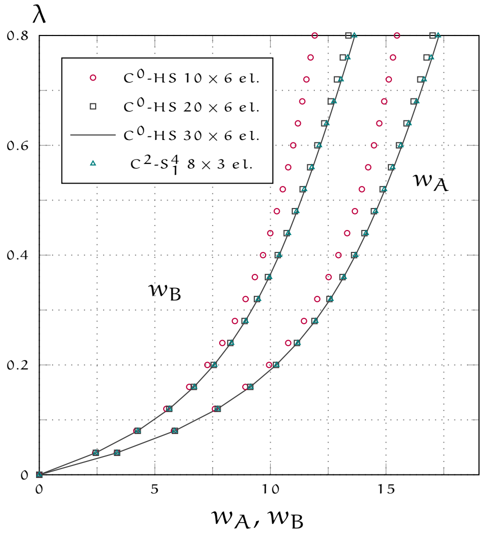

Figure 4.10: Circular ring: equilibrium path.

of equal load increments Nsteps used to reach the maximum load value, it is clear that the standard full Newton method is unable to converge unless a large number of load subdivisions is employed. On the other hand, the MIP Newton easily converges even if the maximum load is reached using just one step. The MIP modified Newton fails for the largest step size, but is much more robust than the standard full Newton. Furthermore, when Nsteps increases, the total number of iterations of the MIP modified Newton is practically the same as the standard Newton and, so, the modified version actually becomes the most convenient. Finally, even for the largest value of Nsteps the MIP Newton is about three times more efficient than the standard Newton.

Table 4.2: Slit annular plate: total number of iterations for the evaluation of the equilibrium path vs the number of load subdivisions.

	Newton	MIP Newton	MIP M. Newton
Nsteps	iters	iters	iters
1	fails	8	fails
5	fails	19	47
10	fails	33	41
20	fails	55	60
30	202	73	74

Table 4.3: The pinched cylinder: total number of steps, iterations and normalised elapsed time for the evaluation of the equilibrium path with C^2-S_1^4.

	Newton		MIP Newton			MIP M. Newton		
mesh	steps	iters	steps	iters	elapsed time*	steps	iters	elapsed time*
50×50	127	507	61	235	0.47	89	352	0.24

∗ normalised with respect to Newton elapsed time.

4.4.2 The pinched cylinder

Another interesting test regarding large deformations is the pinched cylinder depicted in Fig.4.11, that has been studied by several authors [11, 76]. Exploiting the problem symmetries only an eighth of the cylinder is analysed using C^2-S_1^4 and C^0-HS. The equilibrium path of the cylinder is reported in Fig.4.12. Three uniform meshes are considered for C^2-S_1^4. The coarsest one 30×30 (6208 DOFs) already furnishes a good curve, which, however, is not smooth but exhibits fluctuations. This phenomenon is already known in literature in both the FE [77] and IGA [76] context when coarse meshes are employed. It is due to wrinkles developing and moving during the loading process, as can be noted looking at the evolution of the deformed configuration in Fig.4.13. The second mesh adopted for C^2-S_1^4 is 40×40 (10668 DOFs), which provides a smoother curve that is practically coincident with that provided by the 50×50 mesh (16328 DOFs). Finally the C^0-HS results obtained with two meshes is also reported. The 40×40 mesh (9680 DOFs) gives a good prediction but presents a clear discretisation error, which slowly decreases by refining the mesh. In fact, the curve given by the 75×75 mesh (33900 DOFs) tends towards the isogeometric curve. Again, as in the previous test, C^2-S_1^4 converges quickly to the most likely solution because of the exact geometry, while C^0-HS is probably penalised by the linearised representation of the curved geometry.

The equilibrium path is obtained using an arc-length path-following analysis with the Riks constraint and an adaptive step size. The total number of steps and iterations required by the different iterative strategies are illustrated in Table 4.3. It is also reported the elapsed time, normalised with respect to that required by the standard Newton strategy. Even in this test, the MIP Newton outperforms the standard Newton, particularly in the modified version that is clearly the most efficient choice.

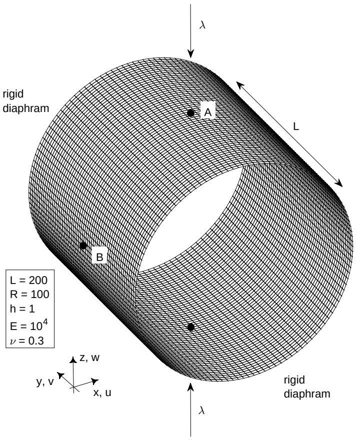

Figure 4.11: The pinched cylinder: geometry

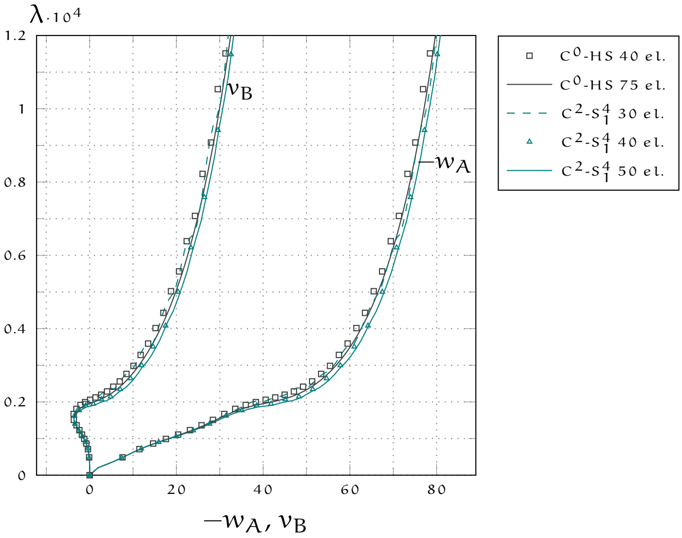

Figure 4.12: Pinched cylinder: equilibrium path.

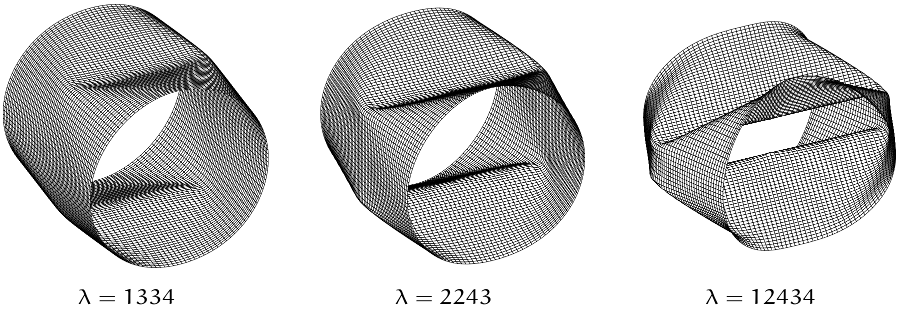

Figure 4.13: Pinched cylinder: evolution of the deformed configuration.

4.4.3 Clamped semi-cylinder

While the results presented so far regard isotropic materials, this benchmark tests the proposed solid-shell model and the MIP Newton in the case of a composite multi-layered shell. The structure is a semi-cylinder loaded by a concentrated force at the middle of one of the curved edges, while the other one is clamped. The vertical displacement of the straight edges is constrained. In Fig.4.15, the geometry and the boundary conditions are depicted. Due to its symmetry, only a half of the structure is analysed. Two cases are considered: isotropic material, characterised by $E = 2068.50$ and $\nu = 0.3$, and a composite multi-layered material. The local reference system, used for defining the material proprieties, has the direction 1 aligned with the y of the global system and the direction 3 is the normal to the surface from inside out. The stacking sequences of the laminated material are [90/0/90] and [0/90/0], measured with respect to the direction 1 of the local reference system and the material properties are $E_1 = 2068.50$, $E_2 = E_3 = 517.125$, $\nu_{12} = \nu_{23} = \nu_{13} = 0.3$ and $G_{12} = G_{23} = G_{13} = 759.58$.

Figure 4.14 shows the equilibrium paths obtained using the element C^2-S_1^4 and for the different material cases analysed. Two uniform meshes of 20×20 elements (2948 DOFs) and 30×30 elements (6208 DOFs) are used. The results of the coarse mesh are practically identical to those obtained with the finer one, except for the case [90/0/90] which exhibits small fluctuations, similar to the previously analysed pinched cylinder, which disappear when the finer mesh is employed. This behaviour is again related to the development of wrinkles as can be observed in the deformed shape at the last evaluated equilibrium point, pictured in Fig.4.15. The results, in both the isotropic and composite cases, can

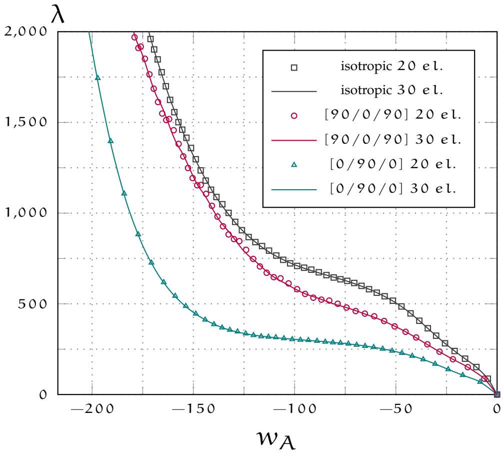

Figure 4.14: Clamped semi-cilinder: equilibrium paths with element C^2-S_1^4 for different meshes and layups.

be compared with the solutions obtained by Abaqus, reported in [78], which are the same as the present ones. Also in this benchmark, the robustness of the MIP strategy is evident. Table 4.4 shows how MIP strategy drastically reduces the number of iterations required to trace the equilibrium path and how MIP modified Newton is the most convenient choice in terms of computational time.

Lastly, Fig.4.16 shows two significant generalised stress components evaluated with a mesh of 30 × 30 C^2-S_1^4 elements (6208 DOFs) compared with a reference solution obtained with C^0-HS and a mesh of 60 × 60 elements (21720 DOFs).

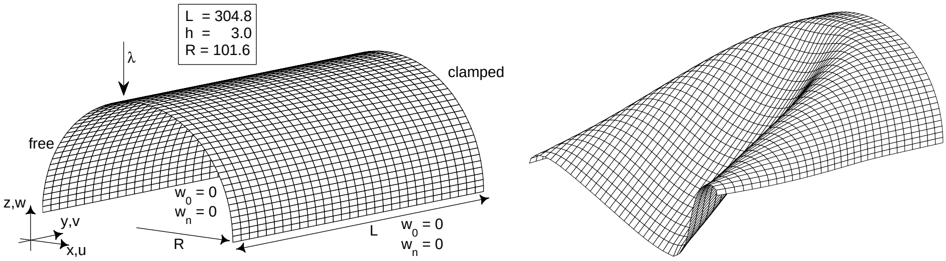

Figure 4.15: Clamped semi-cylinder: geometry and deformed configuration at the last evaluated equilibrium point for [90/0/90] .

Table 4.4: Clamped semi-cylinder: total number of steps and iterations for the evaluation of the equilibrium path using 30×30 C^2-S_1^4 elements.

	Newton		MIP Newton			MIP M. Newton		
layup	steps	iters	steps	iters	elapsed time*	steps	iters	elapsed time*
isotropic	95	382	37	138	0.36	55	216	0.20
[0/90/0]	64	253	32	113	0.44	51	195	0.27
[90/0/90]	92	380	36	142	0.37	62	255	0.23

∗ normalised with respect to Newton elapsed time.

The concentrated force causes a singularity in the 3D continuum model. The maximum value of the color map of $\mathcal{N}_1$ is then limited to make the comparison clearer over the structure by leaving the singular values just under the force out, which are also mesh-dependent.

4.5 IGA KOITER RESULTS

The proposed numerical tool is now tested in common composite structures, such as plates, panels and cylinders. The first goal is to test the accuracy of the isogeometric solid-shell model in representing the buckling and postbuckling configuration. To this end, different meshes and numerical integrations are considered for C_1-quadratic and C_2-cubic NURBS interpolations of the displacement field over the middle surface of the shell. The second goal is to assess the accuracy of the ROM built with the proposed MIP isogeometric formulation of Koiter's method by comparing the results with reference solutions obtained by path-following analyses based on the full model.

4.5.1 Composite square plate

The first test, depicted in Fig.4.17, is a simply supported laminated plate under compression loading. The material properties are reported in Table 4.5. The layup adopted is $[0°/90°]_{4S}$. The test has been studied in [30] using shell elements and in [79] by a Ritz method. Firstly, the accuracy of the proposed isogeometric solid-shell model is tested in the evaluation of the four lowest buckling loads, which are reported in Table 4.6 and Table 4.7 for the C_1 and the C_2 interpolation respectively. The corresponding buckling modes are pictured in Fig.4.18. Different integration schemes are considered as well as the local

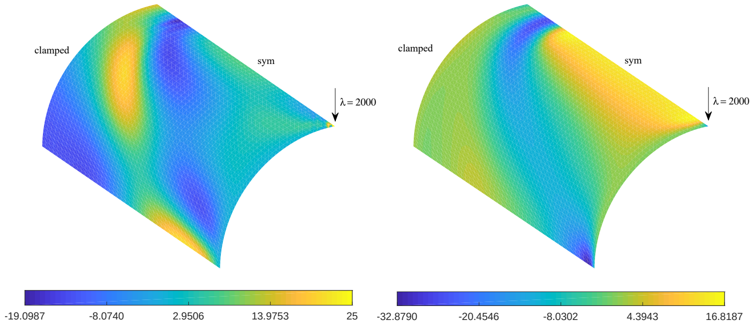

$\mathcal{N}_1$, C^2-S_1^4 30×30 elements

$\mathcal{M}_1$, C^2-S_1^4 30×30 elements

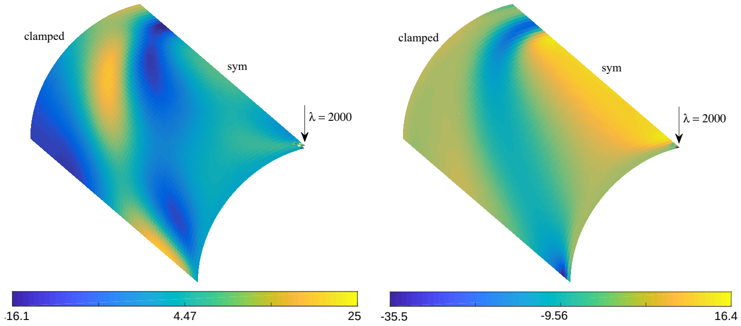

$\mathcal{N}_1$, C^0-HS 60×60 elements

$\mathcal{M}_1$, C^0-HS 60×60 elements

Figure 4.16: Clamped semi-cylinder: generalised stresses at $\lambda = 2000$, layup [0/90/0].

Table 4.5: Composite square plate: material properties.

E_{11}	$E_{22} = E_{33}$	$\nu_{12} = \nu_{13}$	ν_{23}	$G_{12} = G_{13}$	G_{23}
$181 \cdot 10^9$	$10.27 \cdot 10^9$	0.28	0	$7.17 \cdot 10^9$	$5.135 \cdot 10^9$

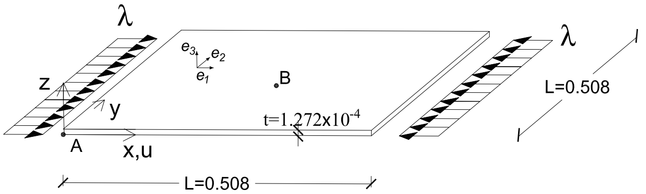

Figure 4.17: Composite square plate: geometry, load and boundary conditions.

Table 4.6: Composite square plate: first 4 normalised buckling loads for C_1 interpolation.

4 elm.				8 elm.				16 elm.			
$\bar{S}_0^2$	S_0^3	S_0^4	ANS	$\bar{S}_0^2$	S_0^3	S_0^4	ANS	$\bar{S}_0^2$	S_0^3	S_0^4	ANS
1.010	1.004	1.185	1.184	1.000	1.002	1.179	1.121	1.000	1.000	1.113	1.006
1.367	*	*	1.483	1.007	1.073	*	1.439	1.000	1.006	1.561	1.064
1.348	*	*	1.457	1.006	1.071	*	1.422	1.000	1.006	1.648	1.076
1.328	*	*	1.636	1.022	1.015	*	1.591	1.000	1.007	*	1.188

$* > 2$

ANS proposed in [13]. In particular, Table 4.6 shows the good performance of $\bar{S}_0^2$, which turns out to be the best integration among those considered in terms of both accuracy and efficiency, providing good results for the 8×8 mesh and requiring just ≈ 1 integration point per element. Conversely, ANS and the full integration S_0^4, which require 9 and ≈ 4 integration points per element respectively, prove to be inaccurate because of the interpolation locking. It increases with the slenderness of the plate and slowly vanishes when the mesh is refined. Moreover, Table 4.7 shows the advantages of a higher continuity in buckling problems, showing that the C_2 interpolation with $\bar{S}_1^3$ and, in particular, S_1^4 integration provides good results even using a 4×4 mesh. $\bar{S}_1^3$ requires ≈ 1 integration point per element but is slightly penalised for coarse meshes by the over-integration, while S_1^4 furnishes exact results for a 8×8 mesh and makes use of ≈ 2.25 integration points per element. The full integration S_1^6, making use of ≈ 6.25 integration points per element, is unusable due to locking phenomena that also hold for the finest mesh.

The equilibrium path in the pre-critical and initial post-critical range is reconstructed using the Koiter method and reported in Fig.4.19 for C_1 and Fig.4.20 for C_2. A small geometrical imperfection $\tilde{e}$ with the shape of the first buckling mode and $\|\tilde{e}\|_\infty = 0.01t$ is considered. In addition, a reference solution obtained using a very fine mesh and the standard Riks method, which solves step-by-step the nonlinear equations of the full discrete model, is reported. For this test,

Table 4.7: Composite square plate: first 4 normalised buckling loads for C_2 interpolation.

4 elm.			8 elm.			16 elm.		
$\bar{S}_1^3$	S_1^4	S_1^6	$\bar{S}_1^3$	S_1^4	S_1^6	$\bar{S}_1^3$	S_1^4	S_1^6
1.003	1.000	1.185	1.000	1.000	1.170	1.000	1.000	1.028
1.031	1.030	1.479	1.003	1.000	1.473	1.000	1.000	1.240
1.034	1.028	1.451	1.004	1.000	1.446	1.000	1.000	1.255
1.139	1.012	1.618	1.016	1.002	1.614	1.001	1.000	1.412

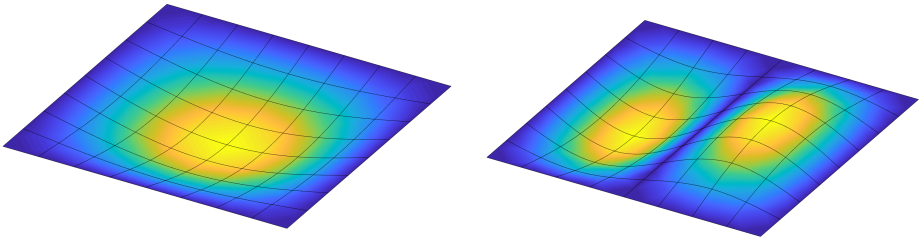

mode 1

mode 2

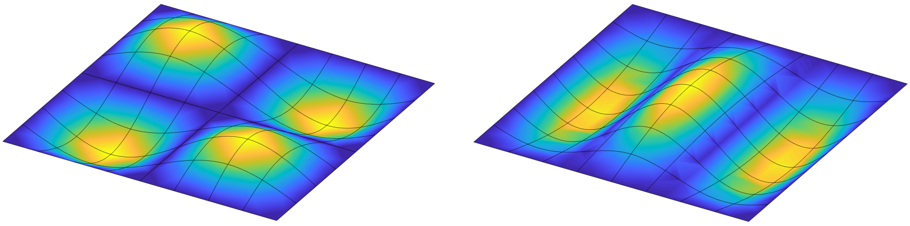

mode 3

mode 4

Figure 4.18: Composite square plate: first 4 buckling modes.

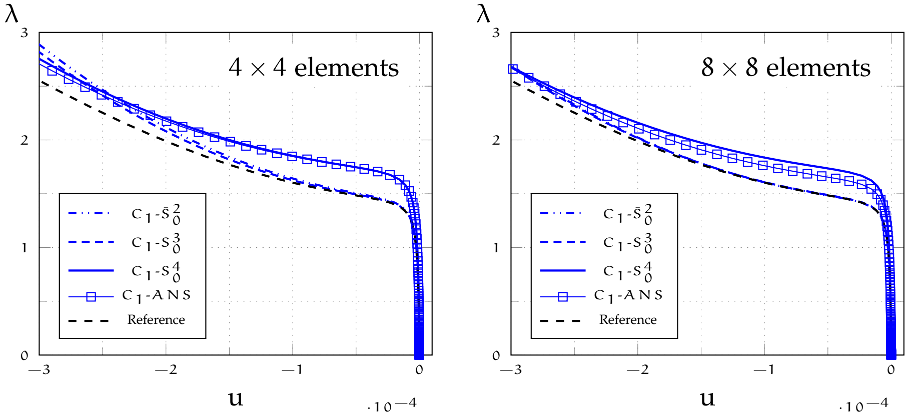

Figure 4.19: Composite square plate: equilibrium path using the C_1 interpolation

just one buckling mode is used in the ROM of the Koiter method which, then, requires that only one nonlinear equation be solved. Looking at Fig.4.19 we can note that, although the bifurcation point is almost exact using C_1-$\bar{S}_0^2$, a 4×4 mesh exhibits a stiffer post-buckling response compared to the reference solution as consequence of interpolation locking of the linear and quadratic strains. However, the error becomes much lower by considering a 8×8 mesh. Figure 4.20, on the other hand, highlights the benefits of a higher continuity: C_2-$\bar{S}_1^3$ and C_2-S_1^4 agree very well with the reference path also for the coarsest mesh.

As a general comment, a drastic reduction in the number of DOFs is achieved with respect to the locking free linear shell elements used in [30] for the same test.

4.5.2 Composite curved panel

The second test regards a curved panel under compression loading whose geometry, loads, and boundary conditions are represented in Fig.4.21. The material properties can be found in Table 4.8. Two different layups are considered: $[0]_6$ and $[45, -45, 0]_s$. The lamination significantly influences the shape of the buckling modes as illustrated in Fig.4.22. The slenderness of the panel is much lower than that of the previous test. This means that the effects of the interpolation locking are less evident. This is confirmed by Tables 4.9, 4.10, 4.11 and 4.12 which show the convergence of the first 4 linearised buckling loads. The high

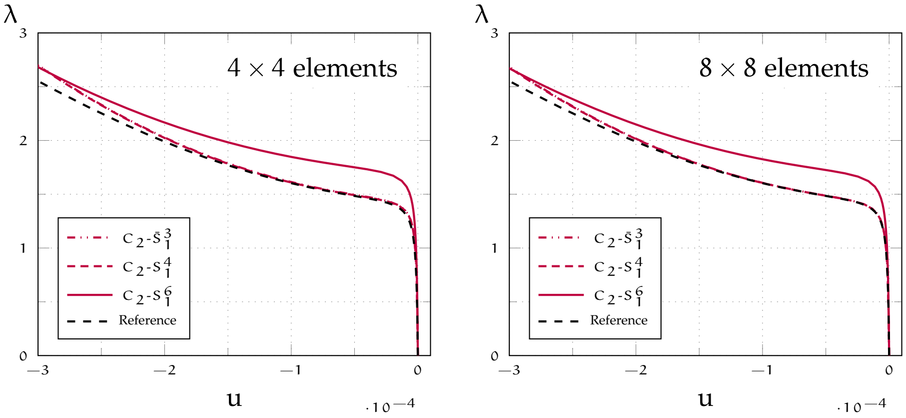

Figure 4.20: Composite square plate: equilibrium path using the C_2 interpolation

Table 4.8: Composite curved panel: material properties.

E_{11}	$E_{22} = E_{33}$	$\nu_{12} = \nu_{13}$	ν_{23}	$G_{12} = G_{13}$	G_{23}
30.6	8.7	0.29	0.5	3.24	2.9

continuity together with the exact representation of the geometry leads to very good results with all the integration strategies. Again, however, the $\bar{S}_0^2$ for C_1 and S_1^4 and $\bar{S}_1^3$ for C_2 represent the best choices in terms of accuracy and efficiency.

The study of the initial post-buckling behaviour of the panel is carried out considering the presence of a geometrical imperfection $\tilde{e}$ that is a combination of the first and the second buckling modes. In particular, it is the difference between them scaled in order to obtain $\|\tilde{e}\|_\infty = 0.1t$. The Koiter solution is

Table 4.9: Composite curved panel: first 4 normalised buckling loads for $[0]_6$ with C_1 interpolation.

4 elm.				8 elm.				16 elm.			
$\bar{S}_0^2$	S_0^3	S_0^4	ANS	$\bar{S}_0^2$	S_0^3	S_0^4	ANS	$\bar{S}_0^2$	S_0^3	S_0^4	ANS
1.053	1.055	1.078	1.042	1.002	0.998	1.020	1.008	0.995	0.995	0.998	0.996
1.158	1.424	1.694	1.177	1.005	1.008	1.069	1.018	0.996	0.998	1.003	0.997
1.259	1.609	*	1.299	1.009	1.035	1.124	1.039	1.003	1.004	1.012	1.003
1.408	1.746	*	1.396	1.007	1.061	1.213	1.067	1.003	1.005	1.020	1.004

$* > 2$

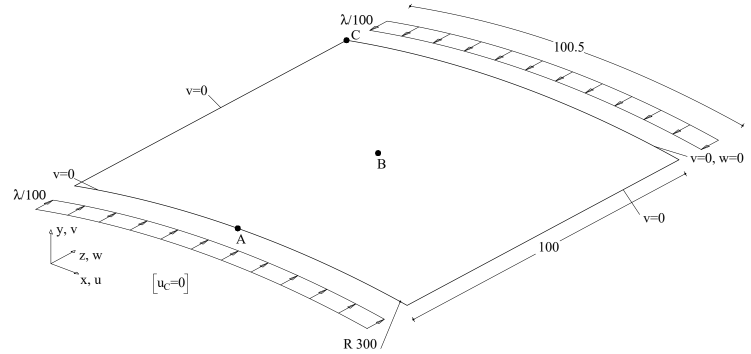

Figure 4.21: Composite curved panel: geometry and boundary conditions.

Table 4.10: Composite curved panel: first 4 normalised buckling loads for $[45, -45, 0]_s$ with C_1 interpolation.

4 elm.				8 elm.				16 elm.			
$\bar{S}_0^2$	S_0^3	S_0^4	ANS	$\bar{S}_0^2$	S_0^3	S_0^4	ANS	$\bar{S}_0^2$	S_0^3	S_0^4	ANS
1.096	1.144	1.263	1.165	1.016	1.018	1.095	1.054	1.001	1.002	1.015	1.004
1.082	1.201	1.656	1.106	1.013	1.010	1.078	1.036	0.998	0.999	1.011	1.001
1.080	1.346	$*$	1.333	1.007	1.010	1.157	1.061	0.998	0.999	1.010	0.999
1.235	1.456	$*$	1.848	1.035	1.073	1.228	1.119	1.003	1.012	1.049	1.011

$* > 2$

Table 4.11: Composite curved panel: first 4 normalised buckling loads for $[0]_s$ with C_2 interpolation.

4 elm.			8 elm.			16 elm.		
$\bar{S}_1^3$	S_1^4	S_1^6	$\bar{S}_1^3$	S_1^4	S_1^6	$\bar{S}_1^3$	S_1^4	S_1^6
0.995	1.034	1.031	1.001	1.005	1.004	1.001	1.002	1.001
1.000	1.013	1.073	1.001	1.004	1.003	1.001	1.001	1.001
1.008	1.063	1.132	1.003	1.008	1.007	1.002	1.003	1.003
1.014	1.104	1.210	1.004	1.009	1.010	1.002	1.003	1.003

Table 4.12: Composite curved panel: first 4 normalised buckling loads $[45, -45, 0]_s$ with C_2 interpolation.

4 elm.			8 elm.			16 elm.		
$\bar{S}_1^3$	S_1^4	S_1^6	$\bar{S}_1^3$	S_1^4	S_1^6	$\bar{S}_1^3$	S_1^4	S_1^6
0.995	1.097	1.110	1.006	1.014	1.018	1.002	1.005	1.004
1.014	1.044	1.068	1.006	1.012	1.015	1.001	1.003	1.003
1.002	1.121	1.167	1.003	1.007	1.014	1.001	1.003	1.002
1.062	1.205	1.280	1.041	1.022	1.061	1.001	1.003	1.003

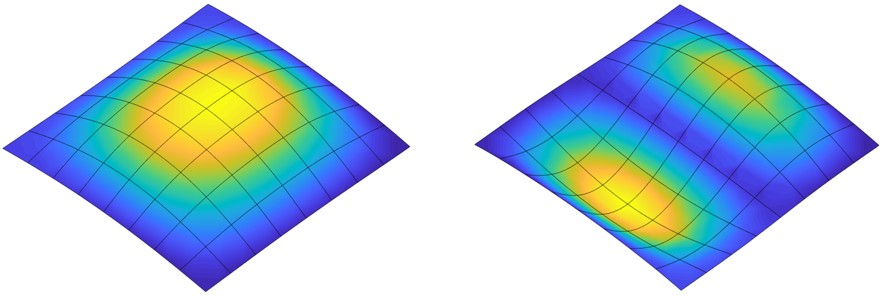

mode 1 $[0]_6$

mode 2 $[0]_6$

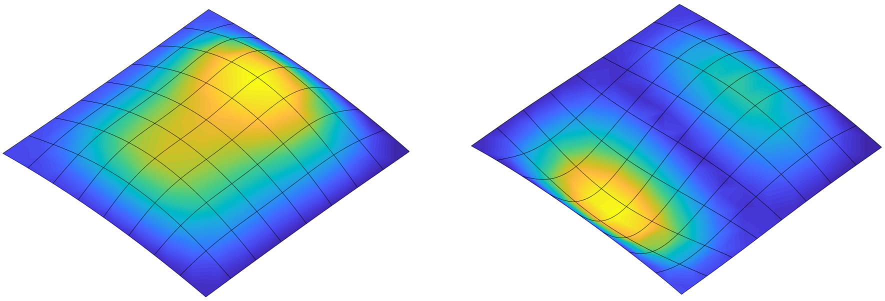

mode 1 $[45/-45/0]_s$

mode 2 $[45/-45/0]_s$

Figure 4.22: Composite curved panel: first and second buckling mode corresponding to two different layups

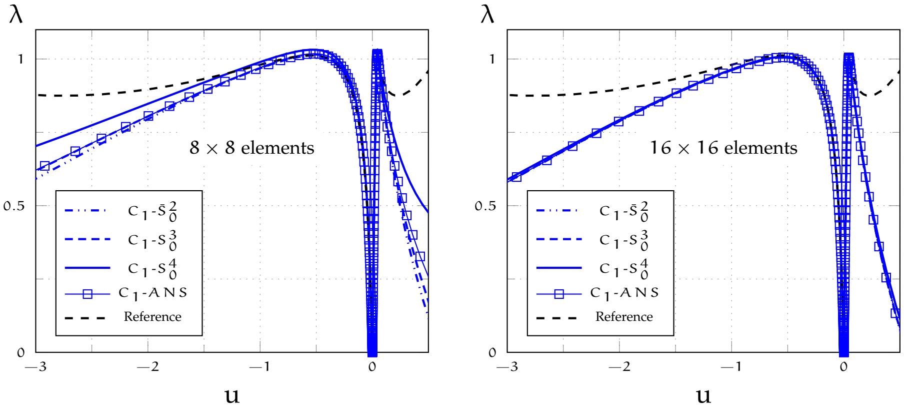

Figure 4.23: Composite curved panel: equilibrium path for $[0]_6$ and C_1 interpolation

evaluated using a ROM based on the first two buckling modes only, since the higher ones are far from the first two, and it is compared with reference paths obtained using a very fine mesh and the standard Riks method for solving the nonlinear equations of the full model. For both the layups, the initial post-buckling exhibits a limit load as shown in Fig.4.23 and Fig.4.24 for $[0]_6$ and in Fig.4.25 and 4.26 for $[45, -45, 0]_s$. C_1-$\bar{S}_0^2$, C_2-$\bar{S}_1^3$ and C_2-$\bar{S}_1^4$ are the best performing strategies, providing a good estimate of the limit loads with a 8 × 8 mesh, which became practically exact using a 16 × 16 mesh. Clearly, the Koiter solution differs from the full nonlinear one for very large displacements since the ROM is built for the estimation of the initial post-buckling behaviour.

4.5.3 Composite cylinder in compression

The cylinder considered in the following and labelled Z33 was manufactured and tested by DLR (German Aerospace Center) and commonly used as a validation model for numerical developments in the context of laminate composite shell design [53, 80]. The stacking sequence is $_{in}[0/0/19/-19/37/-37/45/-45/51/-51]_{out}$ with the angles measured from the cylinder axis with respect to the outward normal. The cylinder has a height of 510, a radius of $R = 250$ and a wall-thickness of $t = 1.25$. The material properties are reported in Table 4.13

The cylinder is clamped at the bottom face and only the axial translation is allowed at the top surface. A uniformly distributed load along the top rim is applied in axial direction. The lowest buckling loads of the perfect structure

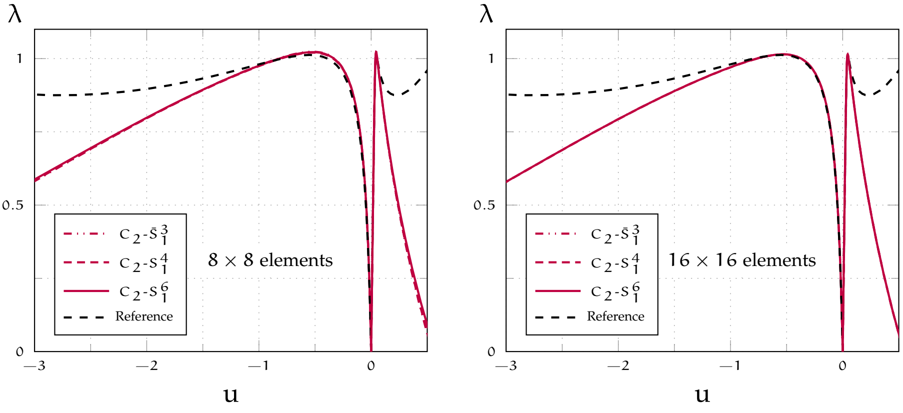

Figure 4.24: Composite curved panel: equilibrium path for $[0]_6$ and C_2 interpolation

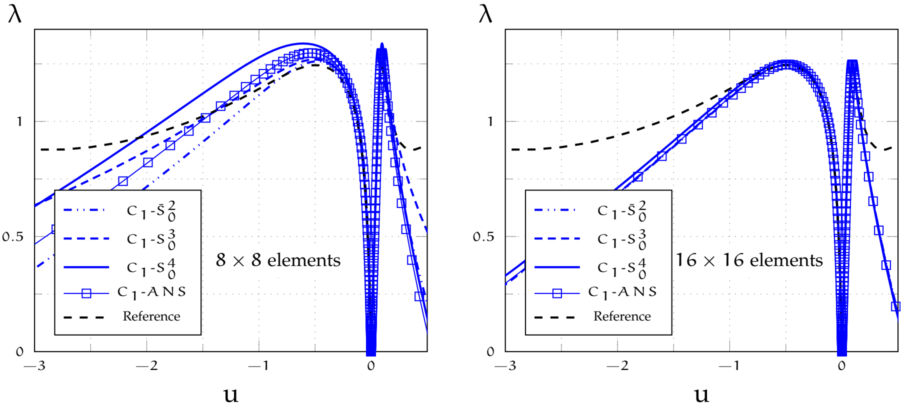

Figure 4.25: Composite curved panel: equilibrium path for $[45/-45/0]$ and C_1 interpolation

Table 4.13: Laminate composite cylinder: material properties.

E_{11}	$E_{22} = E_{33}$	ν_{12}	$\nu_{23} = \nu_{13}$	$G_{12} = G_{13} = G_{23}$
123.6	8.7	0.32	0	5.7

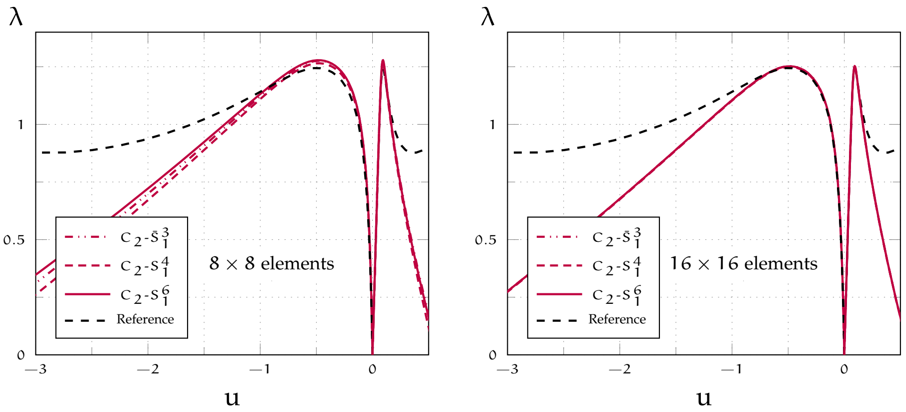

Figure 4.26: Composite curved panel: equilibrium path for [45/−45/0] and C_2 interpolation

Table 4.14: Laminate composite cylinder: first 4 normalised buckling loads with C_1 interpolation.

12 elm.				24 elm.				48 elm.			
$\bar{S}_0^2$	S_0^3	S_0^4	ANS	$\bar{S}_0^2$	S_0^3	S_0^4	ANS	$\bar{S}_0^2$	S_0^3	S_0^4	ANS
0.957	1.594	∗	1.658	1.003	1.041	1.200	1.056	1.000	1.002	1.015	1.001
0.960	1.596	∗	1.664	1.006	1.046	1.200	1.059	1.000	1.002	1.015	1.001
0.959	1.618	∗	1.661	1.005	1.044	1.200	1.060	1.000	1.002	1.014	1.001
0.962	1.618	∗	1.719	1.007	1.048	1.208	1.060	1.000	1.002	1.014	1.001

∗ > 2

are reported in Table 4.14 and Table 4.15 for the C_1 and the C_2 interpolation respectively. The corresponding buckling modes are depicted in Fig.4.27. Due to problem symmetries they occur in couples. Also for this test, C_1-$\bar{S}_0^2$, C_2-$\bar{S}_1^3$ and C_2-S_1^4 turn out to be particularly accurate and provide good results with a relatively coarse mesh in comparison with those usually employed in the FE literature [81].

In evaluating the initial post-buckling behaviour a load imperfection is introduced by a concentrated force halfway up the cylinder axis. By including just one mode in the ROM, a good prediction of the limit load is obtained as shown in Fig.4.28 and confirmed by the comparison with the reference solution obtained using a very fine mesh and a fully nonlinear analysis.

Table 4.15: Laminate composite cylinder: first 4 normalised buckling loads with C_2 interpolation.

12 elm.			24 elm.			48 elm.		
$\bar{S}_1^3$	S_1^4	S_1^6	$\bar{S}_1^3$	S_1^4	S_1^6	$\bar{S}_1^3$	S_1^4	S_1^6
1.156	1.120	1.245	1.003	1.011	1.007	1.000	1.001	1.000
1.176	1.127	1.245	1.003	1.011	1.007	1.000	1.001	1.000
1.175	1.150	1.266	1.002	1.012	1.006	1.000	1.001	1.000
1.183	1.150	1.278	1.002	1.012	1.006	1.000	1.001	1.000

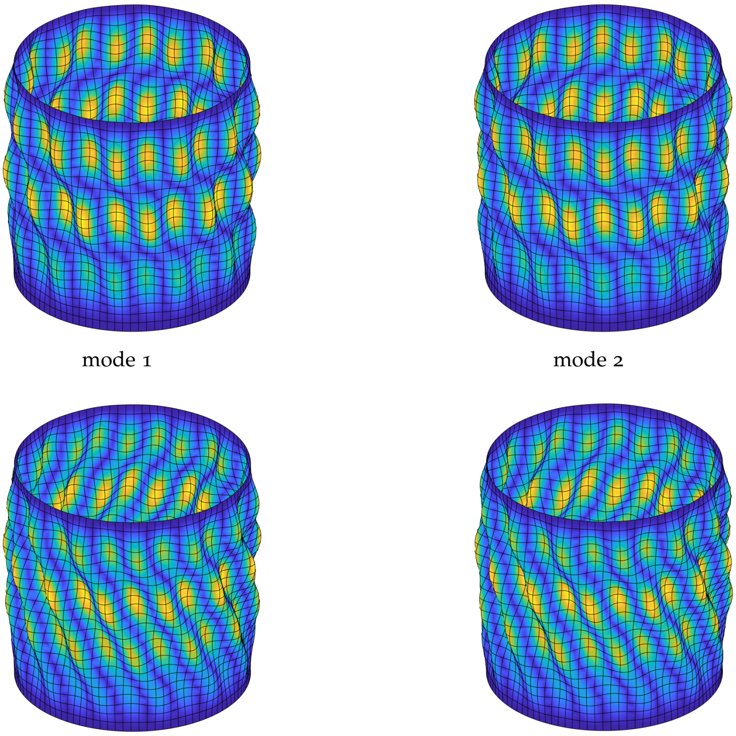

mode 1

mode 2

mode 3

mode 4

Figure 4.27: Laminate composite cylinder: first 4 buckling modes.

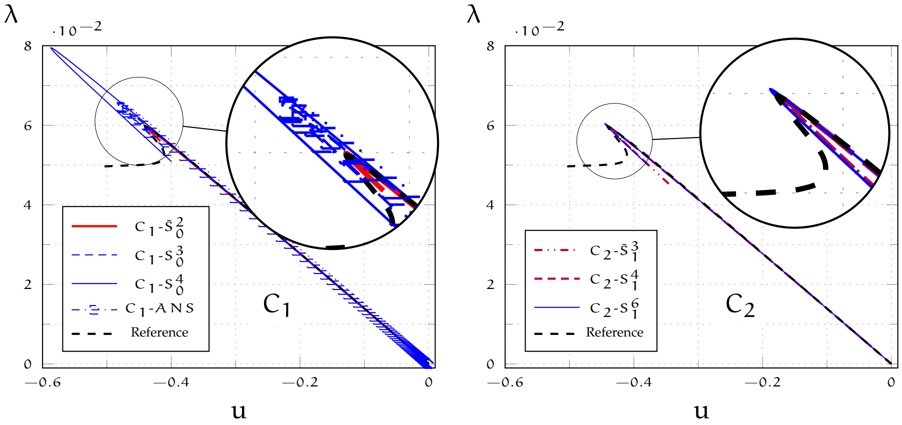

Figure 4.28: Laminate composite cylinder: equilibrium path using a 24 × 96 mesh

5 ACCOUNTING FOR GEOMETRICAL IMPERFECTIONS

One of the interesting aspects of Koiter's method is the possibility of evaluating the effect of many imperfections within the same analysis and without increasing the computational time. As a consequence, the result of a Koiter analysis will be not only a single equilibrium path, but a more complete information that includes the worst equilibrium path. This is of paramount importance, because, due to modal buckling interaction, shell-like structures may exhibit unstable post-buckling behaviour and may be highly sensitive to initial imperfections [82–86], especially to geometrical defects. In more detail, we will deal, from now on, with geometrical imperfections evaluated as linear combination of buckling modes and when talking about worst imperfection we will refer to the worst geometrical imperfection among those evaluated as buckling modes combinations. In this context, Koiter's method has already been used to perform imperfection sensitivity analyses [8, 43, 87, 88] for slender structures of different kinds. However, Koiter's method can give us the opportunity to control the imperfection sensitivity during an optimisation process. In fact, it is well documented [89] that an optimisation process that does not account for imperfection sensitivity can produce naive optimised solutions, namely structures that give optimal performance only if perfectly manufactured and could be highly unstable otherwise.

Obviously, the effects of geometrical imperfections can be included in the Koiter analysis a-priori in the model, like in the standard path-following approach. Although also in this case the analysis would be cheaper than path-following, the real strength of Koiter's method is the possibility of including a-posteriori the effects of the imperfections. This means that their effect is included in the reduced model of the structure without imperfections, built once and for all, by simply adding some energy terms in the reduced system. The extra computational cost regards only the construction of the energy term related to the imperfection and the solution of the reduced system for each imperfection, that represents a negligible fraction of the overall analysis. Nevertheless, the state-of-the-art a-posteriori account of geometrical imperfections is based on the hypothesis of linear pre-critical behaviours and small imperfection amplitudes, that leads to additional terms in the reduced system which are just linear in the load factor. As a consequence, inaccuracies occur even for small pre-critical non-linearities and significant imperfection amplitudes [8], considerably limiting the application of the method.

The goal is to overcome the limits of the approach. To this purpose, a new accurate treatment of the geometrical imperfections is proposed. The asymptotic expansion of the perfect structure is corrected by adding a series of new modes, generated by the imperfection. In this way a more accurate formula for the additional imperfection terms in the reduced system is derived, which coherently takes into account the effects of the geometrical imperfection up to the 2nd order, without losing the advantages of the a-posteriori account.

5.1 FORMULATION OF KOITER'S METHOD

In this section the formulation of Koiter's method with the new treatment of geometrical imperfection is proposed. The mixed solid-shell model is employed, even if the approach can be extended to classic shell models.

5.1.1 The strain energy

Using a Hellinger-Reissner variational principle the mixed strain energy $\Phi[u]$ is expressed as a sum of element contributions

$$\Phi[u] = \sum_e \int_{\Omega_e} \left(\boldsymbol{\sigma}^T \varepsilon[\mathbf{d}] - \frac{1}{2} \boldsymbol{\sigma}^T \mathbf{C}^{-1} \boldsymbol{\sigma} \right) d\Omega_e \tag{5.1}$$

$\varepsilon[\mathbf{d}]$ and $\boldsymbol{\sigma}$ are the vectors collecting the generalised strains and stresses components for the given structural model, see. 2.1.3, Ω_e is the finite element domain and $\mathbf{d}$ is the displacement field and $\mathbf{C}^{-1}$ the compliance matrix of the structural model.

The strain energy of the structure for an initial imperfection characterised by an assigned displacement $\tilde{\mathbf{d}}$ and zero stress is assumed as

$$\Phi_I[u] \equiv \sum_e \int_{\Omega_e} \left(\boldsymbol{\sigma}^T (\varepsilon[\mathbf{d}] - \varepsilon[\tilde{\mathbf{d}}]) - \frac{1}{2} \boldsymbol{\sigma}^T \mathbf{C}_\rho^{-1} \boldsymbol{\sigma} \right) d\Omega_e. \tag{5.2}$$

Denoting with a symbol δ the variation of $\mathbf{d}$ and $\boldsymbol{\sigma}$, the first variation of $\Phi_I[u]$ becomes

$$\begin{aligned}\Phi_I[u]'\delta u &= \sum_e \int_{\Omega_e} \left\{ \delta\boldsymbol{\sigma}^T(\varepsilon[\mathbf{d}] - \varepsilon[\tilde{\mathbf{d}}] - \mathbf{C}_\rho^{-1}\boldsymbol{\sigma}) - \boldsymbol{\sigma}^T\varepsilon'[\mathbf{d}]\delta\mathbf{d} \right\} d\Omega_e \\ &= \left(\Phi[u]' - \Phi'[\tilde{u}]\right)\delta u\end{aligned} \tag{5.3}$$

that is the difference between the perfect and imperfect structure first order strain energy variation, being

$$\Phi'[\tilde{u}]\delta u = \sum_e \int_{\Omega_e} \delta\boldsymbol{\sigma}^T \varepsilon[\tilde{\mathbf{d}}] d\Omega_e \tag{5.4}$$

the first variation of the perfect structure evaluated in $\tilde{u}$ (which has $\tilde{\boldsymbol{\sigma}} = 0$).

The equilibrium path is obtained from the following condition

$$\left(\Phi[u]' - \Phi'[\tilde{u}] - \lambda p\right)\delta u = 0 \quad \forall \delta u \tag{5.5}$$

which in FE format becomes

$$\mathbf{s}[\mathbf{u}] - \tilde{\mathbf{p}} - \lambda\hat{\mathbf{p}} = 0. \tag{5.6}$$

In particular the internal force vector $\mathbf{s}[\mathbf{u}]$, the load vector $\hat{\mathbf{p}}$ and the imperfection vector $\tilde{\mathbf{p}}$ are defined by the energy equivalences

$$\begin{aligned}\mathbf{s}^T\delta\mathbf{u} &\equiv \Phi'[u]\delta u \ , \\ \hat{\mathbf{p}}^T\delta\mathbf{u} &\equiv \hat{p}\,\delta u \ , \\ \tilde{\mathbf{p}}^T\delta\mathbf{u} &\equiv \Phi'[\tilde{u}]\delta u \ , \quad \forall\,\delta\mathbf{u}.\end{aligned} \tag{5.7}$$

Eq.(5.6) can be solved using standard path-following techniques [14, 16, 49] for an assigned imperfection $\tilde{u}$. Note that in the hybrid solid-shell FE model, the internal force vector of the imperfect structure is obtained by simply subtracting a constant vector $\tilde{\mathbf{p}}$, evaluated once and for all at the beginning of the analysis, to the internal forces vector $\mathbf{s}[\mathbf{u}]$ of the perfect structure.

5.1.2 The new reduced model

The space of admissible configurations that will be used in the Lyapunov-Schmidt decomposition is obtained by adding an additional term which represents the initial imperfection, to the configuration field of the perfect structure in Eq.(3.15) that is

$$u_d[\lambda, \xi_i, \tilde{\xi}_i] = \tilde{u} + \lambda\hat{u} + v[\xi_i] + w[\xi_i, \tilde{\xi}_i, \lambda] \tag{5.8}$$

where the geometrical imperfection is assumed to be a linear combination of a known shape $\bar{u}_i$

$$\tilde{u} = \sum_{i=1}^{n} \tilde{\xi}_i \bar{u}_i. \tag{5.9}$$

The imperfection shapes $\bar{u}_i$ are generic and can be, for example, the displacement part of the buckling modes as well as measured geometrical imperfections. Note that, unlike the reduced model in Eq.(3.22), now the quadratic correctives $w[\xi_i, \tilde{\xi}_i, \lambda]$ depend on the geometrical imperfection amplitudes $\tilde{\xi}_i$.

From now on the 3th order dependence of the strain energy on the configuration variables u (see Eq.(3.10)) will be exploited in order to simplify the exposition.

The residual equation (5.5) is firstly expanded in Taylor series starting from $\tilde{u}$, so obtaining

$$\left(\Phi''[\tilde{u}](u_d - \tilde{u}) + \frac{1}{2}\Phi[\tilde{u}]'''(u_d - \tilde{u})^2 - \lambda\hat{p} \right) \delta u = 0.$$

The first term in previous equation is expanded again from the initial configuration of the perfect structure $(u_0 = 0, \lambda = 0)$

$$\Phi''[\tilde{u}](u_d - \tilde{u})\delta u = (\Phi_0'' + \Phi'''\tilde{u})(u_d - \tilde{u})\delta u$$

and, remembering that $\Phi_0''\hat{u}\delta u = p\delta u$

$$\left(\Phi_0''(v + w) + \frac{1}{2}\Phi'''(\lambda\hat{u} + v + w)^2 + \Phi'''\tilde{u}(\lambda\hat{u} + v + w) \right) \delta u = 0. \tag{5.10}$$

With a further Taylor expansion of $\Phi_0''(\cdot)$ starting from the $u_k = \lambda_k\hat{u}$ and letting $\Phi_k'' = \Phi''[u_k]$

$$\Phi_0''(v + w)\delta u = (\Phi_k''(v + w) - \lambda_k\Phi'''\hat{u}(v + w))\delta u$$

Eq. (5.10) becomes

$$\begin{aligned} &\left(\Phi_k''(v + w) + (\lambda - \lambda_k)\Phi'''\hat{u}(v + w) + \frac{1}{2}\lambda^2\Phi'''\hat{u}^2 \right. \\ &\left. + \frac{1}{2}\Phi'''(v + w)^2 + \Phi'''\tilde{u}(\lambda\hat{u} + v + w) \right) \delta u = 0. \end{aligned} \tag{5.11}$$

It is worth mentioning again that Eq.(5.11) does not contain any truncation error. Furthermore note that the equilibrium condition for the structure with no imperfection is regained for $\tilde{u} = 0$.

5.1.3 Projection of the equilibrium equation into the space $\mathcal{W}$

The corrective field $w \in \mathcal{W}$ is obtained by projecting Eq.(5.11) into direction δw, i.e. assuming $\delta u = \delta w$, and expanding it in Taylor series up to the second order in the asymptotic parameters $(\lambda, \xi_i, \tilde{\xi}_i)$. The term $\Phi''_k \dot{v} \delta w$, by exploiting the bifurcation $\Phi''_i \dot{v}_i \delta u = 0$ and the orthogonality $\Phi''' \hat{u} \dot{v}_i \delta w = 0$ conditions, becomes

$$\Phi''_k \dot{v} \delta w = \sum_{i=1}^{n} \xi_i \left\{ \Phi''_i \dot{v}_i + (\lambda_k - \lambda_i) \Phi''' \hat{u} \dot{v}_i \right\} \delta w = 0$$

that allows the simplification of the residual equation as

$$\begin{aligned} \tilde{r}_w[\xi_i, \lambda, \tilde{\xi}] \equiv \Big\{ & \Phi''[\lambda \hat{u}] w + \frac{1}{2} \lambda^2 \Phi''' \hat{u}^2 \\ & + \frac{1}{2} \Phi''' (v^2 + 2wv + w^2) + \Phi''' \tilde{u} (\lambda \hat{u} + v + w) \Big\} \delta w = 0 \end{aligned} \tag{5.12}$$

with $\Phi''[\lambda \hat{u}] w = \Phi''_k w + (\lambda - \lambda_k) \Phi''' \hat{u} w$. Assuming

$$\Phi''[\lambda \hat{u}] w \approx \Phi''_b w \quad \text{with} \quad \Phi''_b \equiv \Phi''[\lambda_b \hat{u}]$$

with λ_b a suitable reference value of the bifurcation cluster and maintaining only the terms of the quadratic polynomial order in $\lambda, \xi_i, \tilde{\xi}_i$ the residual equation simplifies as

$$\begin{aligned} \tilde{r}_w[\lambda, \xi_i, \tilde{\xi}_i] \equiv \Big\{ & \Phi''_b w + \frac{1}{2} \lambda^2 \Phi''' \hat{u}^2 \\ & + \frac{1}{2} \Phi''' v^2 + \Phi''' \tilde{u} (\lambda \hat{u} + v) \Big\} \delta w = 0. \end{aligned} \tag{5.13}$$

Remembering the expression of $v[\xi_i]$, the quadratic correctives of the imperfect structure are sums of the correctives for zero imperfections of Eq.(3.17) and of the additional contribution due to the geometrical imperfection

$$w[\xi_i, \tilde{\xi}_i, \lambda] = \frac{1}{2} \lambda^2 \hat{\tilde{w}} + \frac{1}{2} \sum_{i,j} \xi_i \xi_j \ddot{w}_{ij} + \tilde{w} \tag{5.14}$$

where

$$\tilde{w} = \lambda \tilde{\hat{w}} + \sum_i \xi_i \dot{\tilde{w}}_i \tag{5.15}$$

with

$$\tilde{\hat{w}} := \sum_j \tilde{\xi}_j \hat{w}_j, \quad \tilde{\dot{w}}_i := \sum_j \tilde{\xi}_j \dot{w}_{ij}. \tag{5.16}$$

The terms in Eq.(5.16) can be evaluated, once and for all in the perfect structure step of the Koiter analysis, being known the imperfection basis, as

$$\begin{cases} \Phi_b''\hat{w}_i\delta w = -\Phi'''\hat{u}\bar{u}_i\delta w \\ \Phi_b''\dot{w}_{ij}\delta w = -\Phi'''\dot{v}_i\bar{u}_j\delta w \end{cases} \quad \forall \delta w \in \mathcal{W}. \tag{5.17}$$

5.1.4 The new reduced equations

Exploiting the orthogonality condition $\Phi'''\hat{u}w\dot{v}_k = 0$ the kth equilibrium equation, obtained assuming $\delta u = \dot{v}_k$ in Eq.(5.11), becomes

$$\tilde{r}_k \equiv \left((\lambda - \lambda_k)\Phi'''\hat{u}v + \frac{1}{2}\lambda^2\Phi'''\hat{u}^2 + \frac{1}{2}\Phi'''(v+w)^2 + \Phi'''\tilde{u}(\lambda\hat{u} + v + w) \right) \dot{v}_k = 0. \tag{5.18}$$

Substituting the expression of w and v previously obtained, using the mode normalization condition in Eq.(3.13) and maintaining terms in $\lambda, \xi_i, \tilde{\xi}_i$ up to the 3rd polynomial order, the equilibrium equation becomes

$$\tilde{r}_k[\lambda, \xi_i] \equiv r_k[\lambda, \xi_i] + \tilde{\mu}_k[\lambda, \xi_i] = 0, \quad k = 1 \cdots m \tag{5.19}$$

with $r_k[\lambda, \xi_i] = 0$ the kth reduced equilibrium equation in Eq.(3.18) and the new imperfection factor $\tilde{\mu}_k$ defined as

$$\begin{aligned} \tilde{\mu}_k \equiv & \sum_i \xi_i \lambda \Phi''' v_i \tilde{\hat{w}} \dot{v}_k + \frac{1}{2} \sum_{ij} \xi_i \xi_j \left(\Phi''' v_i \tilde{\dot{w}}_j \dot{v}_k + \Phi''' v_j \tilde{\dot{w}}_i \dot{v}_k + \Phi''' \tilde{u} \ddot{w}_{ij} \dot{v}_k \right) \\ & + \lambda \Phi''' \tilde{u}(\hat{u} + \tilde{\hat{w}})\dot{v}_k + \sum_i \xi_i \Phi''' \tilde{u}(\dot{v}_i + \tilde{\dot{w}}_i)\dot{v}_k + \frac{1}{2}\lambda^2 \Phi''' \tilde{u} \tilde{\hat{w}} \dot{v}_k. \end{aligned} \tag{5.20}$$

It is possible to observe that the only change, with respect to the standard reduced system in subsection 3.3.4 regards the imperfection coefficient $\tilde{\mu}_k$ which is now more complex than the one used in Eq.(3.19), which only maintains the linear contribution in λ

$$\tilde{\mu}_k = \lambda \Phi''' \hat{u} \tilde{u} \dot{v}_k$$

while the quadratic terms in λ and the terms in ξ are neglected, leading to inaccuracy as the pre-critical non-linearity increases.

Furthermore, note that the proposed reduced model assumes the following final expression

$$u_d[\lambda, \xi_i, \tilde{\xi}_i] = \tilde{u} + \lambda(\hat{u} + \tilde{\hat{w}}) + \sum_i \xi_i(\dot{v}_i + \dot{\tilde{w}}_i) + \frac{1}{2}\sum_{ij} \xi_i \xi_j \ddot{w}_{ij} + \frac{1}{2}\lambda^2 \hat{\tilde{w}}. \quad (5.21)$$

The new correctives can be seen as a correction to the fundamental path tangent and the buckling modes of the perfect structures in order to take into account the geometrical imperfection.

5.1.5 Implementation of the proposed algorithm

The construction of the reduced model of the perfect structure presented in chapter 3 is completed by adding the evaluation of the new corrective at the reduced system of equilibrium equations

$$\begin{cases} \mathbf{K}_b \dot{\tilde{\boldsymbol{w}}}_{ij} + \tilde{\mathbf{p}}_{ij} & = 0 \\ \mathbf{K}_b \hat{\tilde{\boldsymbol{w}}}_i + \tilde{\mathbf{p}}_{0i} & = 0 \end{cases} , \quad \forall \boldsymbol{w} \in \mathcal{W} \qquad (5.22)$$

where

$$\delta \boldsymbol{w}^T \tilde{\mathbf{p}}_{ij} = \Phi_b''' \bar{v}_j \dot{u}_j \delta w \quad \delta \boldsymbol{w}^T \tilde{\mathbf{p}}_{0i} = \Phi_b''' \hat{u} \bar{u}_i \delta w.$$

The imperfection coefficients $\tilde{\mu}_k$ are evaluated using the expression (5.20) instead of (3.20). Once the reduced non-linear system (5.19) is solved, the equilibrium path is traced according to (5.21).

The computational cost of the Koiter method with the proposed a-posteriori account of the geometrical imperfections remains of the order of that required by a standard linearised buckling analysis, that is dominated by the factorisation of the matrix $\mathbf{K}_0$. With respect to the standard approach, it is necessary to evaluate the new $m \times m$ correctives $\dot{\tilde{\boldsymbol{w}}}_{ij}$, and m correctives $\hat{\tilde{\boldsymbol{w}}}0_i$ by means of the linear problem in Eq.(5.22) and the corresponding third order strain energy variations in Eq.(5.20).

5.2 NUMERICAL RESULTS

In this section some benchmarks are considered in order to test the accuracy of the proposed a-posteriori account of geometrical imperfection. A comparison with the different approaches is made. In particular, the numerical results report:

- the solution of the full model non-linear equations, obtained using a standard path-following technique, denoted as Riks and considered the reference solution;
- the solution obtained through the Koiter method including the imperfection a-priori in the model by assuming $u_0 = \tilde{u}$ in subsection 3.3.1, which means that the reduced model is re-constructed for each imperfection while $\tilde{\mu}_k = 0$, denoted as K_0;
- the solution obtained through the Koiter method using the reduced model of the perfect structure, built once and for all, and taking into account the imperfection a-posteriori in the standard way recalled in 3.3.4, denoted as K_{lin};
- the solution obtained through the Koiter method using the reduced model of the perfect structure, built once and for all, and taking into account the imperfection a-posteriori according to the new proposal described in 5.1.2, denoted as K_{quad}.

The geometrical imperfection is given as a linear combination of the displacement shapes of the buckling modes and its maximum displacement components, denoted as $\tilde{u}_{max}$.

5.2.1 Simply supported plate

The first example regards a simply supported and uniformly compressed plate whose geometry, load and boundary conditions are reported in Fig.5.1. The imperfection shape is proportional to the first buckling mode reported in the same figure.

Fig.5.2 shows the equilibrium paths obtained with the different methods. In this case the proposed K_{quad} approach provides results very similar to reference Riks ones, even for a large imperfection magnitude, while the standard K_{lin} approach gives a result which is completely wrong. In this case the energy terms associated with $\mathring{w}$ and $\hat{w}$ are large also for small values of the imperfection amplitude due to the membrane hyperstaticity of the plate.

5.2.2 Cylindrical isotropic and laminated roofs

The structure, whose geometry and loads are pictured in Fig.5.3, is a semi-cylindrical roof loaded by a central force whose curved edges are free while the

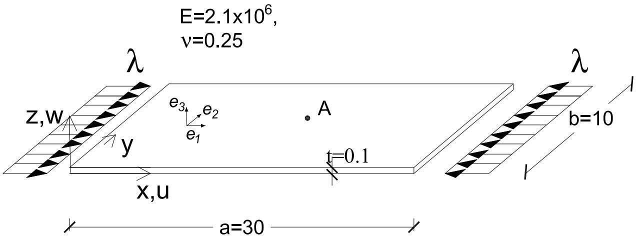

Figure 5.1: Simply supported plate: geometry, load and boundary conditions.

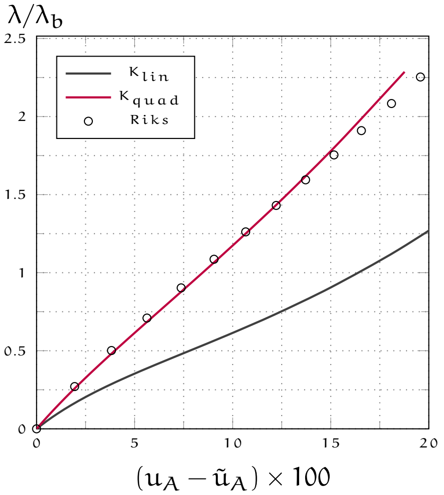

Figure 5.2: Simply supported plate: geometry and equilibrium paths for $\tilde{u}_{max} = t$

Figure 5.3: Cylindrical roof subjected to a central pinching force with material properties of the ply.

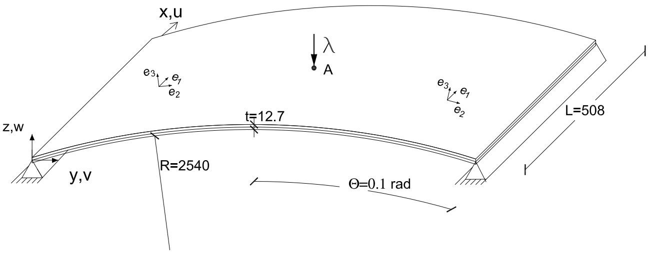

E_{11}	$E_{22} = E_{33}$	$\nu_{12} = \nu_{13}$	ν_{23}	$G_{12} = G_{13}$	G_{23}
3.3	1.1	0.25	0.25	0.66	0.44

straight ones are hinged. Three material configuration are studied: the first one in an isotropic material characterized by $E = 3.10275$ and Poisson ratio $\nu = 0.3$, the second and the third ones are laminated materials characterized by two different layups, $[0°/90°/0°]$ and $[90°/0°/90°]$ respectively with respect to the e_1-axis, whose properties are reported in Fig.5.3.

The imperfection shape is the displacement shape of the first buckling mode. In Figs.5.4, 5.5 and 5.6 the equilibrium paths and the limit loads for different values of the imperfection amplitude $\tilde{u}_{max}$ are reported. It is possible to observe how the proposed Koiter method with a-posteriori account K_{quad} furnishes accurate results for significant values of the imperfection amplitudes, very close to the a-priori account K_0 whose limit load always coincides with the Riks one. Since the pre-critical behaviour is non-linear even for the structure without imperfections, the standard a-posteriori account K_{lin} fails also for very small imperfection amplitudes.

Finally, it is worth noting from Fig.5.7 how the buckling mode corrected with $\mathring{w}_1$, according to Eq.(5.21), has a shape similar to those obtained considering the imperfection a-priori in the discrete model.

5.2.3 Compressed simply supported channel section

A simply supported channel section, whose geometry and material properties are reported in Fig.5.8 is now analysed with 2 different shapes of the imperfection depicted in Fig.5.13: the first one is the displacement shape of the first buckling mode (flexural), the second one corresponds to the displacement shape

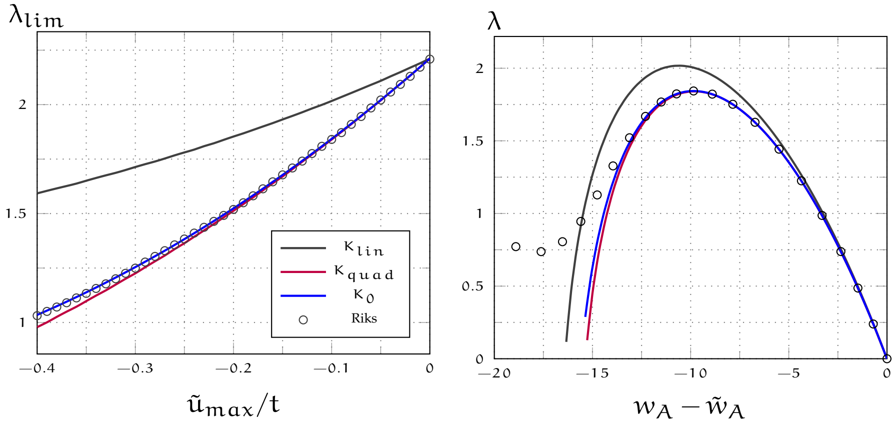

Figure 5.4: Cylindrical isotropic roof: limit load versus imperfection magnitude (left) and equilibrium paths for $\tilde{u}_{max} = 0.1t$ (right).

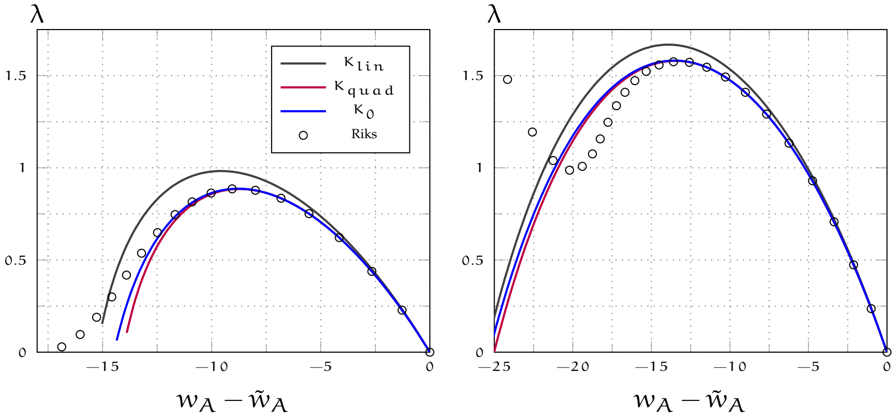

Figure 5.5: Cylindrical laminated roof: equilibrium paths for $u_{max} = 0.1t$ for layup [0/90/0] (left) and [90/0/90] (right).

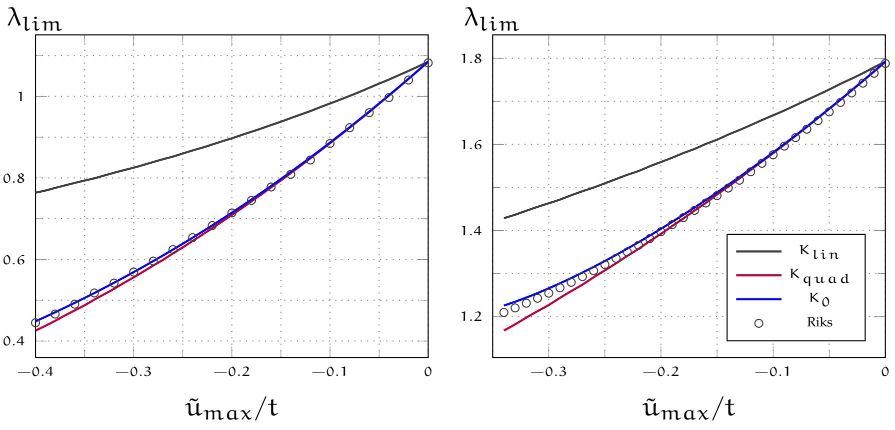

Figure 5.6: Cylindrical laminated roof: limit load vs imperfection magnitude for layup [0/90/0] (left) and [90/0/90] (right).

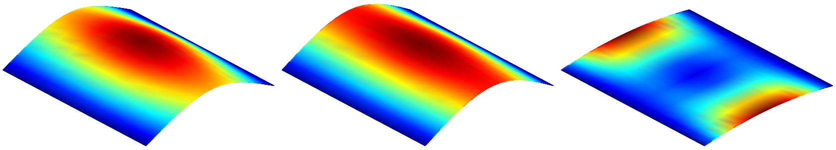

Isotropic: $\dot{v}_1$ $\dot{v}_1(K_0)$ $\dot{\tilde{w}}_1$

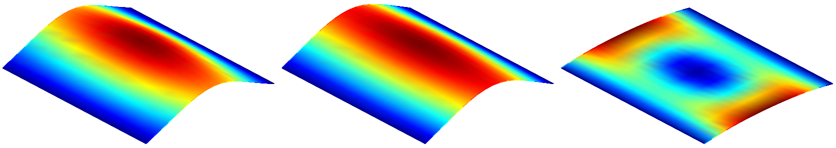

[0/90/0]: $\dot{v}_1$ $\dot{v}_1(K_0)$ $\dot{\tilde{w}}_1$

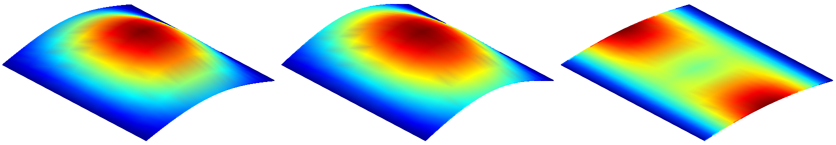

[90/0/90]: $\dot{v}_1$ $\dot{v}_1(K_0)$ $\dot{\tilde{w}}_1$

Figure 5.7: Cylindrical roof: bucking mode of the structure without imperfection, with $\tilde{u}_{max} = 0.2t$ and $\dot{\tilde{w}}_1$ for either isotropic, [0/90/0] and [90/0/90] cases.

of the 3rd buckling mode (local with 13 half-waves). The structure exhibits buckling mode interaction phenomena.

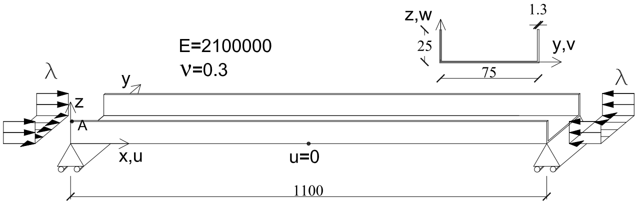

Figure 5.8: Compressed simply supported channel section with material properties.

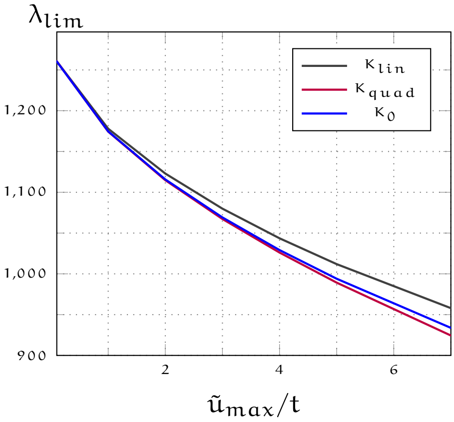

Figure 5.9: C-section: limit load versus imperfection magnitude for flexural imperfection.

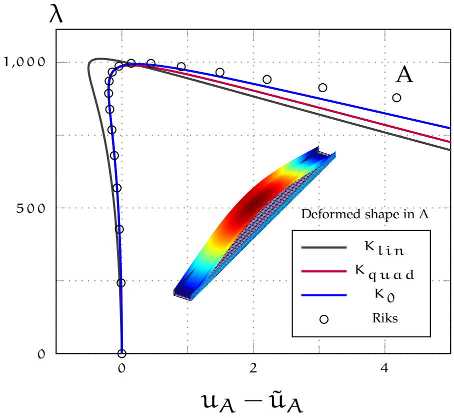

Figure 5.10: C-section: equilibrium paths for first buckling shape imperfection and $\tilde{u}_{max} = 5t$ (upwards).

In Fig.5.9 it is reported how the limit loads change with the amplitude of the first imperfection, while Fig.5.10 shows the equilibrium paths for $\tilde{u}_{max} = 5t$. In Fig.5.11 the buckling modes and correctives for K_0 and K_{quad} are reported. It can be observed how the buckling mode of the imperfect structure presents a shortening, while for the perfect structure presents a similar shape by summing its first buckling mode $\dot{v}_1$ and the corrective $\dot{\tilde{w}}_1$, according to Eq.(5.21). The good behaviour in the evaluation of the limit point of K_{quad} is evident while K_{lin} presents significant errors in the equilibrium path evaluation notwithstanding the fairly accurate value of the limit load.

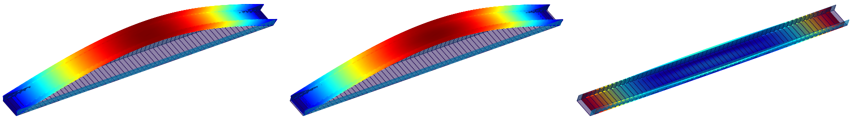

Figure 5.11: C-section: buckling mode of the structure without imperfection (left), with an imperfection in the direction of the first buckling mode of amplitude $\tilde{u}_{max} = 5t$ (centre) and the relative $\dot{\tilde{w}}_1$ (right, displacement factor 10).

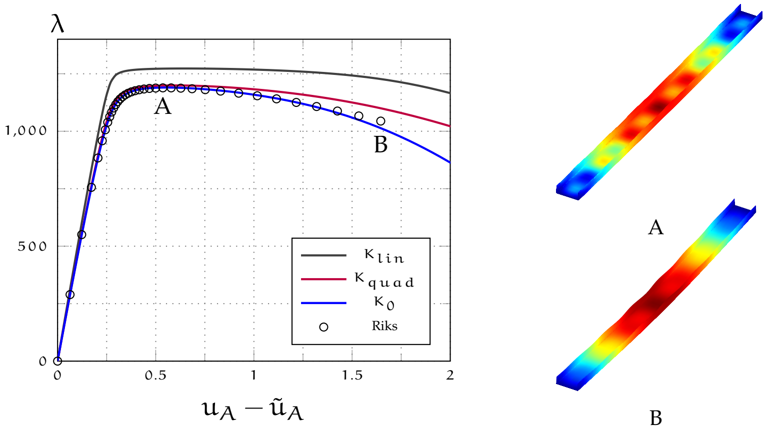

Figure 5.12: C-section: equilibrium paths for third buckling shape imperfection and $\tilde{u}_{max} = -0.5t$. 12 modes have been considered in asymptotic analysis.

In Fig.5.12 the equilibrium paths and the deformed shapes in two equilibrium points for the second imperfection, are presented. The corresponding mode shapes and how they change with the imperfection are reported in Fig.5.13. Also in this case the good behaviour of the proposal K_{quad}, compared to K_{lin}, is evident.

5.2.4 Cylinder

The test regards a compressed composite cylinder. The stacking sequence is $_{in}[0/0/19/-19/37/-37/45/-45/51/-51]_{out}$ with the rotation measured from the cylinder axis with respect to the outward normal. The height is 510 mm, the radius is $R = 250\,mm$, the thickness $t = 1.25\,mm$. The ply properties are $E_1 = 123.6$, $E_2 = E_3 = 8.7$, $\nu_{12} = 0.32$, $\nu_{13} = \nu_{23} = 0$, $G_{12} = G_{13} = G_{23} = 5.7$. The cylinder is labelled Z33 in the literature [52, 80] and has been used as a benchmark case of imperfection sensitivity. The cylinder is clamped on the top and bottom, excluding the axial displacement at the top edge where an uniform distributed load is applied. The displacement in the load direction of a node located at the top of the structure, and labelled w_A, has been chosen as control parameter in the equilibrium path representation. Some of the buckling modes of the perfect structure are plotted in Fig.5.14 while those of the imperfect one and the corresponding correctives $\dot{\tilde{w}}_k$ for a geometrical imperfection in the direction of $\dot{v}_1$ are reported, respectively in Fig.5.16 and Fig.5.17. The equilibrium path and the deformed shape at the limit point, for $\tilde{u}_{max} = 0.2t$ are plotted in Fig.5.15 while the limit load values for all the methods are presented in Tab.5.1. Finally in Fig.5.18 there are the equilibrium paths for a different imperfection shape and $\tilde{u}_{max} = 0.2t$. Also in this case the limit loads evaluated with the different formulations are reported in Tab.5.1. The K_{quad} approach always exhibits greater accuracy than K_{lin} for both the imperfection shapes.

Table 5.1: Cylinder: limit load to imperfection direction for several methods and imperfection amplitudes $\tilde{u}_{max} = 0.2t$.

imp. direction	K_{lin}	K_{quad}	K_0	Riks
$\dot{\mathbf{v}}_1$	0.0831	0.0732	0.0759	0.0769
$\dot{\mathbf{v}}_1 + \dot{\mathbf{v}}_2 + \dot{\mathbf{v}}_3$	0.0929	0.0868	0.0825	0.0826

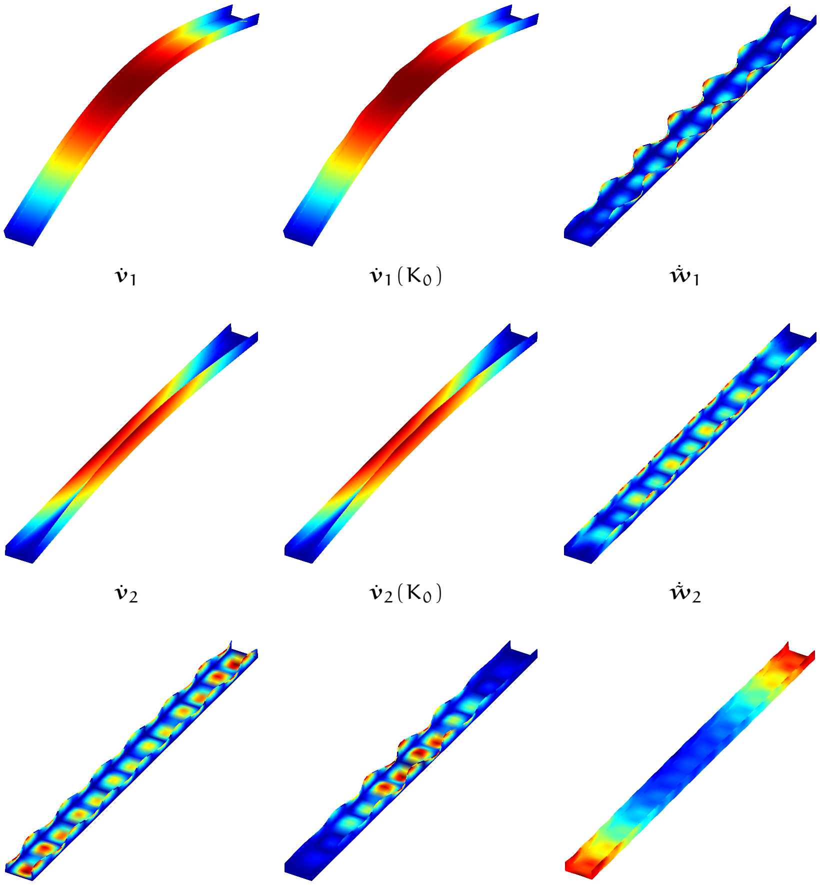

$\dot{\boldsymbol{v}}_1$ $\dot{\boldsymbol{v}}_1(K_0)$ $\dot{\tilde{\boldsymbol{w}}}_1$

$\dot{\boldsymbol{v}}_2$ $\dot{\boldsymbol{v}}_2(K_0)$ $\dot{\tilde{\boldsymbol{w}}}_2$

$\dot{\boldsymbol{v}}_3$ $\dot{\boldsymbol{v}}_3(K_0)$ $\dot{\tilde{\boldsymbol{w}}}_3$

Figure 5.13: C-section: first, second and third buckling modes of the structure without imperfection, with $\tilde{u}_{max} = 0.5t$ in the direction of the third buckling mode and $\dot{\tilde{w}}$ (displacement factor 10).

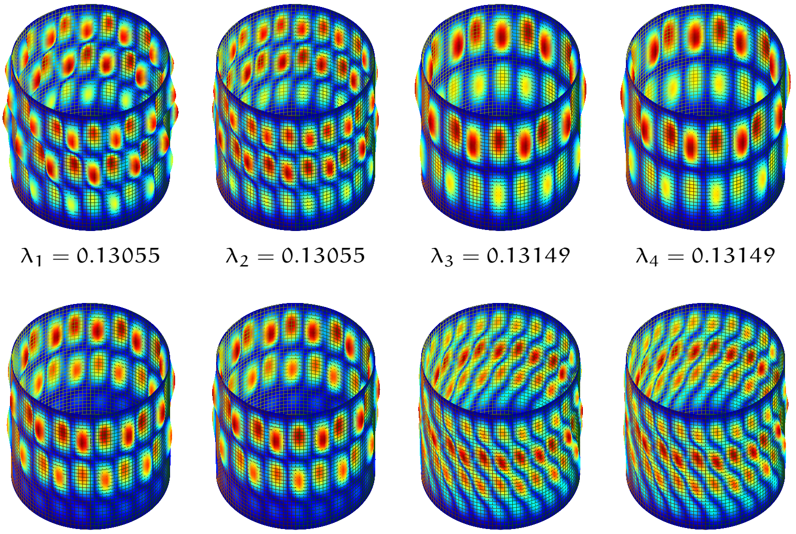

$\lambda_1 = 0.13055$ $\lambda_2 = 0.13055$ $\lambda_3 = 0.13149$ $\lambda_4 = 0.13149$

$\lambda_5 = 0.13165$ $\lambda_6 = 0.13165$ $\lambda_7 = 0.13197$ $\lambda_8 = 0.13197$

Figure 5.14: Cylinder Z33: first 8 buckling modes of the structure without imperfection.

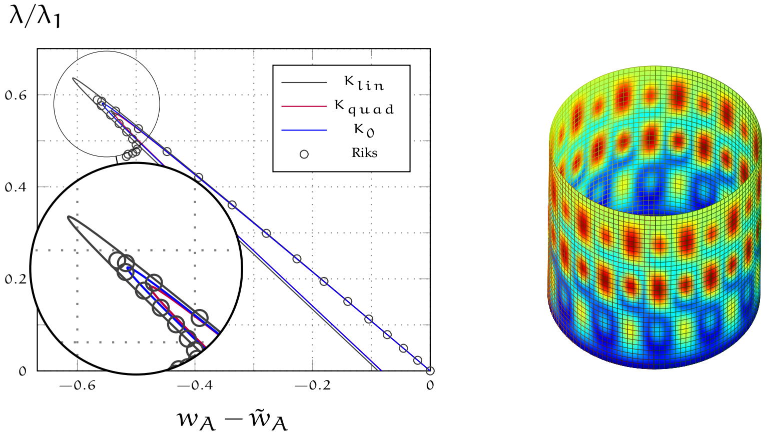

Figure 5.15: Cylinder Z33: equilibrium paths (left) and deformed shape at limit load (right) for first buckling shape imperfection and $\tilde{u}_{max} = 0.2t$. 8 modes have been considered in asymptotic analysis.

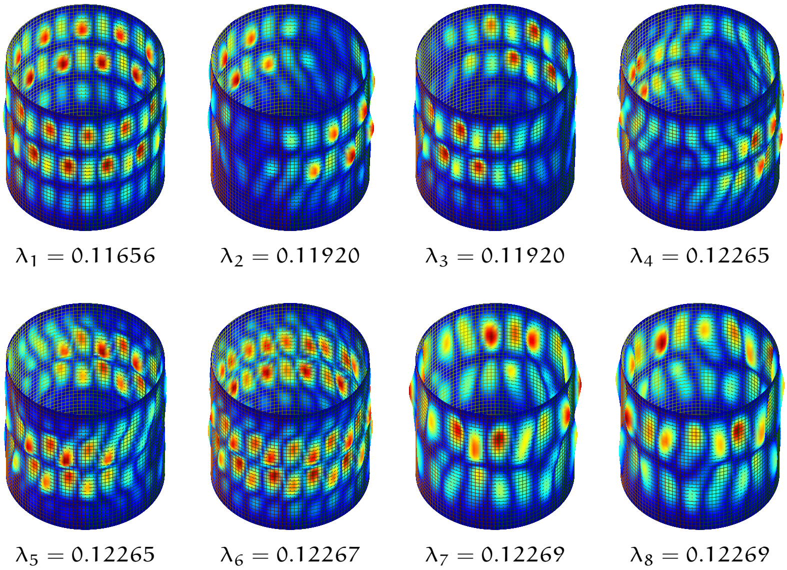

$\lambda_1 = 0.11656$ $\lambda_2 = 0.11920$ $\lambda_3 = 0.11920$ $\lambda_4 = 0.12265$

$\lambda_5 = 0.12265$ $\lambda_6 = 0.12267$ $\lambda_7 = 0.12269$ $\lambda_8 = 0.12269$

Figure 5.16: Cylinder Z33: $\dot{\mathbf{u}}$ in the case of imperfection along the first buckling mode and maximum amplitude $\tilde{u}_{max} = 0.2t$.

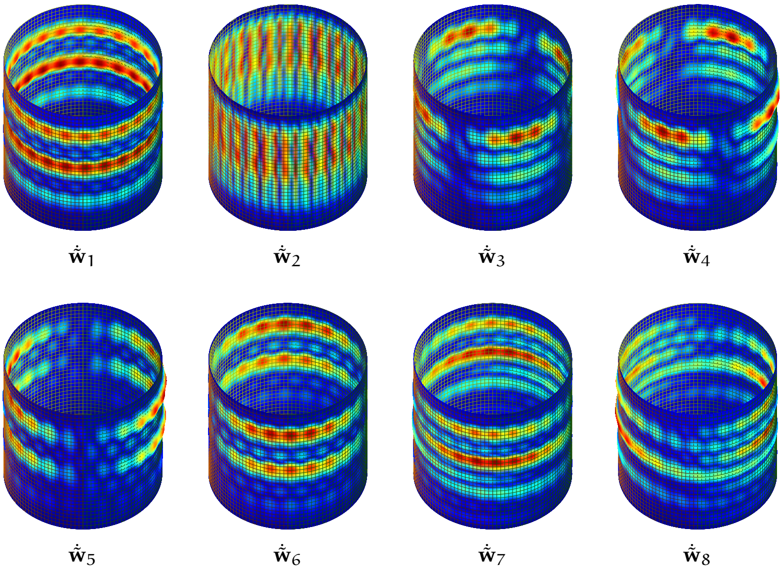

$\dot{\mathbf{w}}_1$ $\dot{\mathbf{w}}_2$ $\dot{\mathbf{w}}_3$ $\dot{\mathbf{w}}_4$

$\dot{\mathbf{w}}_5$ $\dot{\mathbf{w}}_6$ $\dot{\mathbf{w}}_7$ $\dot{\mathbf{w}}_8$

Figure 5.17: Cylinder Z33: $\dot{\mathbf{w}}$ in the case of imperfection along the first buckling mode and maximum amplitude $\tilde{u}_{max} = 0.2t$. The displacement scale is ten times bigger than the one used in the buckling mode representation.

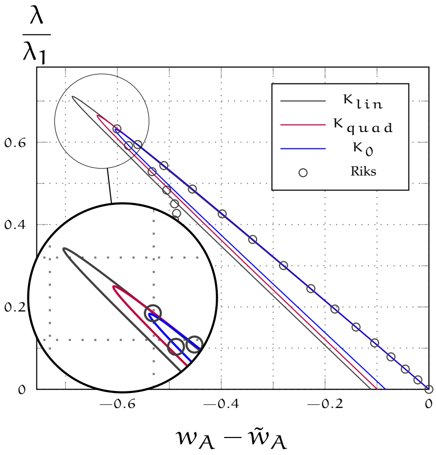

Figure 5.18: Cylinder Z33: equilibrium paths for imperfection: $\tilde{\mathbf{u}} = \dot{\mathbf{v}}_1 + \dot{\mathbf{v}}_2 + \dot{\mathbf{v}}_3$ and $\tilde{u}_{max} = 0.2t$. 8 modes have been considered in asymptotic analysis.

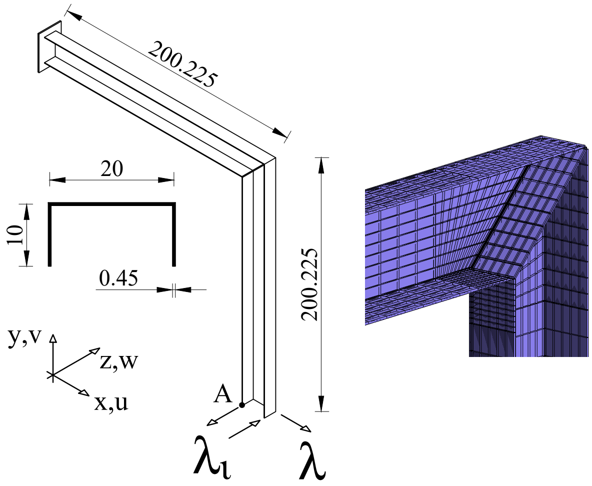

Figure 5.19: Frame: geometry and mesh grid detail.

5.2.5 Frame

The last test regards the frame reported in Fig.5.19. The first 5 buckling modes of the perfect structure are reported in Fig.5.20, while the limit load versus imperfection amplitude curve for a geometrical imperfection with the shape of the second buckling mode and the equilibrium path for $\tilde{u}_{max} = 0.4t$ are reported in Fig.5.21. In the same figure, the equilibrium path of the structure without imperfections is presented, in order to point out the strong imperfection sensitivity of the frame and the modal interaction phenomenon. Even in this last case the proposal K_{quad} provides very accurate results with a limit point which coincides with the a-priori account K_0 and Riks solution, while inaccuracies occur for K_{lin}.

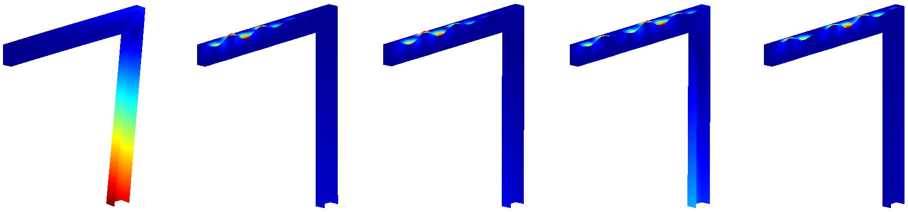

$\lambda_1 = 0.570.$ $\lambda_2 = 0.722.$ $\lambda_3 = 0.726.$ $\lambda_4 = 0.769.$ $\lambda_5 = 0.774.$

Figure 5.20: Frame: First 5 buckling modes of the structure without geometrical imperfections.

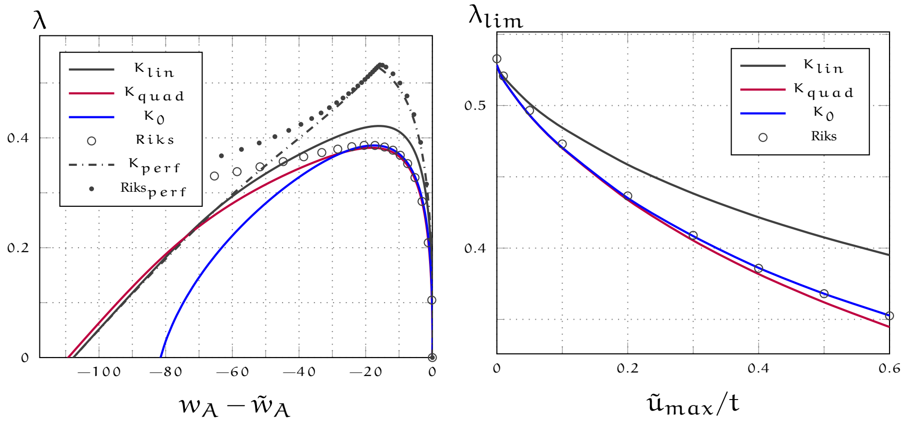

Figure 5.21: Frame: equilibrium paths for geometrical imperfection along the second buckling mode and $\tilde{u}_{max} = 0.4t$ (left) and magnitude imperfection sensitivity (right).

6 OPTIMISATION STRATEGIES

The optimisation of composite structures is a classical research topic that attracts interest for the significant impact on industry it has [90]. In fact, multilayered composite panels offer the technological possibility of being accurate tailored to obtain highly optimised components with the desired structural behaviour. In the recent years one could observe the spread of new technologies that are able to outperform classical composites. Fibre orientations are not only limited to conventional angles, such as ±45°, ±30°, 90°, but a wider set of orientations can be accurately manufactured. Moreover, variable stiffness laminates play a key role among new technologies. They are capable of changing the stiffness pointwise over a structure, such that a great tailoring freedom can be achieved. One of the most promising variable stiffness technology is represented by VAT, namely composites made of fibre that draw curvilinear paths [91]. VAT laminates have proven to be able to redistribute stresses thereby improving structural performance in the linear-elastic range and increasing the buckling load [92–98]. However, less well known is the capability of VAT of performing well also in the postbuckling regime [7, 86, 99]. For instance, recently, White and Weaver showed [25] that the well-known imperfection sensitivity of a cylindrical thin structure under compression loading can be eliminated by tailoring the fibre paths across the surface of cylindrical shells.

Despite the advantages on tailoring capability, VAT laminates require more variables to obtain an optimal design than straight-fibre composites. The strategies present in the literature for describing the VAT over the structural domain can be framed into three groups, namely fibre path parameterisation, discrete fibre representation and direct stiffness modelling [100]. The fibre path parameterisation is based on a pre-defined fibre path controlled by few variables for each layer. In this way, the number of optimisation variables is limited. As such, the main issue resides in the fact that the space in which one looks for the solution is limited and potential optimal configurations are a-priori excluded. Additionally, the resulting optimisation problem is highly non-linear and non-convex and global stochastic optimisers are usually employed. The discrete fibre representation is based on the description of the fibre orientations on a grid of points over the domain of each layer. In this way, the entire optimisation space is encompassed, but the resulting optimisation problem is extremely complex to be solved due to the high nonlinearity and non-convexity and the high number of variables. Conversely, the direct stiffness modelling represents an interesting alternative. It consists of designing directly the homogenised stiffness matrix, regardless of the stacking sequence and the number of plies. To this purpose, the main methods make use of polar decomposition [101] or lamination parameters [102]. In particular, the use of the latter turns out too be particularly convenient for laminates made of many layups because the stiffness matrix of the structure can be described by a linear function of 12 lamination parameters. This aspect entails the reduction of the nonlinearity of the optimisation problem because the nonlinear relationship between fibre orientations and homogenised stiffness matrix is eliminated. The postbuckling optimisation problem is still non-convex, though its solution is simplified, such that gradient based optimisers can be successfully employed. Lamination parameters have already been used by Raju et al.[7] for optimising the postbuckling response of simple geometries.

The optimisation of full-scale structures accounting for their postbuckling behaviour is, however, not so common, requiring time-consuming procedures based on finite element simulations. In this chapter we propose the numerical solution previously described as a valid alternative to be used within an effective optimisation process. It possesses, in fact, many desirable features that ensure generality, accuracy and efficiency that are provided by the solid-shell IGA formulation and the relative implementation of Koiter's method using the MIP technique and the improved accuracy for including the effect of geometrical imperfections.

Koiter's method gives us the possibility of evaluating a wide range of structures, being characterised by complex geometry and entangled postbuckling behaviours. Additionally, it makes it possible to control the imperfection sensitivity during the optimisation process by employing the strategy previously presented. In this way naive optimised solutions [89] are excluded because, for each call of the objective function, an imperfection sensitivity analysis is executed [103]. Two postbuckling optimisation strategies are proposed, sharing the same numerical tool for evaluating the objective function. The first one is based on the use of stochastic simulations to obtain a good estimate of a globally optimal design. When VAT structures are optimised, a fibre path parameterisation is used to reduce the number of optimisation variables [103, 104]. The second strategy is based on direct stiffness modelling using lamination parameters and turns out to be particularly convenient if one wants to optimise structures made of many layers and has the property of smoothing out the objective function and therefore gradient-based optimisers can be successfully employed.

6.1 POSTBUCKLING OPTIMISATION

There is not a unique choice for the objective function when optimising the postbuckling behaviour of thin-walled structures. When dealing with stable postbuckling behaviour, some authors have considered the minimisation of the in-plane or the out-of-plane displacement at a design load within the optimisation of VAT plates [7], others have maximised the load required for reaching a given displacement at a control point [103], while in other works the postbuckling slope and curvature have been maximised [105, 106]. Conversely, if the structure exhibits an unstable behaviour, maximising the limit point seems to be the natural choice [103]. As highlighted by Raju et al. [7], the fibre orientations that minimise the out-of-plane deformation can opposite those that minimise in-plane deformation and, generally, the way of controlling the postbuckling represents a design choice. Generally, if we consider a certain property $\mathcal{P}[\mathbf{h}]$ of the structural behaviour, its minimisation is expressed as

$$\begin{aligned} &\underset{\mathbf{h}}{\text{minimise}} && \mathcal{P}[\mathbf{h}] \\ &\text{subject to} && \mathcal{D}[\mathbf{h}] \leqslant 0 \end{aligned} \tag{6.1}$$

where $\mathcal{D}[\mathbf{h}]$ defines the boundary of the feasible domain. We indicate with $\mathbf{h}$ the vector collecting the optimisation variables that control the composite material.

The evaluation of the objective function $\mathcal{P}[\mathbf{h}]$ is implicitly conducted by solving the reduced system of equilibrium equations built by Koiter's method. After the equilibrium path is drawn, we can extract the property $\mathcal{P}[\mathbf{h}]$ that represents a certain displacement, a stress or a load level. Additionally, every time one asks for the objective function evaluation, an imperfection sensitivity analysis is conducted to provide the worst-case imperfections that gives the worst-case equilibrium path. The procedure is described in the following section.

6.1.1 Imperfection sensitivity analysis

Let us consider an unknown geometrical imperfection $\tilde{\mathbf{d}}$ evaluated, as linear combination of the displacement part of m buckling modes

$$\tilde{\mathbf{d}}[\tilde{\xi}_i] = \sum_{i=1}^{m} \tilde{\xi}_i \mathbf{v}_i$$

where the coefficients $\tilde{\xi}_i$ set the imperfection amplitude equal to a fixed value $\tilde{u}_{max}$, namely

$$\left|\tilde{\mathbf{d}}[\tilde{\xi}_1, \dots, \tilde{\xi}_m]\right|_\infty = \tilde{d}_{max}. \tag{6.2}$$

The corresponding discrete vector containing also the stresses is $\tilde{\mathbf{u}}$. The reduced equilibrium equation system of a structure with the geometrical imperfection $\tilde{\mathbf{d}}$ is expressed by Eq.(5.19). If we assume the coefficients $\tilde{\xi}_i$ to be unknowns, the equilibrium path of the structure depends from them. Consequently, we have the objective function in Eq. (6.1) as a function of the imperfection, namely we have

$$\mathcal{P} = \mathcal{P}[\mathbf{h}, \tilde{\xi}_1, \ldots, \tilde{\xi}_m].$$

At this point, we can define the worst-case imperfection for a given $\mathbf{h}$ as the set of imperfection coefficient $\tilde{\xi}_i$ that give the worst value of $\mathcal{P}$, namely we need to solve

$$\begin{aligned} &\underset{\mathbf{h}}{\text{maximise}} && \mathcal{P}[\mathbf{h}, \tilde{\xi}_1, \ldots, \tilde{\xi}_m] \\ &\text{subject to} && \left|\tilde{\mathbf{d}}[\tilde{\xi}_1, \ldots, \tilde{\xi}_m]\right|_\infty = \tilde{d}_{max} \end{aligned} \tag{6.3}$$

A remarkable advantage for analysing a slender structure with Koiter's method resides in the possibility of accounting for the effect of the imperfection a-posteriori thereby making the solution of Eq. (6.3) efficient. To this end, we propose the use of a stochastic iterative procedure based on Monte Carlo simulation.

The algorithm can be summarised as follows.

1. Generate a sample of ns imperfection coefficients $\tilde{\xi}_i^j$, $i = 1, \ldots m$, $j = 1, \ldots, ns$ that satisfy Eq. (6.2).
2. Evaluate $\mathcal{P}[\mathbf{h}, \tilde{\xi}_1^j, \ldots, \tilde{\xi}_m^j]$ for every $j = 1 \ldots ns$.
3. Build a frequency distribution for $\mathcal{P}$.
4. Fit the frequency distribution using a probability density function. Due to the nature of the objective function, usually a good fit is reached by a type 1 extreme value distribution, also known as Gumbel max distribution
$$f(\lambda_c) = \sigma^{-1} \exp\left(\frac{\mu - \lambda_c}{\sigma}\right) \exp\left(-\exp\left(\frac{\mu - \lambda_c}{\sigma}\right)\right) \tag{6.4}$$
where μ and σ are the location parameter and scale parameter, respectively.
5. Check the convergence criteria: the maximum number of imperfections is exceeded or the variation of μ and σ stays under a tolerance value ϵ_π between two consecutive steps three times in a row
$$\frac{\mu_k - \mu_h}{\mu_k} \leqslant \epsilon_\pi \quad \forall h = k-1, \cdots, k-3$$

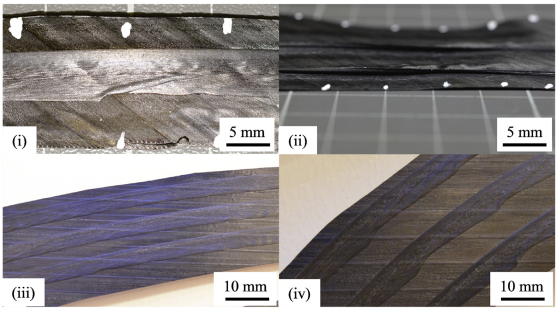

Figure 6.1: Width and thickness variation due to fibre steering, from Clancy et al. [107].

where h denotes the current step.

6. If convergence is reached, a solution has been found, otherwise go to step 1.

6.1.2 Manufacturing constraints

The optimisation of VAT laminates should be able to ensure that the designed fibre path is actually manufacturable. In fact, many defects can be observed due to fibre steering. The main consequence is a variation in width and thickness of the fibre tow increasing with the steering curvature. This is due to fibre wrinkling, fibre fibre buckling and pull-up, as can be noticed in Fig. 6.1, from the Clancy et al. [107]. Additionally, to small steering radii are related phenomena of gap and overlap of the fibre tow, with the consequence of an undesired-variable overall thickness. They can be avoided if parallel fibre paths are realised, with a variation of the curvature among parallel tows.

Consequently, including manufacturing constrains in VAT optimisation process is of great importance [108–110]. In the following only a constraint on the steering radius is included, because it represents the most significant parameter, even if many other manufacturing constraints could be considered.

Being $\vartheta[\xi, \eta]$ the fibre orientation within a single layer, the tangent at the fibre path is

$$\mathbf{t} = [\cos\vartheta[x, y],\, \sin\vartheta[x, y]]^{T}$$

The curvature of a parametric curve is the derivative of ϑ in the tangential direction,namely

$$k(x,y) = \left[\frac{\partial(\vartheta(x,y))}{\partial(x)}, \quad \frac{\partial(\vartheta(x,y))}{\partial(y)}\right]^T \cdot \mathbf{t}. \tag{6.5}$$

Therefore, a constraint on the steering curvature can be included in the optimisation problem in Eq.6.1 as

$$\mathcal{D} = |k - k_{lim}| \leqslant 0, \tag{6.6}$$

where k_{lim} is the maximum allowable steering curvature.

6.2 STOCHASTIC OPTIMISATION

Stochastic optimisation strategies are commonly used in structural optimisation [111, 112]. Their evolution towards the optimal solution is not fully deterministic, but includes the use of random-generated values. Generally speaking, the methods start from an initial random sample and at each iteration a new, improved, population is constructed by applying some stochastic criteria, until convergence is reached. The methods available in literature use different rules to evolve towards the optimum value, and many of them are inspired by natural phenomenon. Therefore, the literature today includes genetic [111], firefly [113], pray-predator [114], ant-colony [115], particle swarm [116] algorithms and many others. The reason of their success reside in the fact that they are able to provide an estimate of the global optimum of non-smooth objective functions in presence of many local optima and high non-convexity. The price for this freedom is a slow convergence rate, and therefore they require an efficient objective function to be effective. Thanks to Koiter's method previously presented, we can efficiently use such algorithms to look for the optimal stacking sequence of composites structures.

However, the number of variables that is possible to chose is limited to a few tens. Therefore, when VAT laminates are optimised, a fibre-path parameterisation is adopted. A commonly-used choice is represented by the linear variation according to Gürdal and Olmedo [92]. In such a case, the fibre orientation is given by

$$\vartheta[\eta] = \varphi + \left(\frac{T_1 - T_0}{a}\right)|\eta| + T_0 \tag{6.7}$$

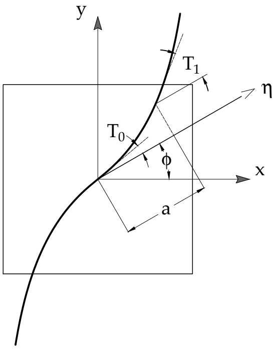

Figure 6.2: Fibre path parameterisation according the linear variation proposed by Gürdal and Olmedo [92].

where η is an abscissa measured along a direction rotated of φ according to Fig. 6.2, T_0 and T_1 are respectively the fibre orientations at the point where $\eta = 0$ and the point where $\eta = a$, measured with respect to φ. Despite its simplicity, the linear variation has many advantages. In fact, the VAT laminate can be described by few variables, only three per layup, and technological constraints on the fibre path can be readily included to ensure manufacturability [107, 109, 110].

The optimisation variables, generically identified with $\mathbf{t}$ in Eq. (6.3), are the fibre orientations of the fibre path parameterisation for each layer, collected in the vector $\boldsymbol{\vartheta}$.

In the following, we present some optimisation methods. The first one is simply a uniform scanning of the optimisation domain. The second one is an evolutionary random-search [117] based on Monte Carlo simulation and lastly the main steps of the genetic algorithm are given.

6.2.1 Uniform scanning

The approach is based on the simple idea of uniformly scanning the space of the N possible layups. In this way, at the end of the process, the objective function trend with the optimisation variables is completely known and the actual optimal solution can be easily identified. Even if the number of analyses can be significantly high, the efficiency of Koiter's method makes them possible in a reasonable computational time when the space is defined by a few parameters. It is evident, indeed, that the number of analyses increases exponentially with the dimension of the sought parameter space.

The approach consists of two stages. During the first one the space is uniformly scanned and, for each lamination, an imperfection sensitivity analysis is performed to detect the collapse load. The second stage is aimed at checking the best solutions found in stage 1 by repeating the imperfection sensitivity analysis with more restrictive tolerances on the μ and σ parameters, as defined in 6.1.1, and including their effect using the K_{quad} approach which proves to be more accurate. Finally, the structure with the best layup subjected to the worst imperfection shape is analysed by means of a path-following Riks analysis using the full FE model.

6.2.2 Monte Carlo random search

The main problem of uniformly scanning the domain of the optimisation parameters is that the number of analyses can increase enormously and, although the Monte Carlo imperfection sensitivity analysis with Koiter's method is efficient, it can prevent the solution of the problem. The second approach proposed overcomes this problem by using a Monte Carlo Algorithm (MCA) to detect the best stacking sequence. The random search simulation MCA is based on two stages [103]. During the first , it generates a random population of N_1 layups and the objective function is evaluated for each of them. The best $n = n_1$ solutions, identified as being an elite ($\mathbf{x}_{el}$), are selected and represent the starting points of the second stage. This is constructed by a sequence of steps (zoom steps) that try to improve the elite population. For each elite value $\mathbf{x}_{el}$, the objective function is evaluated N_2 times at random points defined as

$$\vartheta(j) = \mathbf{x}_{el}(j) + rnd(-R, R)$$

where $j = 1 \dots n$ denotes the elite value and rnd is a generator of pseudo random integer values between $-R$ and R. The radius R assumes the value R_1 during the first zoom step and R_2 during the following ones.

At the end of a zoom step, $n = n_2$ best solutions are selected and represent the elite population of the next step. If convergence is reached the algorithm stops, otherwise a next zoom step is performed.

The algorithm is summarised in the flowchart shown in Fig.6.3.

6.2.3 Genetic Algorithm (GA)

We can couple the advantages given by Koiter's asymptotic analysis with those given by a GA. It is a meta-heuristic optimisation method that looks for the best solution following analogue concepts to those of the evolution of the species.

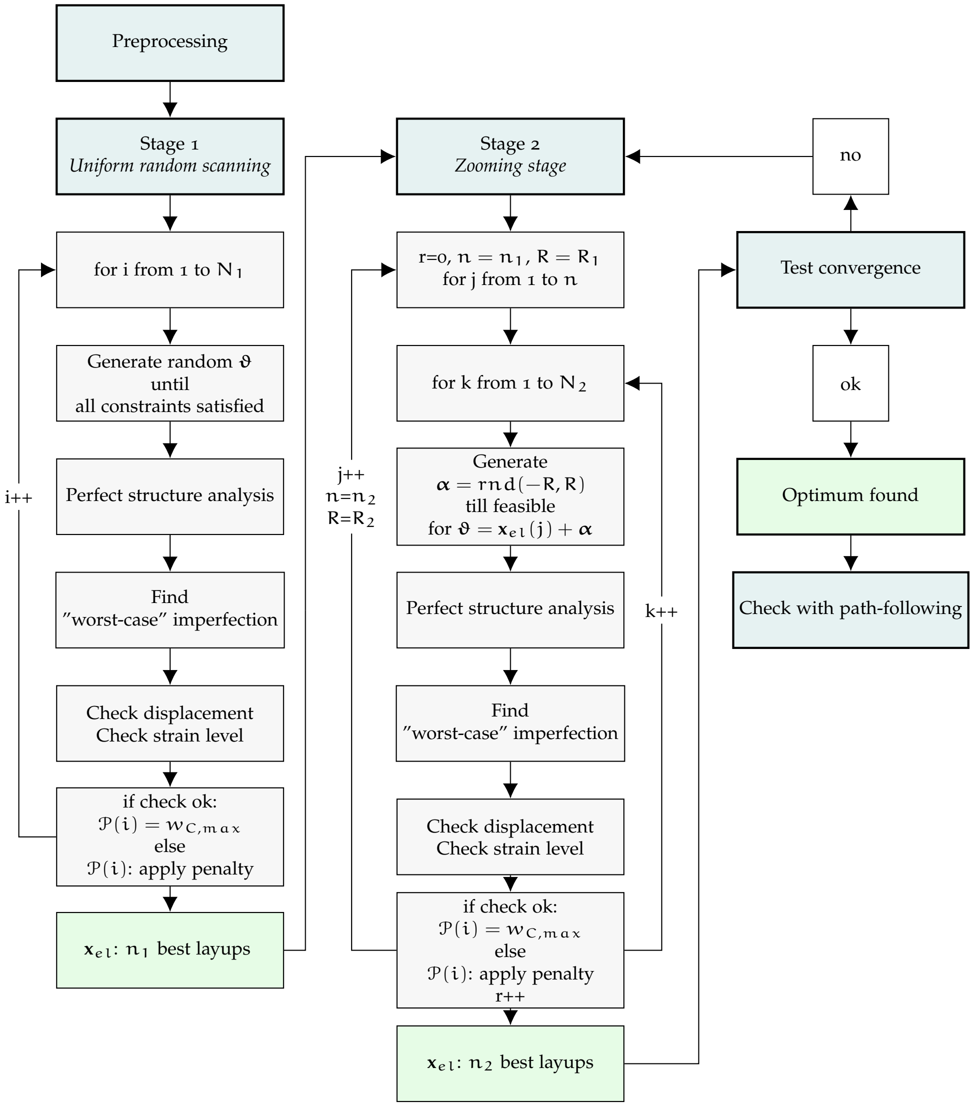

Figure 6.3: Minimisation of $\mathcal{P}[\vartheta]$ using MCA.

Each variable (fibre orientation) is defined by an array of genes. The algorithm can be summarised in the following steps

1. Generate an initial population.
2. Evaluate the objective function using the Koiter algorithm.
3. Select the best individuals (elite).
4. Create the new generation through genetic operations (crossover and mutation).
5. Repeat steps fom 2 to 4 until convergence is reached.

The genetic operations are the criteria that the method uses to improve the population. Crossover swaps some genes between parent individuals. Mutation changes some genes of parent individuals with some random values. In this work, GA [118] with inequality constraints treated as in [119] is employed.

6.3 LAMINATION PARAMETERS

Laminations parameters are effectively used in optimisation problems. In such a case, the optimisation problem is divided into two stages [120]. In the first one, the optimal distribution of lamination parameters is obtained. This is done by employing gradient-based optimisers, because, when written in function of lamination parameters, the optimisation space is smoother than when the fibre orientations are directly optimised. In the second stage a real stacking sequence and fibre orientations are retrieved by the optimal distribution of lamination parameters. The second stage represents a post-processing part of the optimisation process and within this stage manufacturing requirements can be included [109]. In such a way, stage one is a relatively smooth optimisation problem, independent from the number of layers and represents the time consuming part because it involves IGA-Koiter analyses. Conversely, stage two is highly non-linear and non-convex, but the objective function evaluation is extremely rapid.

AN INTEGRATED FRAMEWORK To describe lamination parameters and fibre orientations over the structural domain, use is made of the same NURBS model employed by the isogeometric solid-shell model proposed in chapter 4. In this way, the geometrical description adopted by the CAD model is used to interpolate the unknown fields of the structural model and the variables of optimisation problem, thereby leading to the formulation of an integrated framework for the optimal design of shell structures undergoing buckling. Different levels of h and p refinements [74] can be adopted to account for the different nature of the fields. Therefore, the time spent during the overall design process can be reduced.

Afterwards, it is shown first how the expression of the constitutive matrix modifies when written in terms of lamination parameters. Then, stage one and stage two are described in detail.

6.3.1 Constitutive matrix

The stiffness matrix in a given point ζ_0 of the mid-surface is expressed as

$$\mathbf{C} = \begin{bmatrix} \mathbf{A} & 0 & \mathbf{B} & 0 \\ 0 & Q_{33} & 0 & 0 \\ \mathbf{B} & 0 & \mathbf{D} & 0 \\ 0 & 0 & 0 & \mathbf{A}_s \end{bmatrix} \tag{6.8}$$

where the plane-stress condition is enforced to avoid thickness-locking phenomena [11]. The matrices $\mathbf{A}$, $\mathbf{B}$, $\mathbf{D}$ and $\mathbf{A}_s$ are evaluated in terms of lamination parameters and material invariants

$$\begin{aligned} \mathbf{A} &= \mathbf{\Gamma}_0 + \mathbf{\Gamma}_1\psi_1^A + \mathbf{\Gamma}_2\psi_2^A + \mathbf{\Gamma}_3\psi_3^A + \mathbf{\Gamma}_4\psi_4^A \\ \mathbf{B} &= \frac{1}{2}\left(\mathbf{\Gamma}_1\psi_1^B + \mathbf{\Gamma}_2\psi_2^B + \mathbf{\Gamma}_3\psi_3^B + \mathbf{\Gamma}_4\psi_4^B\right), \\ \mathbf{D} &= \frac{1}{3}\left(\mathbf{\Gamma}_0 + \mathbf{\Gamma}_1\psi_1^D + \mathbf{\Gamma}_2\psi_2^D + \mathbf{\Gamma}_3\psi_3^D + \mathbf{\Gamma}_4\psi_4^D\right) \\ \mathbf{A}_s &= \mathbf{\Gamma}_0^s + \mathbf{\Gamma}_1\psi_1^A + \mathbf{\Gamma}_2^s\psi_2^A. \end{aligned} \tag{6.9}$$

Only lamination parameters depend from the point ζ_0, are defined in the domain $[-1, 1]$ and can be evaluated as

$$\begin{aligned} \psi_i^A =& \int_{-1}^{1} f_i d\zeta_3 \\ \psi_i^B =& 2\int_{-1}^{1} \zeta_3 f_i d\zeta_3 \\ \psi_i^D =& 3\int_{-1}^{1} \zeta_3^2 f_i d\zeta_3, \quad i = 1, \cdots, 4 \end{aligned} \tag{6.10}$$

where f_i is the component of the vector $\mathbf{f} = [\cos(2\vartheta), \sin(2\vartheta), \cos(4\vartheta), \sin(4\vartheta)]$. Matrices $\boldsymbol{\Gamma}_i$ and $\boldsymbol{\Gamma}_i^s$ assume the values

$$\begin{aligned}
&\boldsymbol{\Gamma}_0 = \begin{bmatrix} U_1 & U_4 & 0 \\ U_4 & U_1 & 0 \\ 0 & 0 & U_5 \end{bmatrix}, \quad \boldsymbol{\Gamma}_1 = \begin{bmatrix} U_2 & 0 & 0 \\ 0 & -U_2 & 0 \\ 0 & 0 & 0 \end{bmatrix}, \\
&\boldsymbol{\Gamma}_2 = \begin{bmatrix} 0 & 0 & U_2/2 \\ 0 & 0 & U_2/2 \\ U_2/2 & U_2/2 & 0 \end{bmatrix}, \quad \boldsymbol{\Gamma}_3 = \begin{bmatrix} U_3 & -U_3 & 0 \\ -U_3 & U_3 & 0 \\ 0 & 0 & -U_3 \end{bmatrix}, \\
&\boldsymbol{\Gamma}_4 = \begin{bmatrix} 0 & 0 & U_3 \\ 0 & 0 & -U_3 \\ U_3 & -U_3 & 0 \end{bmatrix},
\end{aligned} \tag{6.11}$$

$$\boldsymbol{\Gamma}_0^s = \begin{bmatrix} U_5 & 0 \\ 0 & U_5 \end{bmatrix}, \quad \boldsymbol{\Gamma}_1^s = \begin{bmatrix} U_6 & 0 \\ 0 & -U_6 \end{bmatrix}, \quad \boldsymbol{\Gamma}_2^s = \begin{bmatrix} 0 & -U_6 \\ -U_6 & 0 \end{bmatrix}, \tag{6.12}$$

in which the material invariants are defined as

$$\begin{aligned}
U_1 &= (3Q_{11} + 3Q_{22} + 2Q_{12} + 4Q_{66})/8, \\
U_2 &= (Q_{11} - Q_{22})/2, \\
U_3 &= (Q_{11} + Q_{22} - 2Q_{12} - 4Q_{66})/8 \\
U_4 &= (Q_{11} + Q_{22} + 6Q_{12} - 4Q_{66})/8, \\
U_5 &= (Q_{44} + Q_{55})/2, \\
U_6 &= (Q_{44} - Q_{55})/2.
\end{aligned} \tag{6.13}$$

The optimisation problem is based on searching for the stiffness distribution that realises the minimisation of a certain property of the equilibrium path obtained by solving Eq. (3.18). This is pursued, as already suggested by [7], by dividing the process into two stages. In the first one, the optimal distribution of lamination parameters is obtained. Then, in the second one, the actual variable stiffness material is retrieved. In particular, in this work the stiffness variations is obtained using the VAT technology, namely changing the fibre orientations over the domain. The two stages are described in the following.

6.3.2 Stage one: optimal distribution of lamination parameters

We collect all the lamination parameters of the structure at control points in the vector $\boldsymbol{\psi}_g$. By means of this vector, we can obtain the lamination parameters in a point of the domain ζ_0 using the NURBS interpolation expressed by Eq.(2.24) in terms of isogeometric elemental variables.

Giving the nature of composites made of unidirectional laminae, being lamination parameters defined as integrals of trigonometric functions, their values are interrelated and need to lay within a feasible domain in order to possess physical meaning. A lot of research has concerned a proper definition of the feasible domain of lamination parameters[121, 122].

Let us now consider a certain property $\mathcal{P}[\boldsymbol{\psi}_g]$ of the structural behaviour. Its minimisation is expressed as

$$\begin{aligned} \underset{\boldsymbol{\psi}_g}{\text{minimise}} \quad & \mathcal{P}[\boldsymbol{\psi}_g] \\ \text{subject to} \quad & \|\boldsymbol{\psi}_g\|_\infty \leqslant 1 \\ & \mathcal{D}[\boldsymbol{\psi}_g] \leqslant 0 \end{aligned} \tag{6.14}$$

where $\mathcal{D}[\boldsymbol{\psi}_g]$ defines the boundary of the feasible domain. For each independent control point of the isogeometric grid, the number of optimisation variables is $lp = 12$.

Under the hypothesis of a special-ortotropic layup characrerised by symmetric and balanced laminate and by neglecting the flexural-torsional coupling, the non-zeros lamination parameters are only four, namely ψ_1^A, ψ_2^A, ψ_1^D, ψ_2^D. In this particular case, Wu et al. [120] propose to approximate the feasible domain a

$$\begin{cases} 5(\psi_1^A - \psi_1^D)^2 - 2(1 + \psi_2^A - 2(\psi_1^A)^2) \leqslant 0 \\ (\psi_2^A - 4t\psi_1^A + 1 + 2t^2)^3 - 4(1 + 2|t| + t^2)^2(\psi_2^D - 4t\psi_1^D + 1 + 2t^2) \leqslant 0 \\ (4t\psi_1^A - \psi_2^A + 1 + 4|t|)^3 - 4(1 + 2|t| + t^2)^2(4t\psi_1^D - \psi_2^D + 1 + 4|t|) \leqslant 0 \end{cases} \tag{6.15}$$

where t assumes the values $0, \pm 0.2, \pm 0.4, \pm 0.6, \pm 0.8, \pm 1.0$. Equations (6.15) define $\mathcal{P}[\boldsymbol{\psi}_g]$ by means of 23 inequality constraint for each independent control point.

The optimal design problem is solved using a gradient based optimiser, namely the Global Convergent Method of Mooving Asimptotes (GCMMA) [123]. It is an algorithm devised for the optimisation of objective functions that require a relatively high computational cost to evaluate the gradient and that are characterised by a high number of optimisation variables. It is based on convex subsequent approximations of the objective function.

Constructing the gradient of the objective function with respect to lamination parameters is not a simple task and it is computed numerically. The i^{th} component of the gradient is evaluated as

$$\nabla \mathcal{P}_i[\psi_g] \approx \frac{\mathcal{P}[\psi_g + h\boldsymbol{e}_i] - \mathcal{P}[\psi_g]}{h} \tag{6.16}$$

with h a conveniently small real parameter chosen to define an appropriate and accurate discrete incremental ratio, and $\boldsymbol{e}_i$ is a basis vector whose i^{th} component assumes unitary value while the other ones are zero. The evaluation of the gradient at point ψ_g requires that the equilibrium path is drawn for each component of $[\psi_g]$. Even if in general the task is extremely time consuming, the relative efficiency of Koiter's method allows to restrain its computational cost within an acceptable range. Moreover, generally GCMMA converges in a low number of iteration, allowing to further reduce the weight of the evaluation of the gradient in the overall computational cost of optimisation process.

6.3.3 Stage two: fibre angle retrieval

The second stage of optimisation is aimed at retrieving a fibre angle distribution. The problem consists in finding a fibre angle distribution to which corresponds a lamination parameters distribution that closely matches the optimal lamination parameters distribution found during stage 1. In detail, the objective function is formulated in terms least-square distance between the lamination parameters related to the unknown fibre angle distribution and the target distribution.

Following the concept of unified framework for the optimisation of shell structures, the fibre distribution ϑ is described by a control grid interpolated by NURBS function as well

$$\vartheta[\zeta] = \mathbf{N}_d[\zeta]\vartheta_e \tag{6.17}$$

where ϑ_e represents the values of the fibre orientations at the control points of the element. The global vector that collects the fibre orientations of all the control points is denoted with ϑ_g and the optimisation problem is

$$\begin{aligned} \underset{\vartheta_g}{\text{minimise}} \quad & \mathcal{E}[\vartheta_g] = \sum_{i=1}^{np}\sum_{j=1}^{lp} \frac{(\psi_j[\vartheta[\bar{X}_i]] - \psi_j[\bar{X}_i])^2}{np} \\ \text{subject to} \quad & ||\vartheta_g||_\infty \leqslant \pi/2 \\ & \mathcal{C}[\vartheta_g] \leqslant 0 \end{aligned} \tag{6.18}$$

where $\bar{X}_i$, with $i = 1 \dots np$, represents a sufficiently refined set of point over the domain in which the condition is tested, lp is the number of lamination parameters for each point, and $\mathcal{C}[\vartheta_g] \leqslant 0$ is a set of manufacturing constraints that the fibre tow must satisfy. This problem is non-convex and non-linear and is usually solved using stochastic minimisation algorithms. However, also in this case GCMMA has proven to be effective. Due to the presence of multiple local minima, a multi-start procedure needs to be employed to guarantee an acceptable response. The gradient of the objective function in Eq. (6.18) is evaluated by employing the complex-step procedure [124]. The i^{th} component of the gradient is evaluated as

$$\nabla \mathcal{E}_i[\vartheta_g] \approx \frac{\mathrm{Im}\left(\mathcal{E}[\vartheta_g + i\, h \boldsymbol{e}_i]\right)}{h} \tag{6.19}$$

with h a small real parameter that can be assumed of the order of the machine tolerance, $1.0e-20$ for instance, i is the imaginary unit, Im is the operation that considers the imaginary part of the result and $\boldsymbol{e}_i$ is a basis vector whose i^{th} component assumes unitary value while the other ones are zero.

6.4 NUMERICAL RESULTS

In this section numerical applications of the proposed optimisation procedures are given. In particular, the section is divided into three part. At first, two straight fibre composite structures are optimised by employing the stochastic procedures previously presented. Afterwards, a VAT full-scale structure is optimised using the Monte Carlo Algorithm. Finally, results obtained using the two-step strategy based on lamination parameters are given.

6.4.1 Straight-fibre laminates

Two examples of stacking sequence optimisation based on the proposed stochastic strategy are presented in this subsection. Non-conventional straight fibre laminates are considered. In the first one, we look for the optimal values of two layup of a curved panel in compression and, due to the relatively small complexity of the problem, the uniform scanning approach is employed. The second test regards the optimisation of a stacking sequence defined by eight parameters, that is the fibre orientation of each layer, and the random scanning approach is used. The objective function is a collapse load, defined as the minimum between the limit load, if exists, and the load related to a design displacement of a control point of the structure $\bar{u}_d$, namely

$$\mathcal{P}[\boldsymbol{\vartheta}] = -\lambda_c[\boldsymbol{\vartheta}] = -\min\left(\lambda_{lim}, \lambda[\bar{u}_d]\right) \tag{6.20}$$

The optimisation problem, in this case, specifies as

$$\begin{aligned} &\underset{\boldsymbol{\vartheta}}{\text{maximise}} && \lambda_c(\boldsymbol{\vartheta}) \\ &\text{subject to} && \vartheta_i \in \{-90^\circ, -72^\circ, \dots, 72^\circ, 90^\circ\} \end{aligned} \tag{6.21}$$

where ϑ_i is the fibre orientation of the ith layer and $\boldsymbol{\vartheta}$ is the vector collecting all ϑ_i.

The capability of the proposed approach for describing the overall structural behaviour as well as finding optimal solutions can be noticed, highlighting the strong influence of the layup on the collapse load. Concerning the sensitivity analysis for the detection of the worst imperfection shape, the results provided by Koiter's method with the two a-posteriori account of the imperfections (K_{lin} and K_{quad}) are compared with the solution obtained using the standard arc-length method (labelled as Riks) taken as baseline result.

6.4.1.1 *Curved panel in compression*

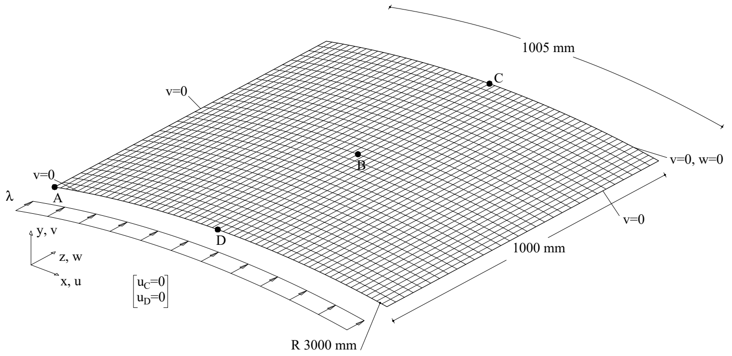

Figure 6.4: Curved panel: geometry and boundary conditions.

The test regards a curved cylindrical panel in compression. The geometry, the loads and the boundary conditions pictured in Fig.6.4 are related to the middle surface of the panel. The thickness of the shell is equal to $10\,\mathrm{mm}$.

The properties of the material are $E_1 = 30.6\,\mathrm{GPa}$, $E_2 = 8.7\,\mathrm{GPa}$, $\nu_{12} = 0.29$, $G_{12} = 3.24\,\mathrm{GPa}$, $G_{23} = 2.9\,\mathrm{GPa}$. The panel is composed of six layers and the stacking sequence is $[\pm\vartheta_1, \pm\vartheta_2, \pm\vartheta_3]$, from inside-out and measured with respect to the 1-axis of the local reference system which is aligned with z. The structure is discretised by a mesh grid made of 60 solid-shell elements along the curved edges and 30 along the straight ones.

The optimisation problem consists in seeking the values of ϑ_1 and ϑ_3 which maximise the collapse load, while ϑ_2 is assumed constant and equal to $0°$.

The imperfection sensitivity analysis is carried out assuming random geometrical imperfections following the Monte Carlo method; the imperfections are generated as a linear combination of the displacement part of the buckling modes and uniformly distributed random numbers represent the coefficients of the combination. The resulting imperfection shape is scaled in order to have a maximum component equal to 0.1 of the thickness.

The space of the sought angles is uniformly scanned from $-90°$ to $90°$ every $18°$. The details of the two stages of the analysis are summarised in Table 6.1. The best 10 laminations detected in stage 1 are checked in stage 2. The same is done for the worst 10 laminations in order to show the great influence of the stacking sequence on the structural performances.

Table 6.1: Curved panel: parameters of the Monte Carlo simulation.

		stage 1	stage 2
	laminations	$N = 100$	$n = 20$
	ϵ_π tolerance	3/100	3/1000
	method	K_{lin}	K_{quad}
imperfections	starting	200	200
	increment	100	100
	maximum	2000	10000

The number of significant buckling modes for the construction of the ROM generally changes with the lamination and cannot be imposed a-priori. In this respect, an adaptive criterion of selection is used. It consists in including the modes corresponding to critical loads that do not exceed 1.5 times the lowest one. The deformation limit is reached when the displacement component w_A becomes greater than $2\,\mathrm{mm}$.

Figure 6.5 shows, for stage 1, the trend of the first buckling load and of the collapse load in the angles domain. It can be observed that, as expected, the buckling load values are not directly linked to the collapse loads. It is worth noting that the unstable cases are the most frequent (darkest areas) and produce a low collapse load coincident with the limit load, while the maximum values (lighter areas) of the collapse load correspond to stable cases where the

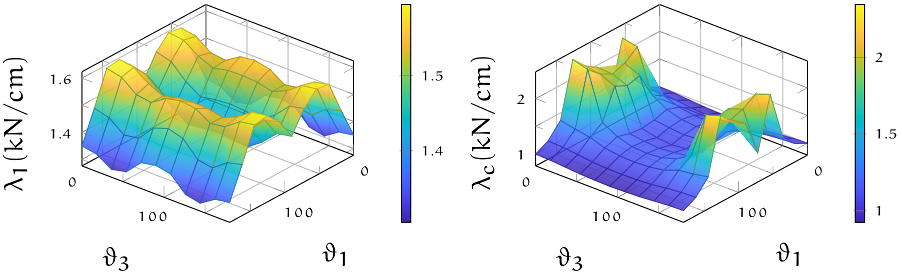

Figure 6.5: Curved panel: results of stage 1 in terms of first buckling load (left) and collapse load (right) trend with respect to the lamination angles.

deformation limit dominates. In Fig.6.6 the collapse load is normalised with respect to the first eigenvalue, showing that the former is much lower then the second one for the unstable cases and confirming that the linearised buckling load is not a reliable objective function for the optimisation.

The best and the worst 10 cases, in terms of collapse load, are summarised in Table 6.2 for both stages. It highlights that stage 2 gives smaller collapse loads than stage 1 and that the number of imperfections significantly increases between the two stages due to the more restrictive values for the distribution parameters σ and μ adopted. The analysis shows also that the best stacking sequences detected at stage 1 are also the optimal ones of the stage 2. Note also that, as expected, the worst cases are symmetric with respect to the fibre direction and this confirms the robustness of the proposal in terms of number of numerical experiments. For example the layup $[0_4/\pm 72]$ gives identical results as $[0_4/\mp 72]$. For the stable cases, since the control point A is not located on the symmetry axis, the results in terms of collapse load are not symmetric unlike the linearised buckling loads. See for instance the layups $[\mp 54/0_4]$ and $[\pm 54/0_4]$.

The extreme cases are analysed more deeply in the following. The stacking sequence $[0_4/90_2]$ furnishes the worst results in terms of collapse load. For this lamination, the equilibrium paths corresponding to the worst imperfection shape are reported in Fig.6.7 using the Koiter method, with both K_{lin} and K_{quad} approaches, and a path-following strategy. The solution found by K_{quad} is in accordance with the one of the path following analysis on the full FE model and, in particular, the collapse load is accurately predicted. Conversely, the cheaper approach K_{lin} gives a slightly higher value of the collapse load but is however able to capture the structural behaviour. The buckling modes and the quadratic correctives used in the Koiter analysis for building the ROM of the corresponding perfect structure are pictured in Fig.6.8 while Fig.6.9 and Fig.6.10

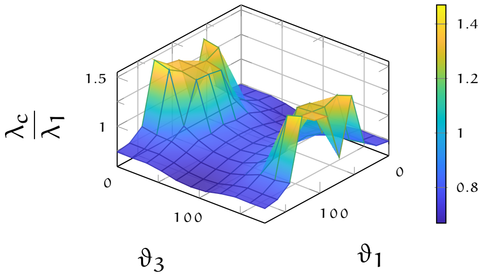

Figure 6.6: Curved panel: results of stage 1 in terms of collapse load normalised with respect to the first buckling load.

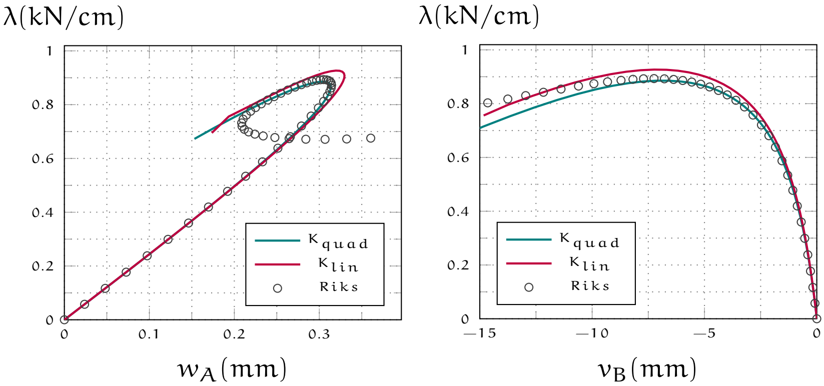

Figure 6.7: Curved panel: equilibrium path for the worst imperfection shape in stage 2, path following vs Koiter a-posteriori, lamination $[0_4/90_2]$.

Table 6.2: Curved panel: results of the best 10 and the worst 10 laminations. The loads are expressed in kN/cm.

	buckling loads			Stage 1			Stage 2		
lamination	λ_1	λ_2	λ_3	λ_c	$\frac{\lambda_c}{\lambda_1}$	N_i	λ_c	$\frac{\lambda_c}{\lambda_1}$	N_i
$[\mp 54/0_4]$	1.595	1.986	-	2.344	1.470	500	2.354	1.476	2797
$[\mp 54/0_2/\pm 18]$	1.587	1.971	-	2.265	1.427	500	2.304	1.452	1599
$[\mp 54/0_2/\mp 18]$	1.587	1.975	-	2.260	1.424	499	2.294	1.445	1698
$[\pm 54/0_4]$	1.595	1.986	-	2.245	1.408	500	2.277	1.428	1699
$[\pm 54/0_2/\pm 18]$	1.587	1.975	-	2.187	1.377	500	2.228	1.404	1699
$[\pm 54/0_2/\mp 18]$	1.587	1.971	-	2.148	1.354	500	2.215	1.396	1298
$[\mp 72/0_4]$	1.548	1.993	-	2.107	1.361	500	2.172	1.403	2100
$[\mp 72/0_2/\pm 18]$	1.535	1.966	-	2.061	1.343	500	2.122	1.383	1597
$[\mp 72/0_2/\mp 18]$	1.533	1.969	-	2.060	1.343	600	2.127	1.387	1600
$[\pm 72/0_2/\pm 18]$	1.533	1.969	-	2.014	1.314	600	2.074	1.353	1500
$[0]_6$	1.350	1.978	-	0.996	0.738	352	0.970	0.719	1499
$[0_4/\pm 18]$	1.340	1.938	-	0.987	0.736	466	0.966	0.720	2974
$[0_4/\mp 18]$	1.340	1.938	-	0.987	0.736	585	0.966	0.720	2064
$[0_4/\pm 36]$	1.305	1.799	-	0.965	0.740	493	0.945	0.724	2385
$[0_4/\mp 36]$	1.305	1.799	-	0.965	0.740	493	0.945	0.724	1791
$[0_4/\pm 54]$	1.317	1.661	-	0.944	0.717	500	0.910	0.691	3391
$[0_4/\mp 54]$	1.317	1.661	-	0.944	0.717	800	0.910	0.691	4679
$[0_4/\mp 72]$	1.371	1.632	2.022	0.933	0.680	500	0.894	0.652	2498
$[0_4/\pm 72]$	1.371	1.632	2.022	0.933	0.680	700	0.893	0.652	2100
$[0_4/90_2]$	1.382	1.628	1.962	0.925	0.669	500	0.885	0.641	2499

show the deformed configuration at collapse load and the worst imperfection shape, respectively. It is interesting to note as the worst imperfection shape does not correspond, in this case, to the first buckling mode and as all the buckling modes contribute to the deformed shape at the limit point.

To point out the influence of the number of buckling modes included in the ROM on the collapse load, an imperfection sensitivity analysis with 3 modes, that is the number used during the scan process, and 8 modes has been carried out for the case $[0_4/90_2]$. The minimum collapse load and its 5% fractile provided when increasing the imperfections has been monitored. The results are pictured in Fig.6.11. The collapse load from the two cases stabilises at the same value although when 3 modes are employed it converges for a smaller number of imperfections. On the contrary, as expected, the fractiles are quite different because, by enlarging the number of the modes, the space of the possible imperfections also increases without providing any further information about the worst imperfection, which is well represented by the first 3 modes.

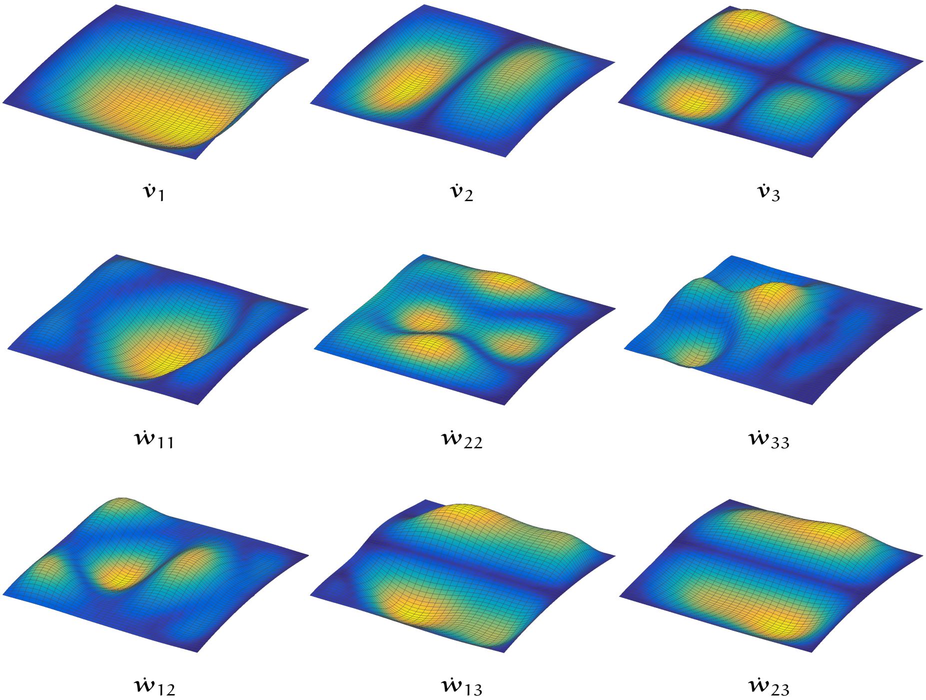

$\dot{v}_1$ $\dot{v}_2$ $\dot{v}_3$

$\dot{w}_{11}$ $\dot{w}_{22}$ $\dot{w}_{33}$

$\dot{w}_{12}$ $\dot{w}_{13}$ $\dot{w}_{23}$

Figure 6.8: Curved panel: buckling modes and quadratic correctives, case $[0_4/90_2]$.

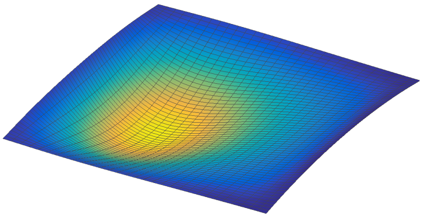

Figure 6.9: Curved panel: deformed shape at collapse point, case $[0_4/90_2]$.

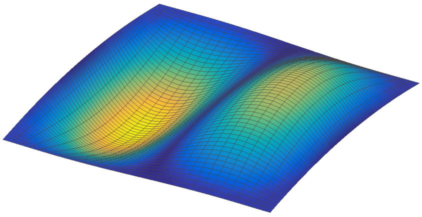

Figure 6.10: Curved panel: worst imperfection shape, lamination $[0_4/90_2]$.

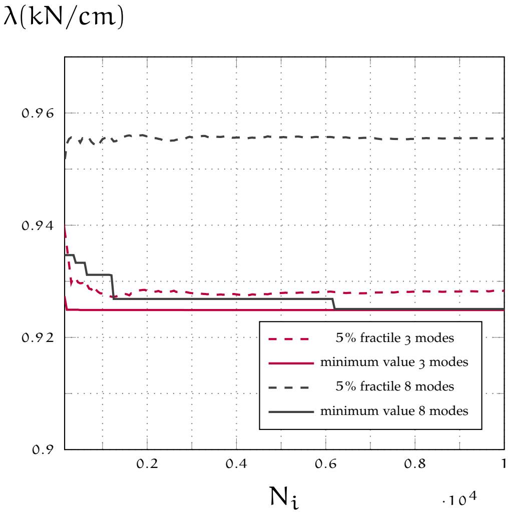

Figure 6.11: Curved panel: 5% fractile and minimum value of the collapse load versus number of imperfections for 3 and 8 modes, case $[0_4/90_2]$.

Moreover, for a fixed number of modes, the frequency distribution converges quickly. This can be seen in Fig.6.11 where the fractile does not change significantly, or in Fig.6.12 and Table 6.3 which show, for 8 modes, how the probability density function and the parameters of the distribution vary with the number of imperfections.

The other extreme lamination is $[\mp 54/0_4]$, characterised by a stable post critical behaviour and the highest collapse load. In Fig.6.14, the corresponding equilibrium paths traced by Koiter (ROM) and Riks (full FE model) analyses are reported showing a good agreement. The deformed configuration at the last evaluated equilibrium point is shown as well. The buckling modes and the corresponding corrective modes used to construct the ROM are pictured in Fig.6.15. Finally, to assess the choice of discretising the angles domain by 18°, the optimisation process is repeated with a finer discretisation of 6°. In this case, the method finds $[\mp 48/0_4]$ as the best layup with a collapse load $\lambda_c = 2,369$. The solution is just slightly better than that provided by the previous analysis, confirming that 18° was already a good choice.

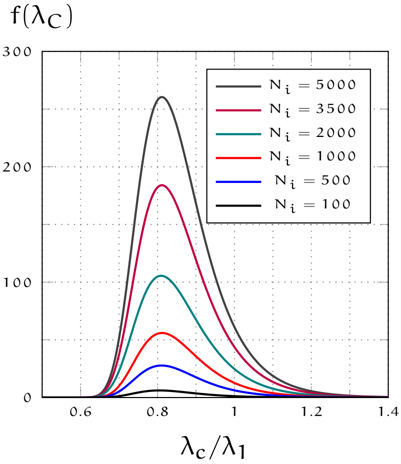

Figure 6.12: Curved panel: Gumbel max probability density function for different number of imperfections, lamination $[0]_6$, 8 modes.

Table 6.3: Curved panel: distribution parameters variation with the number of imperfections, lamination $[0]_6$.

N_i	μ	σ
100	-0.8049	0.0755
500	-0.8105	0.0788
1000	-0.8116	0.0786
2000	-0.8094	0.0809
3500	-0.8113	0.0806
5000	-0.8113	0.0801

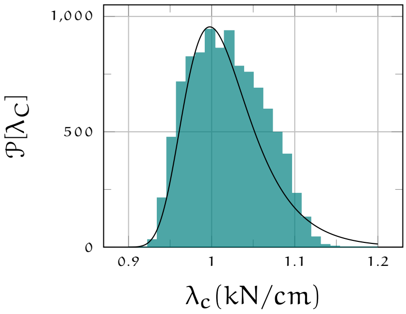

Figure 6.13: Curved panel: frequencies of the collapse load and fit by Gumbel max distribution, lamination $[0_4/90_2]$, 8 buckling modes, 10^4 imperfections.

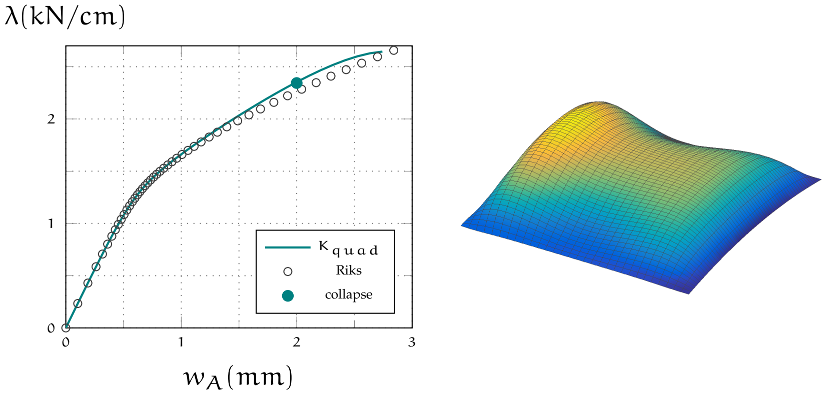

Figure 6.14: Curved panel: equilibrium path (left) and deformed shape at the last evaluated equilibrium point (right), lamination $[\mp 54/0_4]$.

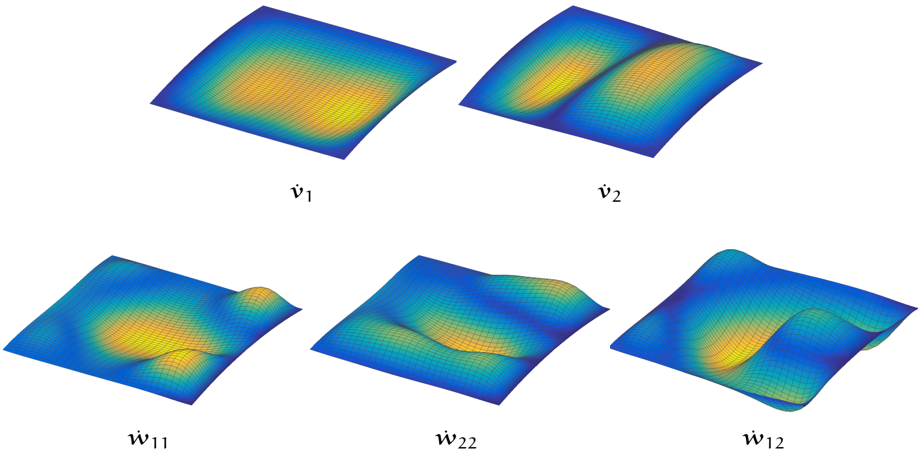
$\dot{\mathbf{v}}_1$ $\dot{\mathbf{v}}_2$

$\dot{\mathbf{w}}_{11}$ $\dot{\mathbf{w}}_{22}$ $\dot{\mathbf{w}}_{12}$

Figure 6.15: Curved panel: buckling modes and quadratic correctives for the case $[\mp 54/0_4]$.

6.4.1.2 *Stiffened panel*

The second test regards a curved panel with ”T” stiffeners in compression, like those commonly employed for aeronautical structures [112]. In Fig.6.16 an axonometric projection shows the geometry and the boundary conditions, while geometrical details of a section have been pictured in Fig.6.17. The v displacement of the lateral faces of the four panels is bounded and the deformation of only one curved edge is constrained, also along z. In the illustrations, it is possible to see the mesh grid details for the 3D solid-shell description of the structure. It is worth noting how the solid-shell finite element allows us to model, easily and accurately, the connection between the panel and the stiffeners, with no need for rigid links or offsets, in contrast to classical shell models. The curved faces and the stiffener ends are loaded by a uniform line load $\lambda = 1$.

The same material is employed for the skin and the stiffeners and it is characterised by $E_1 = 30.6\,\mathrm{GPa}$, $E_2 = 8.7\,\mathrm{GPa}$, $\nu_{12} = 0.3$, $G_{12} = 3.4\,\mathrm{GPa}$, $G_{23} = 2.9\,\mathrm{GPa}$, with respect to the local reference system which has the direction 1 aligned with the global direction z while the direction 3 is along the normal at the middle plane of the skin. The stiffener lamination is supposed to be constant and equal to $0°$, while eight layers define the lamination of the skin labelled as $[\vartheta_1/\ldots/\vartheta_8]$ where every ϑ_i is a multiple of $18°$ and can vary from $-90°$ to $90°$. The purpose of the test is studying the variability of the post-critical behaviour when the lamination changes and seeking the laminations with the maximum collapse load. The solutions with minimum collapse load are searched as well, just to identify the range of variability of the structural performances. The collapse load for the stable configurations is the load producing the deformation limit $w_A = 4\,\mathrm{mm}$. As in the first test, the buckling modes employed for the ROM of the Koiter analyses correspond to buckling loads which do not exceed 1.5 times the first one.

The parameters used to set up the three stages of the random scanning approach are reported in Table 6.4. In the first stage, $N_1 = 2500$ random uniformly generated laminations are analysed and the $n_1 = 10$ best and the 10 worst laminations (in terms of collapse load), reported in Table 6.5, are selected. In the second stage, for each of these configurations, a further $N_2 = 100$ randomly generated laminations are considered with each layer angle that can vary between $-36°$ and $36°$ with an increment of $18°$ with respect to the likely optimal values identified by the first stage. Lastly, in stage 3 the best $n_2 = 10$ and the worst 10 results obtained in stage 2, and labelled as indicated in Table 6.6, are analysed using the accurate account of geometrical imperfections and a

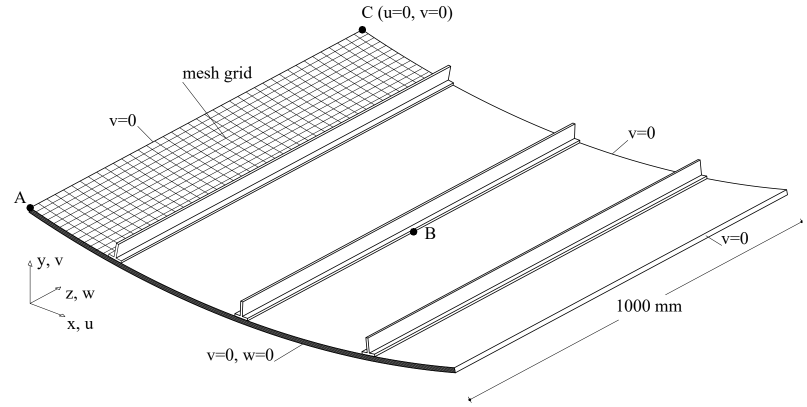

Figure 6.16: Stiffened panel: geometry and boundary conditions.

more restrictive tolerance for parameters μ and σ; a summary of the results is reported in Table 6.7.

Even though the number of finite element parameters is quite significant, the code is not really time consuming. For instance, the average time taken by a prototype code for analysis each layup at stage 1 is 32.02 seconds (i7-6700HQ CPU 2.6Ghz, Matlab R2016a, single core) considering that the average number of imperfections per layup is 805.

The curves in Fig.6.18 plot the collapse load, the two lowest buckling loads λ_1 and λ_2 and the ratio between the collapse load and the first eigenvalue as

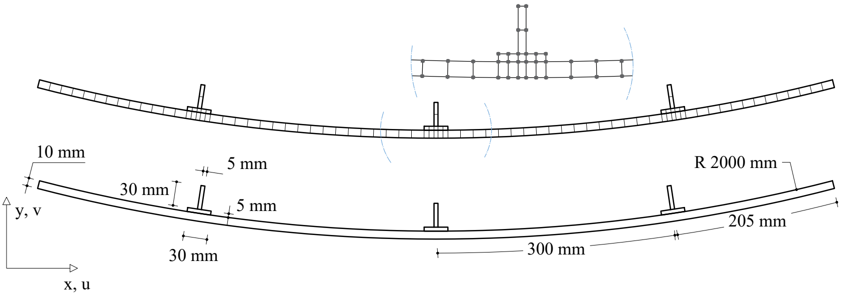

Figure 6.17: Stiffened panel: section geometry and mesh.

Table 6.4: Stiffened panel: parameters of the Monte Carlo simulation.

		stage 1	stage 2	stage 3
	laminations	2500	2000	20
	tolerance	3/100	5/1000	3/1000
	method	K_{lin}	K_{lin}	K_{quad}
imperfections	starting	50	200	200
	increment	50	50	100
	maximum	2000	2000	10000

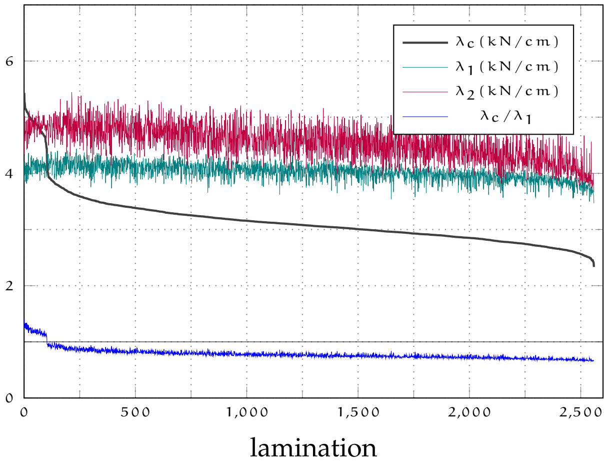

Figure 6.18: Stiffened panel: collapse load and buckling loads for the lamination in order of decreasing collapse load, stage 1.

a function of a lamination index. This is an integer number which is assigned to each lamination after they are ordered in terms of decreasing collapse load. The laminations with the smallest index have a stable behaviour and collapse for reaching the deformation limit. The buckling loads in these cases are well separated from each other. The first buckling load is actually quite constant with the lamination though, when the second one gets closer to it, the collapse load, due to modal interaction phenomenon, drastically reduces. This behaviour is significantly more evident in Fig.6.19 where the results of stage 2 are reported. The best laminations in terms of collapse load are characterised by an evident distance between the first and the second linearised buckling load and exhibit a stable behaviour. Conversely, for the worst laminations, the second eigenvalue is

Table 6.5: Stiffened panel: results of the best 10 and the worst 10 laminations, stage 1. The loads are expressed in kN/cm.

lamination	λ_1	λ_2	λ_c	$\lambda_{c,5}$	λ_c/λ_1	N_i
$[18/36/-18/72/0_4]$	3.8805	4.3430	5.4337	-	1.4003	350
$[-72/36/72/-18/0/72/0/-18]$	4.2127	5.0184	5.2665	-	1.2501	350
$[-72/36/-18/-36/18/0/-18/0]$	3.9662	4.8839	5.2580	-	1.3257	200
$[-54_2/0/-36/-18/0/18/0]$	3.8521	4.7065	5.1439	-	1.3354	350
$[90/-72/0/18_2/0/-18/0]$	3.8604	4.7119	5.0942	-	1.3196	550
$[54_2/18/0/54/0/-18/0]$	3.8930	4.7015	5.0641	-	1.3008	300
$[72/-54/72_2/0/-72/0_2]$	4.3619	4.9789	5.0532	-	1.1585	350
$[36/54/-72/18/36/0_2/-18]$	4.0863	4.7736	4.9990	-	1.2234	400
$[72/-54/36/18/-36/18/0_2]$	4.0992	4.9873	4.9985	-	1.2194	300
$[54/72/0/72/36/0_2]$	3.9844	4.6742	4.9831	-	1.2506	250
$[-18/-36/-18/-36_2/72/-72/90]$	3.6837	3.7316	2.4582	2.4614	0.6673	300
$[-18/0/18/90_2/-54_2/-72]$	3.6686	3.7659	2.4519	2.4539	0.6683	250
$[0_2/-54/72_2/-54/72/-72]$	3.7314	3.7613	2.4511	2.4534	0.6569	300
$[18_2/-72_2/36/-54/54_2]$	3.6627	3.8805	2.4505	2.4525	0.6690	300
$[18_2/-36/-72/-54/-72/90/-54]$	3.6901	3.7830	2.4503	2.4525	0.6640	400
$[-18_2/54/-72/-54/72/90/-72]$	3.6955	3.8094	2.4295	2.4316	0.6574	400
$[0/-54/-72_2/(-54/90)_2]$	3.6464	3.9985	2.4255	2.4286	0.6652	250
$[18/-18/54_2/-72_3/-54]$	3.6160	3.8386	2.4211	2.4234	0.6696	300
$[0/18/-36/-72/54_2/90/72]$	3.6131	3.7729	2.4016	2.4048	0.6647	450
$[18_2/0/36/54/72/54/72]$	3.4698	3.6626	2.3334	2.3359	0.6725	250

very close to the first one and the modal interaction leads to a relevant unstable behaviour with an imperfection sensitive limit load.

Some equilibrium paths are presented in Fig.6.20. The collapse loads predicted by the Koiter method are practically coincident with those provided by the Riks analysis with the full FE model. The buckling modes used in the ROM and some quadratic correctives are pictured in Fig.6.21 and in Fig.6.24 for the laminations L1 and L20 respectively. In addition, Fig.6.22 shows the worst imperfection shape detected in stage 2 for the lamination L20 and the corresponding deformed shape at the limit point is reported in Fig.6.23. The convergence of the Monte Carlo optimisation is shown in Fig.6.25, that is the trend of the maximum and the minimum collapse load for an increasing number of analysed laminations. In particular, a little over a thousand of layups has to be considered to obtain a converged value of the maximum collapse load. Lastly, Fig.6.26 indicates how the structural behaviour in terms of equilibrium path drastically changes with the stacking sequence and, in particular, how the post-critical behaviour varies from strongly unstable to stable, confirming again the great influence of a stacking sequence optimisation.

Table 6.6: Stiffened panel: labels of the best 10 and the worst 10 laminations, stage 2.

label	lamination
L1	$[-72/18/-18_2/0/18/0_2]$
L2	$[72/0/-18/-36/0_2/-18/0]$
L3	$[-72/18/72/-18/18/72/0_2]$
L4	$[-54/0/-18/-72/18/0_2/18]$
L5	$[-72/54/-36/0/18/0_2/18]$
L6	$[-72/-18/36/0/-72/0_2/18]$
L7	$[0/72/-18/36/18/0/18/0]$
L8	$[90/18/0/-18/18_2/-18/0]$
L9	$[72/18/-54/18/0_2/36/0]$
L10	$[-72/54/0/-36/(0/18)_2]$
L11	$[0/-54_4/90/-72/-54]$
L12	$[0_2/-72/90/-72/-54/-72/90]$
L13	$[-18/0/72_2/90/54/72_2]$
L14	$[-18_2/72_2/-72/90/-54_2]$
L15	$[-18_2/72/90_3/-72/-54]$
L16	$[18/-72/-54/-72_2/90/-72]$
L17	$[0/18/54_2/72/90/-72/72]$
L18	$[0/-18/-54_2/90/-72/90/72]$
L19	$[-18_2/36/-72/-54/90/72_2]$
L20	$[0_2/54/72_2/90_2/72]$

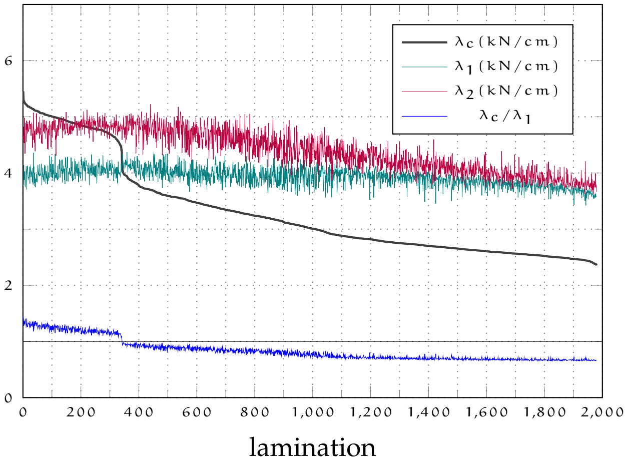

Figure 6.19: Stiffened panel: collapse load, fractile and buckling loads for the lamination in order of decreasing collapse load, stage 2.

Table 6.7: Stiffened panel: stage 2 and stage 3 results. The loads are expressed in kN/cm.

	buckling loads				Stage 2			Stage 3		
	λ_1	λ_2	λ_3	λ_4	λ_c	$\frac{\lambda_c}{\lambda_1}$	N_i	λ_c	$\frac{\lambda_c}{\lambda_1}$	N_i
L1	3.771	4.663	5.610	-	5.450	1.442	850	5.463	1.449	1200
L2	3.801	4.605	5.645	-	5.302	1.395	1100	5.314	1.398	2200
L3	4.140	4.823	5.975	-	5.289	1.276	600	5.300	1.280	2500
L4	3.876	4.534	5.713	-	5.277	1.361	900	5.286	1.364	2100
L5	4.016	4.982	5.786	-	5.260	1.310	600	5.250	1.307	2200
L6	4.025	4.762	5.826	-	5.254	1.306	950	5.260	1.307	1700
L7	3.785	4.344	5.644	-	5.238	1.384	700	5.244	1.386	3600
L8	3.752	4.615	5.573	-	5.236	1.396	800	5.242	1.397	1600
L9	3.956	4.781	5.713	-	5.229	1.322	950	5.238	1.324	800
L10	3.971	4.891	5.720	-	5.227	1.316	950	5.240	1.320	1400
L11	3.587	3.864	5.110	5.305	2.389	0.666	750	2.381	0.664	2300
L12	3.550	3.809	5.000	5.111	2.387	0.672	800	2.380	0.670	2598
L13	3.562	3.835	5.111	5.131	2.387	0.670	1000	2.380	0.668	2200
L14	3.618	3.752	5.238	5.341	2.382	0.658	750	2.374	0.656	1800
L15	3.618	3.765	5.195	5.343	2.381	0.658	1100	2.373	0.656	1400
L16	3.563	3.992	5.184	5.220	2.378	0.667	500	2.373	0.666	2300
L17	3.621	3.757	5.116	5.255	2.380	0.657	700	2.369	0.654	1400
L18	3.585	3.744	5.058	5.269	2.373	0.662	650	2.364	0.659	1900
L19	3.579	3.774	5.153	5.289	2.371	0.662	750	2.362	0.660	1600
L20	3.579	3.663	4.967	5.140	2.353	0.658	900	2.345	0.655	1500

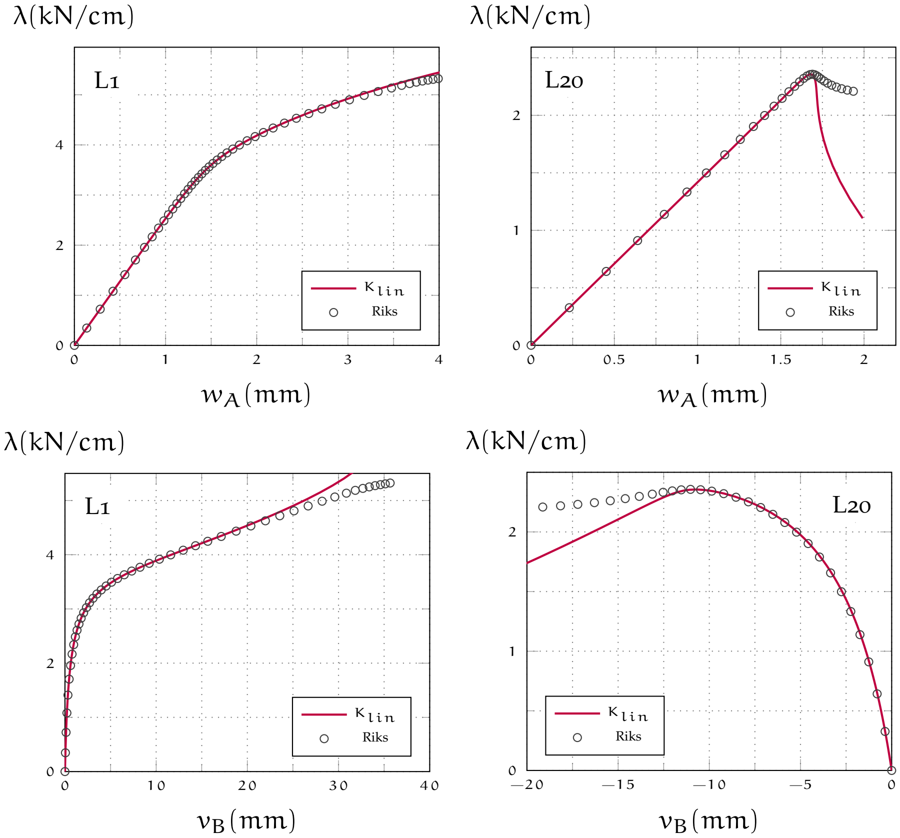

Figure 6.20: Stiffened panel: equilibrium paths for the worst imperfection shape and laminations L1 and L20, path following vs Koiter.

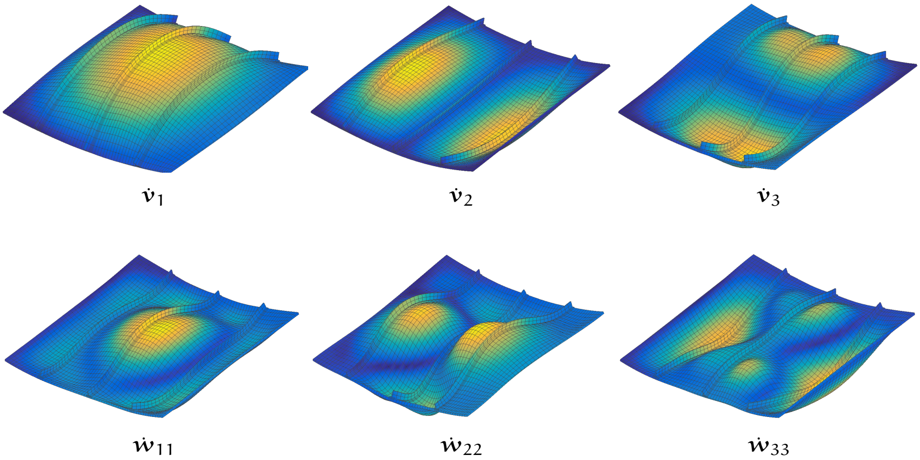

$\dot{\boldsymbol{v}}_1$ $\dot{\boldsymbol{v}}_2$ $\dot{\boldsymbol{v}}_3$

$\dot{\boldsymbol{w}}_{11}$ $\dot{\boldsymbol{w}}_{22}$ $\dot{\boldsymbol{w}}_{33}$

Figure 6.21: Stiffened panel: buckling modes and quadratic correctives, case L1.

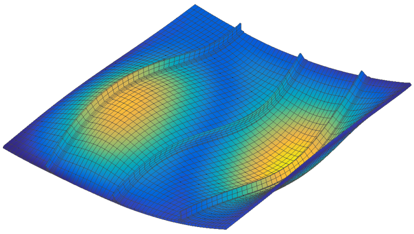

Figure 6.22: Stiffened panel: worst imperfection shape, L20.

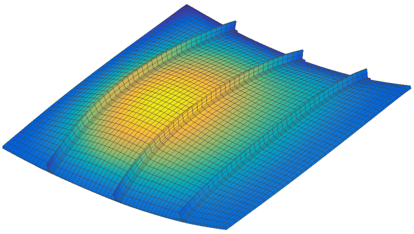

Figure 6.23: Stiffened panel: deformed shape at collapse point, L20.

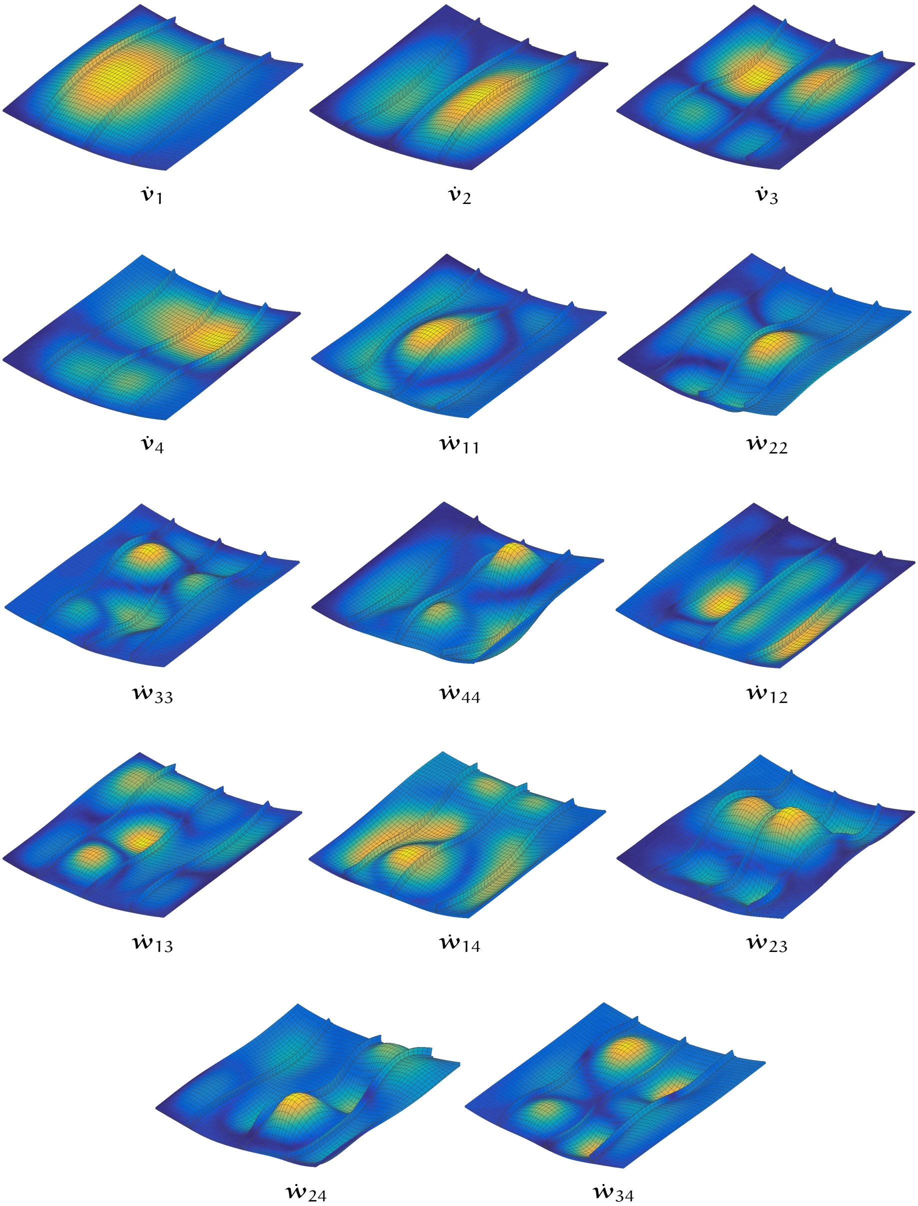

$\dot{\boldsymbol{v}}_1$ $\dot{\boldsymbol{v}}_2$ $\dot{\boldsymbol{v}}_3$

$\dot{\boldsymbol{v}}_4$ $\dot{\boldsymbol{w}}_{11}$ $\dot{\boldsymbol{w}}_{22}$

$\dot{\boldsymbol{w}}_{33}$ $\dot{\boldsymbol{w}}_{44}$ $\dot{\boldsymbol{w}}_{12}$

$\dot{\boldsymbol{w}}_{13}$ $\dot{\boldsymbol{w}}_{14}$ $\dot{\boldsymbol{w}}_{23}$

$\dot{\boldsymbol{w}}_{24}$ $\dot{\boldsymbol{w}}_{34}$

Figure 6.24: Stiffened panel: buckling modes and quadratic correctives, case L20.

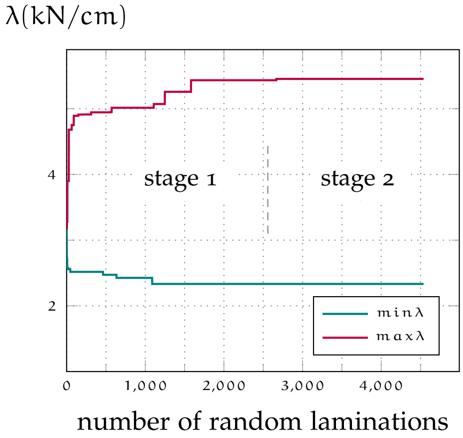

Figure 6.25: Stiffened panel: maximum and minimum collapse loads when the laminations increase.

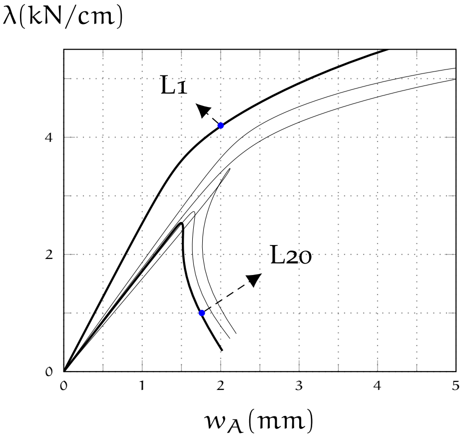

Figure 6.26: Stiffened panel: equilibrium paths for some laminations at stage 2.

6.4.2 Fibre-path parameterisation

In this subsection, we focus on the optimisation of a VAT structure using a fibre path parametersation and the stochastic procedures previously described. The numerical result concern a full-scale structure, namely a new-generation VAT composite wingbox recently proposed at University of Limerick [18]. In the following, at first a description of the wingbox is given. Then, the wingbox in the initial design is analysed using the proposed Koiter's algorithm to validate the model. This initial design is taken as baseline result for the optimisation obtained using MCA and GA and afterwards described.

6.4.2.1 *VAT composite wingbox*

The wingbox under consideration is representative of a medium-range civil aircraft having a maximum take-off mass of 75t and a wingspan of $2b = 36m$ (see Fig.6.27). In particular, Oliveri et al. [18] designed the wingbox assuming that it is located at about the 85% of the aircraft's half wingspan between two ribs.

The cross-sectional dimensions have been designed considering a linear-elastic beam model with a Quasi Isotropic (QI) composite layup under an elliptical load distribution that simulates the load during cruise [125]. During the design process, for each cross-section of the beam, the second moment of area along the X axes (see Fig.(6.28)) has been assumed to be proportional to the bending moment along the X axes. Therefore, by imposing the deflection of the tip of the wing to be equal to a design value (i.e. a percentage of b), it was possible to evaluate the forces and moments acting on a generic cross-section of the wing [18].

The main geometrical quantities of the wingbox under consideration are shown in Fig.6.29. More details regarding the geometry and their design process can be found in Oliveri et al. [18]. In Fig.6.30 the loading and boundary conditions of the wingbox are shown. In particular, the wingbox is considered to be loaded on one end by a shear force $F_A = 23.8kN$ and a flexural moment $M_A = 14.28kNm$, while the opposite side is fully clamped.

The layup of the wingbox was chosen to perform well against buckling. It is reported in Table 6.8 and denoted by SS_0 in the following. The angle 0 is measured in the direction of the local tangent at the surface ($\mathbf{e}_3$) with respect to the direction $\mathbf{e}_1$, referring to the local reference system of each panel shown in Fig.6.28. It has been assigned such that the direction $\mathbf{e}_1$ aligns with the direction $\mathbf{Y}$ of the global system and $\mathbf{e}_3$ goes from the inside out. The layups of the variable angle tow panels are expressed in according to the notation

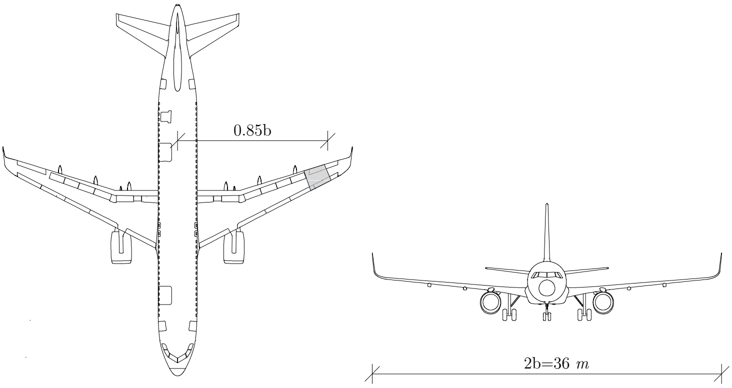

Figure 6.27: Wingbox position on the aircraft.

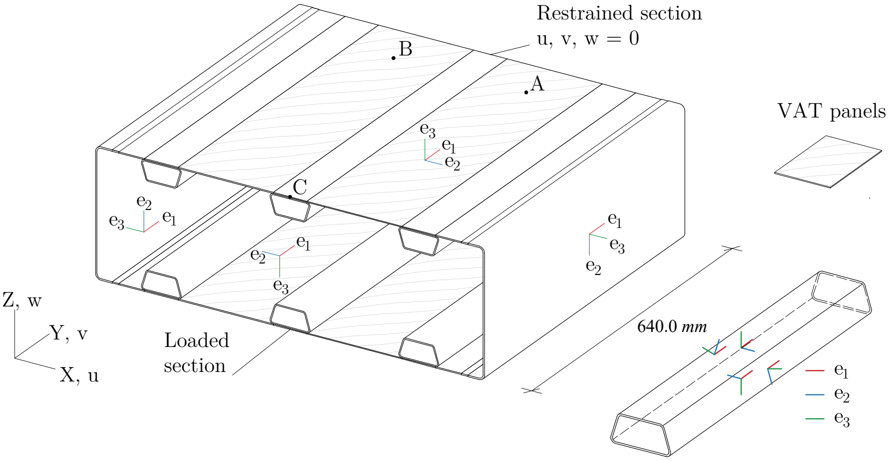

Figure 6.28: Geometry, loading and boundary conditions of the wingbox.

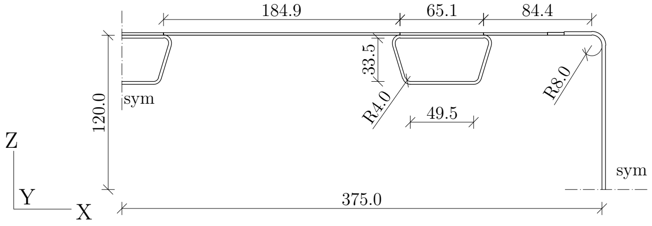

Figure 6.29: Detailed view of the cross-section of the wingbox. All the lengths are expressed in *mm*.

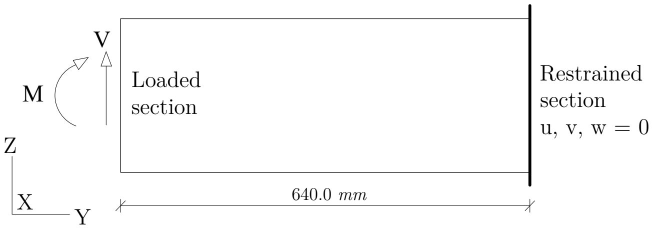

Figure 6.30: Loads and boundary conditions applied at the two end sections of the wingbox.

Table 6.8: Layup SS_0 of the wingbox.

Part	stacking sequence
Skin bay	$90/[(0 \pm \langle 52\|35 \rangle)/0/\pm 45]_S$
Skin	$90/[\pm 35/0/\pm 45]_S$
Stiffener	$[90/45/0_2/-45/0]_S$
Spar web	$90/[\pm 35/0_3/\pm 45]_S$

Table 6.9: Material properties.

$E_1 [GPa]$	$E_2 [GPa]$	$G_{12} [GPa]$	ν_{12}
135.00	7.54	5.00	0.30

of Gürdal and Olmedo [92]. The material properties are given in Table 6.9 and the thickness of each layer is $0.1875\,mm$. As shown in Table 6.8, the skin comprises eleven layers, while four additional 0° layers have been added to the spar webs for increasing their stiffness. The wingbox has been designed to keep the principal strains under a limit value, namely $\varepsilon_{lim} = 2500\mu\epsilon$. Figure 6.31, shows an image of the wingbox manufactured at University of Limerick [18].

6.4.2.2 *Optimisation problem*

The goal of the current optimisation study is to minimise the out-of-plane displacement of the wingbox under a design load. In fact, the most notable effect observed in the wingbox in the postbuckling regime is an increasing transverse displacement of the skin panels in compression. Consequently, its minimisation improves the postbuckling performances, as shown by Raju et al. [7]. The maximum out-of-plane displacement is denoted by $w_{c,max}$ and is measured at the points where the maximum amplitude of the buckling modes occurs. The design load is 1.2 times the applied load.

The optimisation variables are the angles of the stacking sequence, denoted as $\boldsymbol{\vartheta} = [\vartheta_1, \ldots, \vartheta_6]$. The first layer of 90° is kept constant due to manufacturing need [18]. The optimisation is based on a fibre path parameterisation according to Gürdal and Olmedo [92]. Table 6.10 shows the parametric layup. The fibre angle of skin and web is compatible at the corners, guaranteeing the continuity of the fibre path. The angles are constrained to integer values and their domain is defined from $-90°$ to $90°$.

Strains and tip displacement are constrained to be less than $\varepsilon_{lim} = 2500\mu\epsilon$, and $w_{lim} = w_{QI,max} = 2.38\,mm$, respectively. These constraints are included

Figure 6.31: Manufactured wingbox, from [18].

Table 6.10: Parametric fibre paths used in the optimisation problem.

Part	stacking sequence
Skin bay	$90/[(0 \pm \langle \vartheta_1 \vert \vartheta_2 \rangle)/0/(0 \pm \langle \vartheta_4 \vert \vartheta_3 \rangle)]_S$
Skin	$90/[\pm\vartheta_2/0/\pm\vartheta_3]_S$
Stiffener	$[90/45/0_2/-45/0]_S$
Spa web	$90/[(0 \pm \langle \vartheta_5 \vert \vartheta_2 \rangle)/0_3/(0 \pm \langle \vartheta_6 \vert \vartheta_3 \rangle)]_S$

in the optimisation process by assigning a penalty value to the objective function if any limit is exceeded

$$\mathcal{P}(\vartheta) = \begin{cases} \dfrac{|w_{max}|}{w_{lim}} + c_1 & \text{if} \quad |w_{max}| > w_{lim} \\ \dfrac{|\varepsilon_p|}{\varepsilon_{lim}} + c_2 & \text{if} \quad |\varepsilon_p| > \varepsilon_{lim} \\ |w_{c,max}| & \text{otherwise.} \end{cases} \tag{6.22}$$

where w_{max} is the tip displacement, ε_p is the maximum principal strain, c_1 and c_2 are the penalty constants. If both the limits are exceeded, the highest value evaluated by Eq.(6.22) is applied.

The VAT steering radius is constrained to exceed a minimum value to guarantee manufacturability. The limit amplitude is $R_{lim} = 400\,mm$, according to results previously presented [107].

Table 6.11: Buckling loads for the initial stacking sequence (SS_0).

mode	1	2	3	4	5	6	7	8
λ	1.1417	1.1555	1.2017	1.2133	1.4285	1.4385	1.5073	1.5269
λ/λ_1	1.000	1.0121	1.0526	1.0627	1.2512	1.2600	1.3202	1.3374

Finally, the optimisation problem can be stated as

$$\begin{aligned} \underset{\vartheta}{\text{minimise}} \quad & f(\vartheta) \\ \text{subject to} \quad & c_r(T_{0,\nu}, T_{1,\nu}) \leqslant 0, \quad \nu = 1 \dots n_{vat} \\ & \vartheta_i \in \mathcal{N} \\ & -90^\circ \leqslant \vartheta_i \leqslant 90^\circ, \quad i = 1 \dots 6 \end{aligned} \tag{6.23}$$

The nonlinear displacements and strains are evaluated using Koiter's method.

6.4.2.3 *Analysis of the baseline configuration*

Hereafter, we focus on the postbuckling behaviour of the baseline wingbox. This stage is useful to validate the FE model and to assess the suitability of Koiter's method.

The use of the solid-shell model gives has the advantage that, due to the 3D description, the connection between the stiffeners and the skin can be modelled without rigid links. Moreover, the continuity of the skin is preserved in the zones of variable thickness, unlike classical shell finite elements that need an offset to define the actual position of the panels.

We first present the results of a linear buckling analysis carried out on the FE model. Then, we perform the geometrically non-linear analysis with Koiter's method. The results in terms of equilibrium path are compared with those provided by an arc-length strategy. It employs the same FE description used by Koiter so that the differences can only be attributed to the solution algorithm. In addition, so as to exclude errors in the FE model, the results are compared with Abaqus/Standard.

LINEAR BUCKLING ANALYSIS The first eight buckling loads are reported in Table 6.11. The first six modes are shown in Fig.6.32. The first buckling load is 27.17kN, that is in agreement with the result of the static test performed on the wingbox by Zucco et al. [126] who gave the measured value of $26.10 - 27.20$kN.

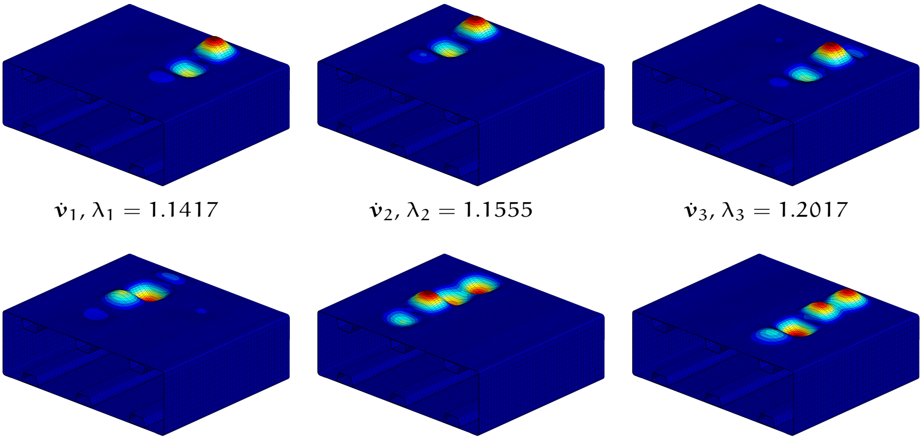

$\dot{v}_1, \lambda_1 = 1.1417$ $\dot{v}_2, \lambda_2 = 1.1555$ $\dot{v}_3, \lambda_3 = 1.2017$

$\dot{v}_4, \lambda_4 = 1.2133$ $\dot{v}_5, \lambda_5 = 1.4285$ $\dot{v}_6, \lambda_6 = 1.4385$

Figure 6.32: Buckling modes for the initial stacking sequence.

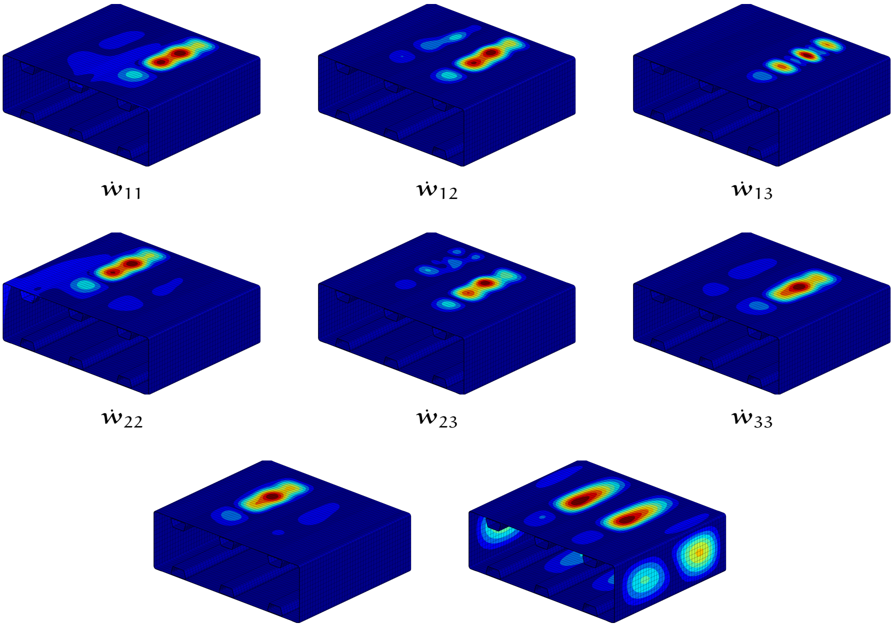

$\dot{w}_{11}$ $\dot{w}_{12}$ $\dot{w}_{13}$

$\dot{w}_{22}$ $\dot{w}_{23}$ $\dot{w}_{33}$

$\dot{w}_{44}$ $\hat{\dot{w}}$

Figure 6.33: Some of the quadratic correction terms for the SS_0 layup.

NONLINEAR ANALYSIS The nonlinear analysis is performed with Koiter's algorithm. Figure 6.33 shows some of the quadratic corrections used by the method. Together with the buckling modes shown in Fig.6.32 and the linear-elastic solution, they constitute the ROM constructed by Koiter's method. First, we perform a Koiter analysis including only the first buckling mode. The results are reported in Fig.6.34 where they are compared with the reference solution evaluated by the path following method. While the solution at point A is appropriate, an incorrect solution is obtained at point B. The improving correlation at point B between Koiter's solution and the path-following method for increasing buckling modes is shown in Fig.6.35. Figure 6.36 shows how the solution at point A improves with the first two buckling modes. When the first six modes are included, the solution is practically coincident with that obtained from the path following method. Further increasing the number of modes does not produce a noticeable effect, as shown in Fig.6.37 for points A and C. Figure 6.38 shows how the variables of the ROM change when the load increases.

In Fig.6.39 the solution obtained with Koiter's method including six buckling modes is compared with the solution provided by two path following analyses. The first one is performed on the same model used for Koiter analysis, while the second is obtained using a very fine mesh of shell FE S4R in ABAQUS. Very good agreement between them can be observed.

Finally, deformed shapes at two load levels are reported in Fig.6.40. They are obtained by three Koiter analyses, using one, two and six modes. They confirm that the solution is not correctly captured with one buckling mode, whilst using two modes provides good results over the whole domain. Additionally, the postbuckled out-of-plane displacement is in agreement with that measured from Digital Image Correlation in the buckled region of the wingbox, as shown in Fig.20 and 21 of the work by Zucco et al.[126].

6.4.2.4 *Optimisation*

The proposed optimisation cases are as follows:

- Case A: in the spar web, the fibre angle is constant and then the number of variables is four. With reference to Table 6.10, $\vartheta_5 = \theta_2$, $\vartheta_6 = \theta_3$;
- Case B: the problem has six variables active and the displacement limit is reduced, assuming $w_{\mathrm{lim}} = 0.8 \cdot w_{\mathrm{QI},max}$;
- Case C: we look for a solution that allows weight to be reduced whilst respecting all constraints.

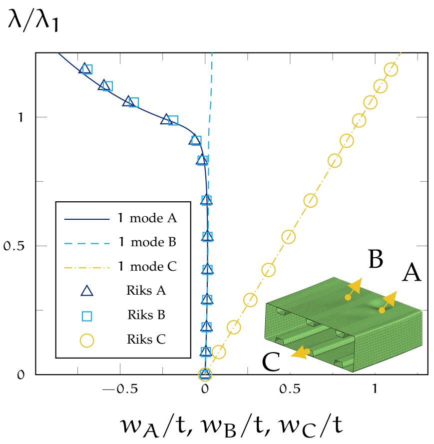

Figure 6.34: Equilibrium paths for the layup SS_0 with one mode Koiter.

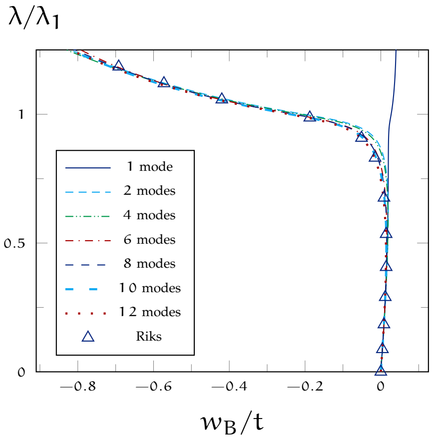

Figure 6.35: Equilibrium paths at point B for the layup SS_0 using from 1 to 12 buckling modes.

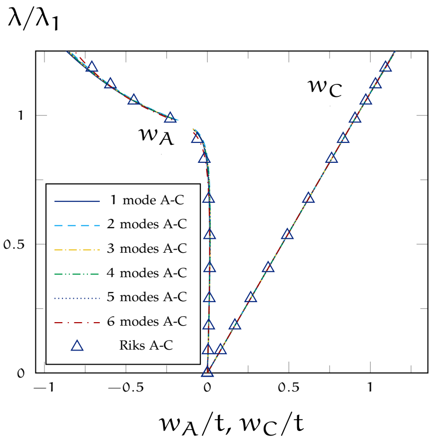

Figure 6.36: Equilibrium paths for the layup SS_0 using from 1 to 6 buckling modes.

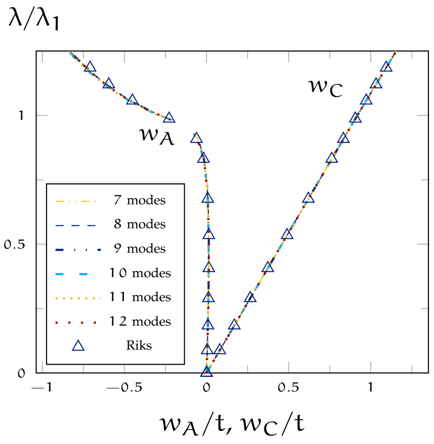

Figure 6.37: Equilibrium paths for the layup SS_0 using from 7 to 12 buckling modes.

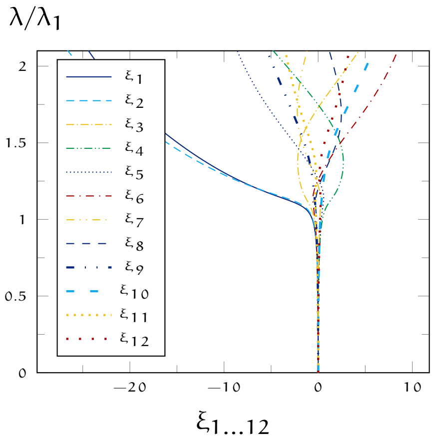

Figure 6.38: Variables of the ROM with the first 12 buckling modes for the layup SS_0 .

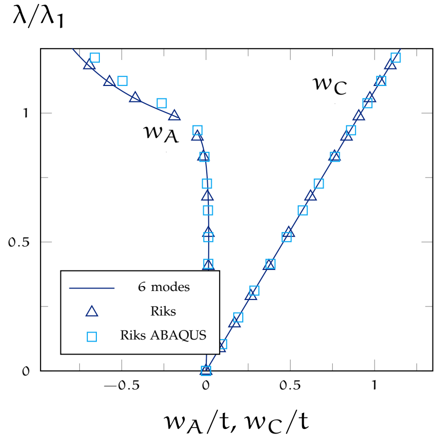

Figure 6.39: Comparison between the solution provided by Koiter's method and the path following analysis using the solid shell FE and the S4R shell element of ABAQUS, layup SS_0 .

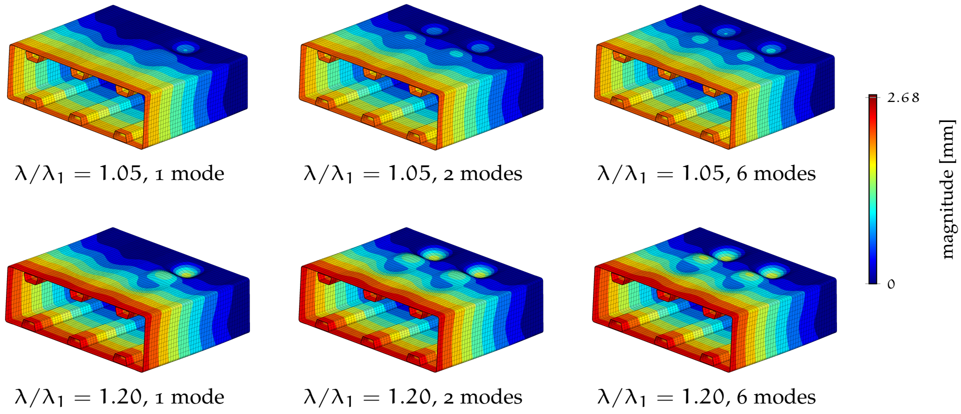
$\lambda/\lambda_1 = 1.05$, 1 mode
$\lambda/\lambda_1 = 1.05$, 2 modes
$\lambda/\lambda_1 = 1.05$, 6 modes
$\lambda/\lambda_1 = 1.20$, 1 mode
$\lambda/\lambda_1 = 1.20$, 2 modes
$\lambda/\lambda_1 = 1.20$, 6 modes

Figure 6.40: Magnitude of the displacement field for the layup SS_0 at $\lambda = 1.05$ and $\lambda = 1.20$ employing the first 1,2 and 6 buckling modes.

Table 6.12: Parameters of MCA.

property	symbol	value	
		set 1	set 2
initial population	N_1	400	800
zoom population	N_2	8	10
initial elite	n_1	20	30
elite during zooms	n_2	5	5
zooms	N_z	6	10
first zoom radius	R_1	8	10
zoom radius	R_2	4	6

To make the optimisation process less time consuming, a coarser mesh than the one used in section 6.4.2.1 is employed. The results of the optimal solutions are then compared with those obtained with the fine mesh. In Koiter's method, the buckling modes are selected as those corresponding to critical loads that do not exceed 1.3 times the lowest one. This criterion, which is analogous to that employed in the optimisation strategy proposed previously, is chosen on the basis of the results of section 6.4.2.3 regarding the SS_0 layup. The validity of this assumption for the optimal solutions is verified by comparing the equilibrium paths obtained using Koiter's algorithm with those traced using path-following analyses. In the following, the results for all three cases are presented.

6.4.2.5 *Case A*

First, optimisation is carried out with MCA using the parameter set no.1, as defined in Table 6.12. The optimal layup is denoted by $SS_{A,MCA}$. To assess the convergence of MCA, the analysis is repeated using parameter set no.2 of Table 6.12. Then, the problem is solved using GA, obtaining the optimal layup denoted by $SS_{A,GA}$. The population has 40 individuals and the crossover fraction of each generation in 0.7. The optimal fibre paths and objective function values are shown in Table 6.13. It is possible to observe that $w_{c,max}$ remains the same, whilst the value of the optimisation variables slightly changes.

The equilibrium paths for different layups are shown in Fig.6.41. They are plotted at the point where displacement $w_{c,max}$ is a maximum, and at point C. In addition, in Fig.6.42 the equilibrium path of $SS_{A,GA}$ is compared with those obtained by an arc-length method and with the finer mesh, obtaining good agreement.

Table 6.13: Stacking sequences $SS_{A,GA}$ and $SS_{A,MCA}$ and objective function values.

	Skin bay	Spar web	$w_{c,max}$
$SS_{A,GA}$	$90/[(0\pm\langle 53\vert 34\rangle)/0/(0\pm\langle 86\vert 77\rangle)]_S$	$90/[(0\pm 34)/0_3/(0\pm 77)]_S$	0.20
$SS_{A,MCA}$	$90/[(0\mp\langle 52\vert 34\rangle)/0/(0\pm\langle 87\vert 77\rangle)]_S$	$90/[(0\mp 34)/0_3/(0\pm 77)]_S$	0.20
$SS_{A,MCA}$ (2)	$90/[(0\pm\langle 53\vert 34\rangle)/0/(0\mp\langle 90\vert 77\rangle)]_S$	$90/[(0\pm 37)/0_3/(0\mp 77)]_S$	0.20

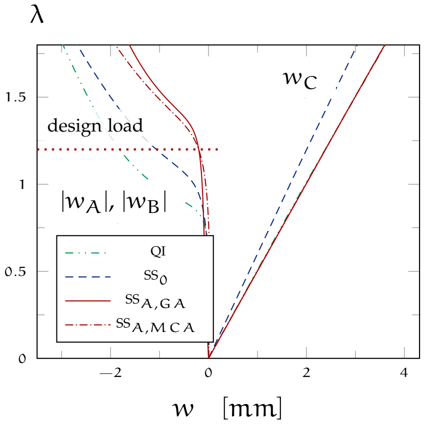

Figure 6.41: Equilibrium paths of the optimised structures of case A.

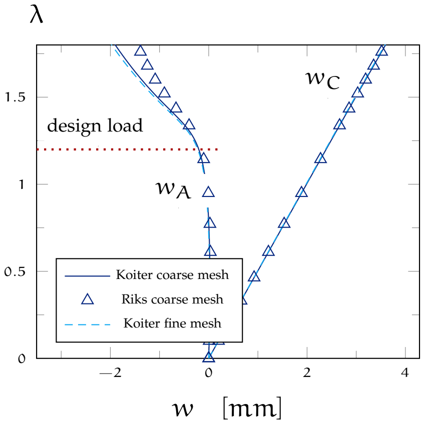

Figure 6.42: Solution obtained with Koiter's method and the mesh used during the optimisation process and layup $SS_{A,MCA}$ compared with that obtained with a path following analysis and with Koiter's algorithm using a finer discretisation.

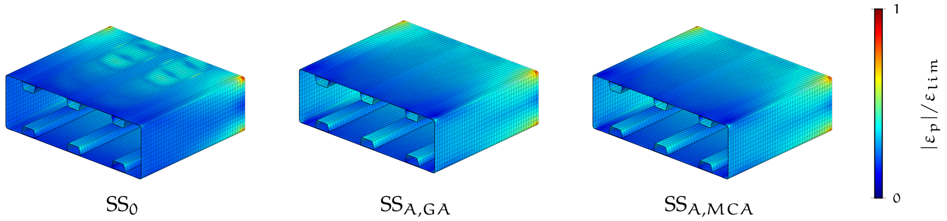

Figure 6.43: Maximum principal strains normalised for the limit strain of $2500\mu\epsilon$ at $\lambda = 1.2$ for the initial and optimised layups, case A.

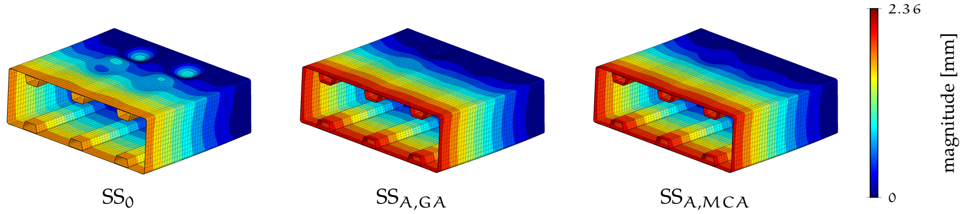

Figure 6.44: Displacement field at $\lambda = 1.2$ for the initial and optimised layups.

Figure 6.43 shows the map of the principal strains at the design load. They are normalised with respect to the strain limit. The optimised structures have a more uniform distribution of the strains and the maximum value is lower. In particular, the ratio between the maximum principal strain $|\varepsilon_p|$ and the limit strain ε_{lim} is 0.93 for the initial configuration and 0.90 for the optimised ones. Additionally, Fig.6.44 shows the deformed configurations at the design load. The layup SS_0 is globally stiffer than the optimised ones, even though in $SS_{A,GA}$ and $SS_{C,MCA}$ almost no buckling phenomena can be observed. Finally, Fig.6.45 shows the convergence of the two algorithms. It highlights how the minimum of the objective function changes with increasing function evaluations. In particular, the methods converge to a similar minimum values but, for the problem under consideration and analysis setups, the MCA provides a good estimate with fewer objective function evaluations. In the next paragraph, we show how the results of the optimisation are influenced by the steering radius.

INFLUENCE OF THE STEERING RADIUS Manufacturing VAT laminates with small steering radii can be a challenging task. In fact, this increases the probability of defects and the gap-overlap effect [107] and, as a consequence, the actual structure can have a different behaviour with respect to the design model if those

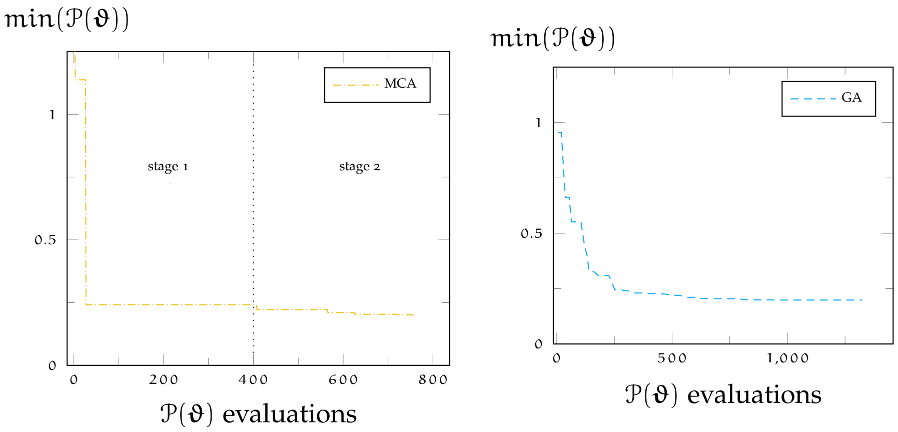

Figure 6.45: Convergence of MCA (left), and of GA (right), case A.

imperfections are not taken into account. We now show the influence of different steering radius constraints on the optimised structures. The optimisation process is repeated for different limiting radii. MCA is employed with parameter set no.1 from Table 6.12. The same limit is imposed on all VAT layers. In Table 6.14, the results of these analyses are presented. We show, for each optimised structure with a different minimum radius limit, the stacking sequence of the VAT panels, the actual radii, the value of the objective function and the smallest buckling load. The variation of the optimised displacement with the value of the maximum steering radius is plotted in Fig.6.46. The results highlight the possibility of considerably enhancing the postbuckling performance by decreasing the VAT steering radius. For example, the steering radius of $200\mathrm{mm}$ leads to a 5.7% higher buckling load and 24.7% decrease in out-of-plane displacement than for a steering radius of $400\mathrm{mm}$.

6.4.2.6 *Case B*

The results of case A show how the optimised layups improve the buckling performances yet reduces the global stiffness. To increase the mean stiffness related to the deflection of the end section, a smaller limit displacement is employed, namely $w_{\mathrm{lim}} = 0.8 \cdot w_{\mathrm{QI,max}}$.

The number of optimisation variables is greater in this case, with a commensurately larger population being used. In particular, a population of 80 individuals is used to optimise the structure using GA and the solution obtained

Table 6.14: Results of the optimisation problem of case A with different limiting steering radii. $SS_{2,3}$ and $SS_{5,6}$ denote the layup of the $2nd$, 3rd and of the $5th$, $6th$ layer of the skin, respectively, while with $R_{2,3}$ and $R_{5,6}$ the relative steering radii.

R_{lim}	200	400	600	800	1000	∞
$SS_{2,3}$	$0 \pm \langle 64 \vert 26 \rangle$	$0 \mp \langle 52 \vert 34 \rangle$	$0 \pm \langle 53 \vert 41 \rangle$	$0 \pm \langle 51 \vert 42 \rangle$	$0 \pm \langle 52 \vert 44 \rangle$	± 46
$SS_{5,6}$	$0 \pm \langle 88 \vert 71 \rangle$	$0 \pm \langle 87 \vert 77 \rangle$	± 76	$0 \pm \langle 76 \vert 74 \rangle$	$0 \pm \langle 76 \vert 73 \rangle$	± 73
$R_{2,3}$	201	433	605	812	1011	∞
$R_{5,6}$	385	536	∞	3322	2220	∞
$w_{C,max}$	0.1520	0.2018	0.2461	0.2520	0.2602	0.3256
λ_1	1.5307	1.4486	1.4135	1.3919	1.3876	1.3435

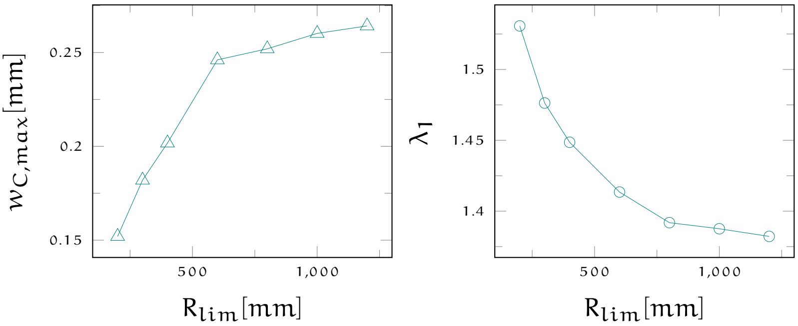

Figure 6.46: Optimised displacement and buckling load for different values of the maximum steering radius, case A.

Table 6.15: Stacking sequences $SS_{B,GA}$ and $SS_{B,MCA}$ and objective function values.

case	part	value
$SS_{B,GA}$	Skin bay	$90/[(0 \pm \langle 57\|53 \rangle)/0/(0 \mp \langle 42\|13 \rangle)]_S$
	Skin	$90/[\pm 53/0/\mp 13]_S$
	Spar web	$90/[(0 \pm \langle 40\|53 \rangle)/0_3/(0 \mp \langle 47\|13 \rangle)]_S$
	$w_{c,max}$	0.44
$SS_{B,MCA}$	Skin bay	$90/[(0 \mp \langle 59\|51 \rangle)/0/(0 \pm \langle 42\|15 \rangle)]_S$
	Skin	$90/[\mp 51/0/\pm 15]_S$
	Spar web	$90/[(0 \mp \langle 41\|51 \rangle)/0_3/(0 \pm \langle 46\|15 \rangle)]_S$
	$w_{c,max}$	0.45

Table 6.16: Buckling loads for the stacking sequence $SS_{C,MCA}$.

mode	1	2	3	4	5	6	7	8
λ	1.1922	1.1977	1.2420	1.2465	1.2627	1.2705	1.4629	1.4677

is identified as $SS_{B,GA}$. MCA uses parameter set no.2, as defined in Table 6.12, and the solution provided is labelled $SS_{B,MCA}$. The stacking sequences and the displacement $w_{c,max}$ are reported in Table 6.15. A graphical representation of a VAT layer of $SS_{B,GA}$ is given in Fig.6.47.

The results obtained in terms of equilibrium paths are reported in Fig.6.48. With respect to the previously obtained layups, we obtain stiffer structures, even if the buckling performances get slightly worst. Anyway, the postbuckling slope for $SS_{B,GA}$ and $SS_{B,MCA}$ is relatively high.

Figure 6.49 shows the deformed configurations. It confirms that the solution is the stiffest globally, even if the out-of-plane displacements due to buckling are bigger than in case A. On the other hand, the strains of $SS_{B,GA}$ are smaller than $SS_{A,GA}$, as shown in Fig.6.50. In particular, the maximum principal strain normalised for the limit strain ($|\varepsilon_p|/\varepsilon_{lim}$) is 0.93 for the initial configuration SS_0 , 0.90 for $SS_{A,MCA}$ and 0.83 for $SS_{B,GA}$.

6.4.2.7 *Case C*

The spar web, having 15 layers, is thicker than the skin (13 layers). We now find an optimised solution considering a uniform thickness, with 13 layers for both skin and spar web. In this way, the weight saving is 6.48%. In fact, the initial skin cross-sectional area is $4537 mm^2$, the cross-sectional area of the stiffeners is $2701 mm^2$ while the reduced cross-sectional area of the skin is $4068 mm^2$. The stiffener is again not considered in the optimisation process.

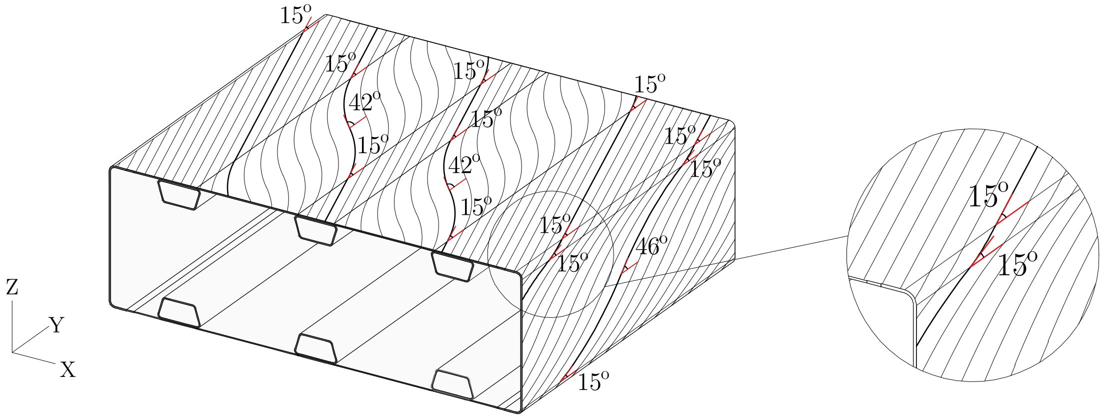

Figure 6.47: Representation of the 5th layer of $\mathrm{SS}_{B,GA}$, $(0\langle 42|15\rangle)$ on the skin and $(0\langle 46|15\rangle)$ on the spar web. The continuity of the fibre path between the skin and the spar web is highlighted in the magnified detail.

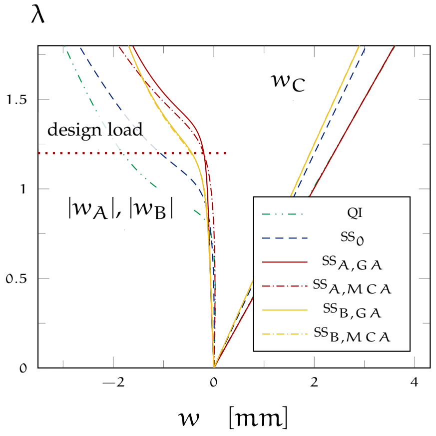

Figure 6.48: Equilibrium paths of the optimised structures.

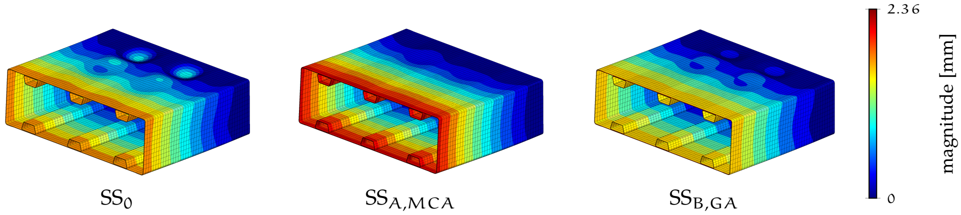

Figure 6.49: Displacement field at $\lambda = 1.2$ for the initial and optimised layups.

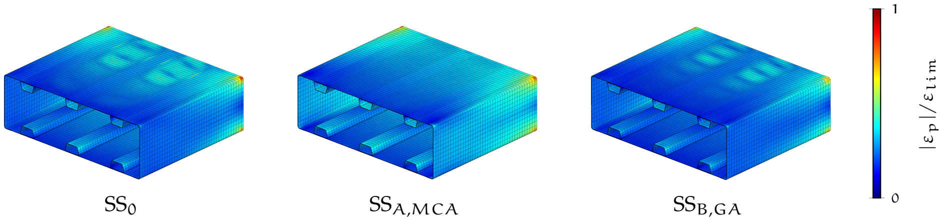

Figure 6.50: Maximum principal strains normalised for the limit strain of 2500$\mu\epsilon$ at $\lambda = 1.2$ for the initial and optimised layups.

The optimal layup provided by MCA is identified as $SS_{C,MCA}$, while that obtained using GA is labelled $SS_{C,GA}$. The results obtained are reported in Table 6.17. In particular, MCA furnishes an improvement of 29% on the out-of-plane displacement and of 4% of on the first buckling load.

Eight buckling modes have been used in the analysis of $SS_{C,MCA}$. Their values are reported in Table 6.16 while Fig.6.54 shows the first three of them. Figure 6.51 shows equilibrium paths of the optimised structure and compares it with the previously found optimised solutions. In this case, the importance of a multimodal algorithm is more evident. This is shown by the curves in Fig.6.52, in which the modal interaction is represented by very similar values assumed by the modal amplitudes of the ROM at the same value of the load. Figure 6.53 shows the strains and the deformed shape at the design load. It also shows the good agreement between the deformed shapes obtained with Koiter's method and the standard path-following analysis.

6.4.2.8 *Comments on the results of the optimisation*

In this section we have shown the results of the optimisation process obtained with different scenarios. The best improvement in out-of-plane postbuckling

Table 6.17: Stacking sequences and objective function values for case C.

case	part	value
$SS_{C,MCA}$	Skin bay	$90/[(0 \pm \langle 57\|66\rangle)/0/(0 \pm \langle 48\|26\rangle)]_S$
	Skin	$90/[\pm 66/0/\pm 26]_S$
	Spar web	$90/[(0 \pm \langle 63\|66\rangle)/0/(0 \pm \langle 53\|26\rangle)]_S$
	$w_{c,max}$	0.75
$SS_{C,GA}$	Skin bay	$90/[(0 \mp \langle 56\|69\rangle)/0/(0 \mp \langle 46\|24\rangle)]_S$
	Skin	$90/[\mp 69/0/\mp 24]_S$
	Spar web	$90/[(0 \mp \langle 53\|69\rangle)/0/(0 \mp \langle 41\|24\rangle)]_S$
	$w_{c,max}$	0.77

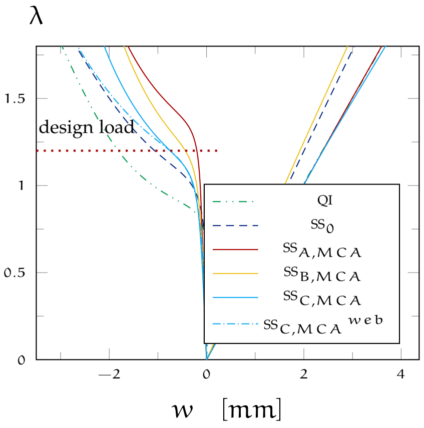

Figure 6.51: Equilibrium paths of the optimised structures.

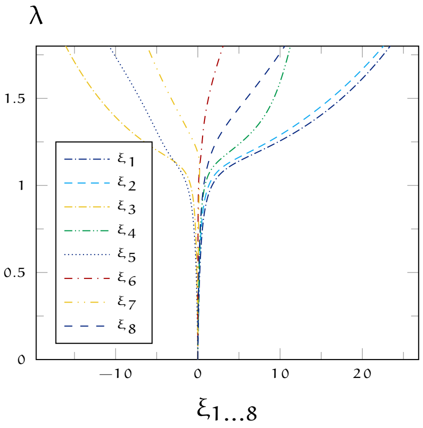

Figure 6.52: Variables of the ROM for the layup $SS_{C,MCA}$.

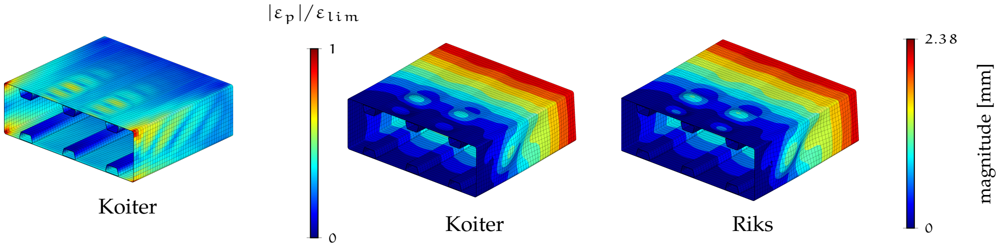

Figure 6.53: Maximum principal strain normalised with respect to the limit strain on the left and deformed configuration on the right, solution $SS_{C,MCA}$ and load level $\lambda = 1.2$. The wingbox is rotated by 180° with respect to the global Z to show the buckling on the spar web.

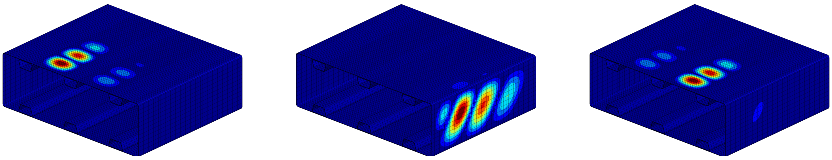

mode 1 mode 2 mode 3

Figure 6.54: First three buckling modes for the solution $SS_{C,MCA}$ .The wingbox is rotated by 180° with respect to the global Z to show the buckling on the spar web.

Table 6.18: Results of the initial and optimised configurations: out-of-plane displacement, first buckling load, maximum tip deflection and area. The improvements are evaluated with respect to SS_0 .

	initial		optimised			improvements		
property	QI	SS_0	case A	case B	case C	case A	case B	case C
$w_{C,max}\,[mm]$	1.82	1.07	0.20	0.44	0.75	81.31%	58.88%	29.91%
λ_1	0.93	1.15	1.45	1.31	1.19	25.97%	13.91 %	3.48%
$w_{max}\,[mm]$	2.38	2.00	2.36	1.89	2.38	-17.79%	5.67%	-18.71%
area $[mm^2]$	4537	4537	4537	4537	4068	-	-	6.48%

displacement is achieved in case *A*. However, the maximum tip displacement slightly increases, even if it remains under the design limit. In case *B* we obtain the globally stiffest solution and, in addition, notable improvements in the buckling and postbuckling performances. Finally, case *C* highlights the possibility of obtaining a lighter wingbox together with an improved performance in the buckling and postbuckling regime. Table 6.18 summarises the results obtained for the three analysed cases.

6.4.3 Lamination parameters

Hereafter, two numerical examples are analysed using lamination parameters as intermediate variables, according to the approach presented in 6.3. The first test regards a cylindrical panel in compression, with an unstable postbuckling and imperfection sensitive behaviour. The second one is a well-behaved full-scale wingbox subject to shear and flexural moment. The two structures in the numerical examples behave differently and are able to show the potentiality of the proposed approach from two different perspectives. From one side, in fact, the analysis regards a structure with simple geometry but complex postbuckling behaviour, involving multimodal buckling and imperfection sensitivity. From the other side, the wingbox is characterised by a simpler structural behaviour, but high complexity in the geometry, constituted by many patches and stringer. Additionally, both the numerical examples have been already previously optimised by employing stochastic optimisers and this highlights the improvements achieved using lamination parameters. In all cases the baseline design is represented by a Quasi-Isotropic laminate (QI) obtained when all the lamination parameters are zero.

6.4.3.1 *Cylindrical panel under compression*

Figure 6.55 shows the simply-supported cylindrical panel under uniform axial compression that represents the first test proposed. The structure was previously object of postbuckling optimisation [103] using non-conventional straight fibre laminates and a stochastic optimiser. Additionally, it was taken as benchmark example to test the accuracy of the isogeometric model in chapter 4 [127].

STAGE 1 The optimisation regards finding the distribution of lamination parameters that maximise a collapse load defined as the minimum between the lowest limit load λ_{lim} and the load related to a design axial displacement of the loaded section $v_{ax} = v_d$. With reference to Eq.(6.14), it reads as

$$\mathcal{P}[\psi_d] = -\frac{\lambda_c}{\lambda_{qi}} = -\frac{\min(\lambda_{lim}, \lambda[v_d])}{\lambda_{qi}} \tag{6.24}$$

where the loads are normalised with respect to the first buckling load for the QI case λ_{qi}. Such a formulation of the objective function allows to look for the less imperfection-sensitive configuration or the axially-stiffest potential stable behaviour.

The overall thickness of the shell is $t = 10\,\mathrm{mm}$. The design axial displacement is $v_d = 2\,\mathrm{mm}$. Material properties are given in Table 6.19. The discrete model employs quadratic NURBS and a 9×9 control grid that guarantee convergence for a set of lamination parameters distributions. Consequently, the number of variables is 683. The geometrical imperfection is given in the direction of the buckling modes and its maximum amplitude is $\tilde{u}_x = 0.5t$.

Lamination parameters are described by using two different grids, 6×6 and 9×9 elements. Because of the symmetry of the problem, only the control points of a quarter of the structure are taken as independent variables, this leading to 4×4 and 6×6 design control points, respectively for the two discretisations.

Table 6.19: Cylindrical panel: elastic material coefficients.

$E_{11}[GPa]$	$E_{22}[GPa]$	ν_{12}	ν_{23}	$G_{12}[GPa]$	$G_{23}[GPa]$
30.6	8.7	0.29	0.5	3.24	2.9

A special-orthotropic laminate is adopted, characterised by a symmetric and balanced stacking sequence and with no flexural-torsion coupling effects. The number of optimisation variables is 64 and 144 respectively in the two cases.

Figure 6.56 shows the convergence of GCMMA for the two different meshes for lamination parameters. It is possible to note how convergence is reached for less than 10 iterations and how a good solution is achieved also for the coarser mesh. For the 9×9, Fig. 6.57 shows how the equilibrium path evolves during iterations. Interestingly, already in first iteration the solution significantly improves with respect to the baseline QI configuration and the third solution has a stable initial postbuckling. After that, the optimiser founds increasingly axially-stiffer solutions and a converged result is obtained quite soon.

The results of stage 1 are reported in Fig. 6.58 in terms of equilibrium paths. The equilibrium path for the optimal distribution of lamination parameters (LP) is compare with the baseline QI case. Additionally, comparison is also made with the optimal solution obtained using straight fibre laminates with a non-symmetric stacking sequence (SF) [103]. The fibre orientations of SF case are $[\mp 54, 0_4]$ and are measured from inside-out with respect to the cylindrical axis. For all the solutions provided by Koiter's method, comparison is made with the results of a path-following solution algorithm, denoted with *Riks* in Fig. 6.58, obtaining good agreement. The optimal distribution of lamination parameters is shown in Fig.6.59. The buckling modes for the optimal distribution of lamination parameters are pictured in Fig.6.61, while Fig.6.60 shows the worst case imperfection detected during the optimisation process.

STAGE 2 The potentiality of the 2-stages approach resides in the possibility of designing structures with many layers without increasing the computational cost of the overall process. Actually, having a high number of layers is an advantage for the procedure since the more the layers, the more accurate the match with the optimal solution in stage 1 will be. This is shown here, where stage 2 is repeated considering three symmetric and balanced laminates composed by nl equal to 4, 8 and 12 independent layers. The stacking sequence is $[\pm\vartheta_1, \dots, \pm\vartheta_{nl}]_s$ and each ϑ varies with a quadratic NURBS according to eq.(6.17) and over a grid of 9×9 elements.

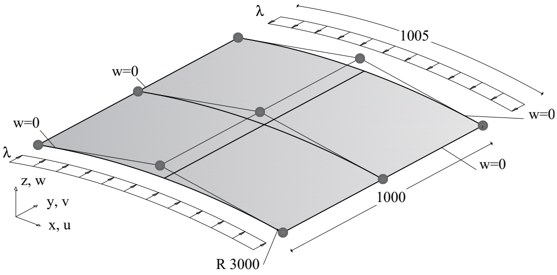

Figure 6.55: Cylindrical panel: geometry, NURBS control grid and loading and boundary conditions.

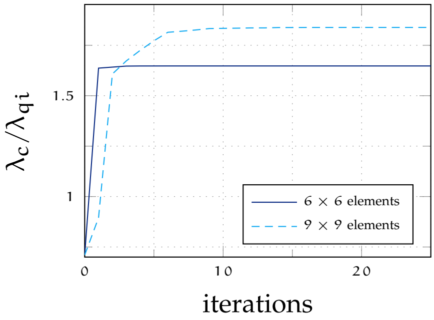

Figure 6.56: Cylindrical panel: convergence of GCMMA at the first optimisation stage for two different mesh grids of the NURBS interpolation for lamination parameters.

The solution of the problem in Eq.(6.18) is obtained with a multi-start GCMMA. The convergence of the algorithm is quite fast, as Fig. 6.62 shows although it is sensible to the initialisation. The convergence results for different starting points are reported in Fig. 6.63. When straight fibre (SF) laminates are employed as starting points, the convergence of the algorithm is faster than a VAT initialisation. The results in terms of equilibrium path are shown in Fig. 6.64, while Table 6.20 gives informations about the matching between the values of objective function and the first buckling loads obtained using lamination parameters and with the retrieved fibre orientations with increasing number of layers. The retrieved fibre orientations are reported in Fig. 6.65 and in Fig. 6.66 for 4 and 8 independent layers, respectively.

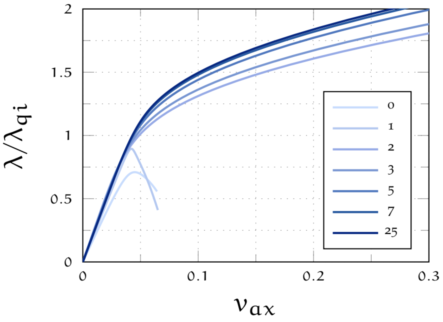

Figure 6.57: Cylindrical panel: equilibrium path for different iterations $(0, 1, \ldots 25)$ of GCMMA at the first optimisation stage and a grid of 9×9 control points. Displacement v_{ax} versus load control parameters λ normalised on λ_{qi}.

Table 6.20: Cylindrical panel: results of the optimised configuration LP using a grid of 6×6 and 9×9 control points for the lamination parameters. The second level optimisation is repeated increasing the number of layers showing how the matching $((1 - \mathcal{E})\%$ of Eq.(6.18)) with the results of the first level optimisation improves.

	9×9					
case	$\mathcal{P}$	λ_1	λ_2	λ_3	λ_4	match
QI	0.710	1.000	1.255	1.795	1.883	-
optimum LP	1.830	1.177	1.489	1.840	2.100	-
4 layers	1.800	1.156	1.493	1.837	2.155	98.29%
8 layers	1.811	1.167	1.479	1.837	2.099	99.78%
12 layers	1.821	1.170	1.482	1.840	2.097	99.92%

6.4.3.2 *Full-scale wingbox*

The optimal design of full-scale structures into the postbuckling range is not a simple task because of the time-consuming procedure usually required. This test regards a concept wingbox that has represented a demonstrator recently manufactured and tested at University of Limerick [18]. It is presented to show the possibility of applying the proposed approach to the optimal design of a full-scale structure, overcoming many difficulties of the approaches available in literature.

The starting point is a reference design obtained using the approach proposed in section 6.4.2 which is based on linear variation of the fibre orientations and stochastic optimisers. Successively, the wingbox is optimised using the proposed

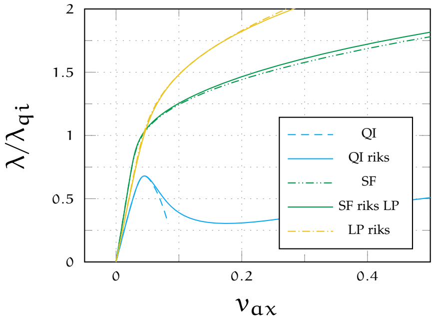

Figure 6.58: Cylindrical panel: path-following (Riks) vs Koiter solutions for the baseline and optimised shell panels after first optimisation stage. Displacement u at point $\cdots$ versus load control parameters λ normalized on λ_{qi}, for different material configuration: quasi-isotropic QI, optimised lamination parameters LP, optimised straight fibre.

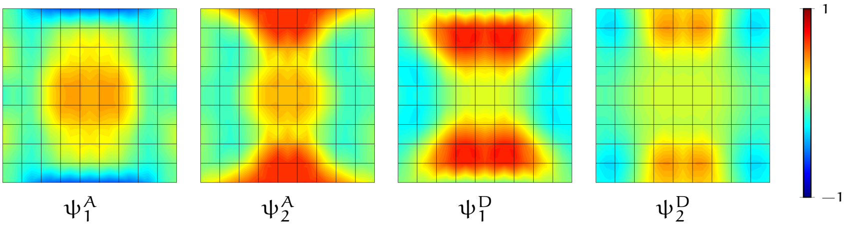

Figure 6.59: Cylindrical panel: distribution of lamination parameters for the optimal configuration LP.

two-stages approach. Two different expressions of the objective function to optimise the post-buckling regime are proposed. The first one, denoted in the following with case 1, is analogous to that already proposed, and is aimed at minimising the maximum postbuckled displacement at a design load level, namely

$$\mathcal{P}[\boldsymbol{\psi}_d] = u_{pb} = ||\mathbf{d}[\mathbf{X}, \lambda_d] - \lambda_d \hat{\mathbf{d}}[\mathbf{X}]||_\infty \tag{6.25}$$

where λ_d is a design load level chosen to be 2.5, $\mathbf{u}$ is the displacement field and $\hat{\mathbf{u}}$ is the linear elastic solution.

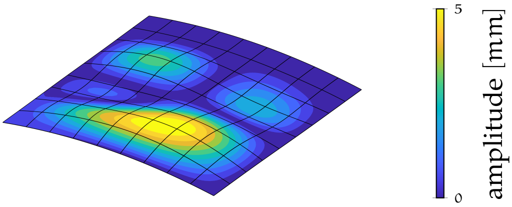

Figure 6.60: Cylindrical panel: worst geometrical imperfection case obtained for the optimal lamination parameters configuration LP.

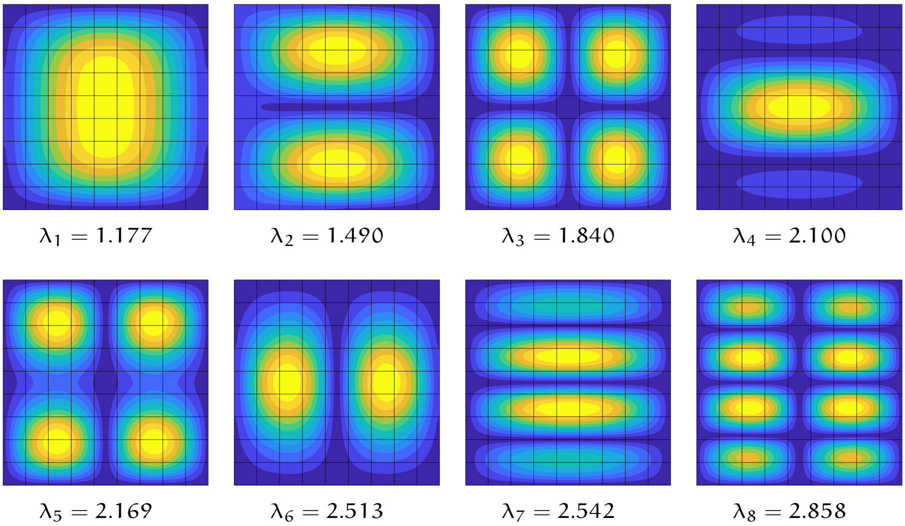

Figure 6.61: Cylindrical panel: first eight buckling modes $\dot{v}_i$ and corresponding buckling load λ_i used in Koiter analysis for the optimal lamination parameters case LP.

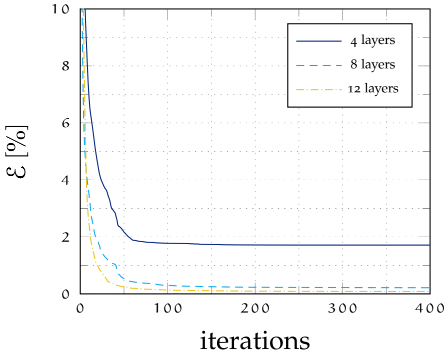

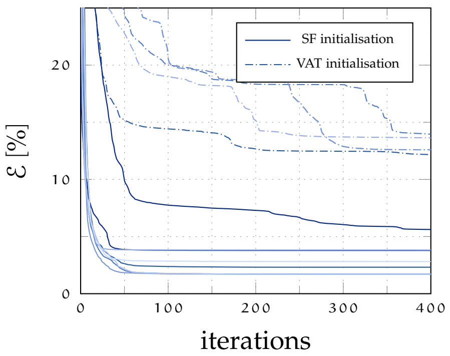

Figure 6.62: Cylindrical panel: convergence of multi-start GCMMA at the second optimisation stage. It is shown the result relative to the best initialisation for each analysed case.

Figure 6.63: Cylindrical panel: convergence of GCMMA for different starting points for the case with 4 independent layers. The convergence is good if a straight fibre (SF) initialisation is adopted, while it is difficult for all the VAT initialisations.

Conversely, in case 2 it is searched for a solution that minimises the average postbuckled displacement and the objective function is defined as

$$\mathcal{P}[\psi_d] = \Phi_{pb} = \left(\mathbf{d}_g[\lambda_d] - \lambda_d \hat{\mathbf{d}}_g\right)^T \mathbf{K}_{QI} \left(\mathbf{d}[\lambda_d] - \lambda_d \hat{\mathbf{d}}_g\right) \tag{6.26}$$

where $\mathbf{K}_{QI}$ is the linear tangent matrix evaluated for a QI case obtained with all the lamination parameters equal to zero and $\hat{\mathbf{d}}_g$ is the displacement part of the linear solution.

The maximum imperfection amplitude used during the optimisation process is $1/50$ of the skin thickness.

The optimisation concerns skin and spar web only, while the stiffener's layup is kept constant to $[90/45/0_2/-45/0]_S$. The variable stiffness laminate is designed only over the skin, while the spar web is designed as a straight fibre laminate. Anyway, continuity of the lamination parameters is guaranteed along the corners between skin and spar web. The material is supposed to be specially-orthotropic such that four lamination parameters can describe the stiffness matrix.

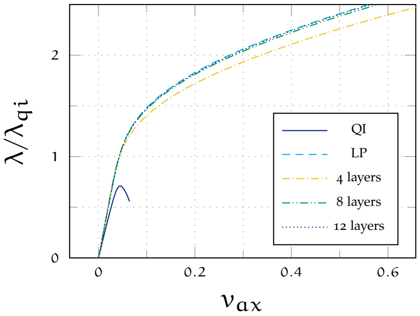

Figure 6.64: Cylindrical panel: equilibrium paths of the axial displacement for the baseline and optimised solutions after second stage optimisation. Displacement v of the loaded section versus normalised load control parameter λ, for different material configuration: quasi isostropic QI, optimised lamination parameters LP, retrieved layers.

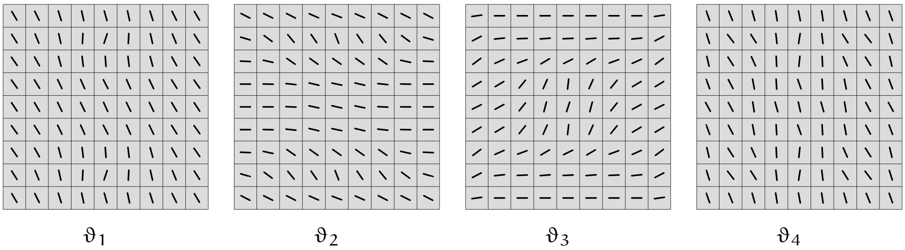

Figure 6.65: Cylindrical panel: fibre orientations obtained from the second optimisation level for the stacking sequence $[\pm\vartheta_1, \pm\vartheta_2, \pm\vartheta_3, \pm\vartheta_4]_S$.

LINEAR-VARIATION OF FIBRE ORIENTATIONS The postbuckling optimisation is performed using the approach presented in section 6.4.2 to have a reference solution. The optimisation is based on a fibre path parameterisation according to Gürdal and Olmedo [92] and the parametric stacking sequence is reported in Table 6.22. The optimisation furnishes as optimal fibre orientations the values $\vartheta = [-69.65, -20.66, 90.00, 3.59]$, while the optimal value of objective function in Eq. (6.25) is 2.42 mm.

STAGE 1 The optimal distribution of the lamination parameters is obtained using the proposed strategy for the two cases. Lamination parameters are described over the skin by quadratic NURBS interpolation controlled by 81

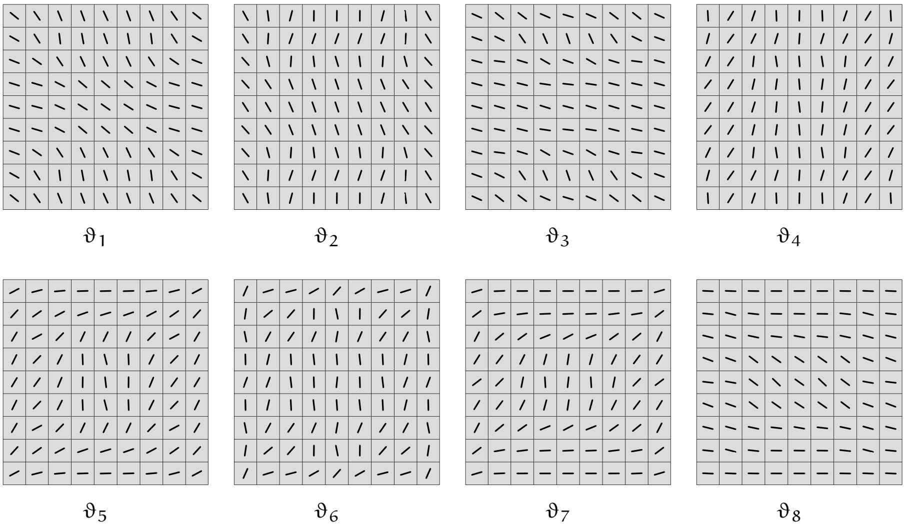
ϑ_1 ϑ_2 ϑ_3 ϑ_4

ϑ_5 ϑ_6 ϑ_7 ϑ_8

Figure 6.66: Cylindrical panel: fibre orientations obtained from the second optimisation level for the stacking sequence $[\pm\vartheta_1, \pm\vartheta_2, \pm\vartheta_3, \pm\vartheta_4, \pm\vartheta_5, \pm\vartheta_6, \pm\vartheta_7, \pm\vartheta_8]_S$.

Table 6.21: Wingbox: elastic material coefficients.

$E_1[GPa]$	$E_2[GPa]$	$G_{12}[GPa]$	ν_{12}
135.00	7.54	5.00	0.30

Table 6.22: Wingbox: Parametric fibre paths used in the optimisation problem.

Part	stacking sequence
Skin bay	$[90/(0 \pm \langle\vartheta_1\vert\vartheta_2\rangle)/0/(0 \pm \langle\vartheta_4\vert\vartheta_3\rangle)]_S$
Skin	$[90/\pm\vartheta_2/0/\pm\vartheta_3]_S$
Stiffener	$[90/45/0_2/-45/0]_S$
Spar web	$[90/(0 \pm \langle\vartheta_5\vert\vartheta_2\rangle)/0_3/(0 \pm \langle\vartheta_6\vert\vartheta_3\rangle)]_S$

control points that lead to 324 optimisation variables. The stiffness distribution is constant along the edge between skin and spar-web while the top and bottom skin are constrained to be equal. Additionally, due to the symmetry in the loading condition, only a half of the skin is optimised.

Figure 6.67 the number of iterations of GCMMA versus the value of the objective function for the two cases, each one normalised on its optimal value. It is possible to note how the objective function in case 2 leads to a smoother optimisation space with positive consequences on the convergence of the minimisation problem. In Fig. 6.68 it is possible to note how the equilibrium paths evolve during the iterations. The results of stage 1 are reported in Table 6.23. It shows the values of the Φ_{pb} and u_{pb} and the two lowest buckling loads for the quasi-isotropic case, for the optimised solution using linear fibre orientations and for the optimal solutions of the two cases (LP case 1 and LP case 2). The corresponding equilibrium paths are plotted in Fig.6.69 for the displacement u_{pb}. Figures 6.70 and 6.71 show the optimal distributions of lamination parameters for case 1 and 2.

Table 6.23: Wingbox: convergence results for stage 1. Φ_{pb}, u_{pb}, first and second buckling mode λ_1, λ_2 for quasi isotropic QI, linear fibre variation LV, case 1 and case 2.

	Φ_{pb}	u_{pb}	λ_1	λ_2
QI	8.9837	4.9110	1.2494	1.2679
LV	1.7442	2.4213	2.0713	2.1078
case 1	1.6408	0.5815	2.576	2.6317
case 2	0.6441	0.7574	2.5907	2.6418

Comparison can be made between the optimal solutions found in case 1 and case 2. The two lowest buckling modes are represented in Fig.6.72 for the optimal solution of case 1 and in Fig. 6.73 for case 2. Additionally, Fig.6.74 compares the nonlinear part of the displacement between QI and optimised cases, while Fig. 6.75 shows the equilibrium paths in terms of Φ_{pb} and u_{pb}.

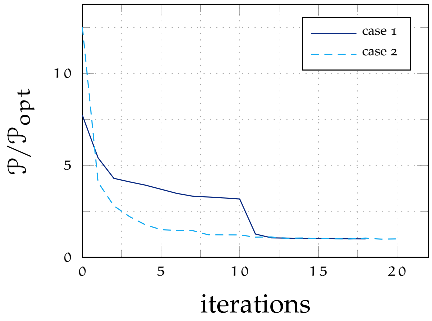

Figure 6.67: Wingbox: convergence of GCMMA at the stage 1. The number of iterations are plotted versus the value of the objective function for the two cases, each one normalised on its optimal value. It is possible to note how the convergence the formulation of the objective function in case 2 is faster.

STAGE 2: FIBRE ANGLE ORIENTATIONS In stage 2 a variable angle tow laminate is retrieved from the optimal distribution of lamination parameters. The stage is repeated for three different number of layers over the skin and the spar-web, namely $nl = 4, 8, 12$ independent layers. The stacking sequence is $[\pm\vartheta_1, \ldots, \pm\vartheta_{nl}]_s$ and each ϑ varies with a quadratic NURBS according to eq.(6.17). The solution of the optimisation problem of stage 2 is performed using GCMMA using as a starting point a quasi-isotropic straight fibre laminate. Table 6.24 collects the results from stage 2. The target results of stage 1 are compared with those obtained with the retrieved layups. The results with 12 independent layers give, as expected, the best correspondence in terms of maximum and average nonlinear displacement and in terms of buckling loads for both case 1 and 2. Also the results obtained with 8 layers closely match those of lamination parameters, while some differences can be observed with 4 independent layers. The distribution of fibre orientations over the skin is reported in Fig.6.76 for case 1 and in Fig.6.77 for case 2.

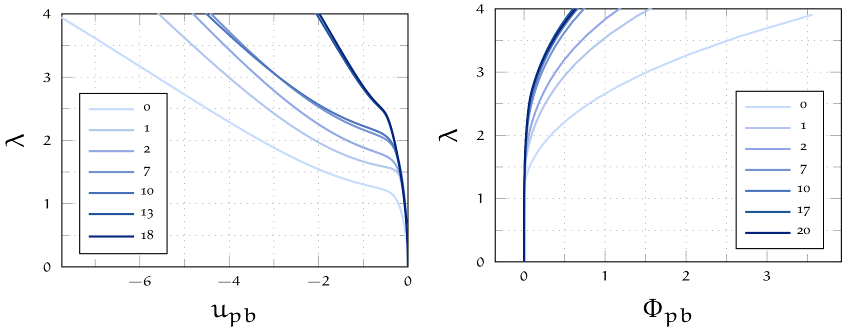

Figure 6.68: Wingbox: equilibrium path for different iterations of GCMMA relatively to case 1 (left) and case 2 (right).

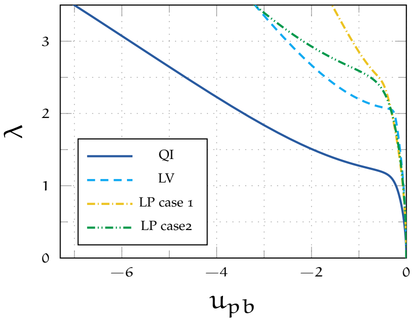

Figure 6.69: Wingbox: equilibrium path for the baseline structure QI, linear fiber variation LV, optimum lamination parameters LP (case 1 and 2). Displacement u_{pb} versus load control parameter λ.

Table 6.24: Wingbox: results of the optimisation from stage 2. The *match* value is $(1-\mathcal{E})\%$ and express the average correspondence between the lamination parameters obtained from fibre orientations and the optimal lamination parameters found in stage 1.

	case 1					case 2				
case	u_{pb}	Φ_{pb}	λ_1	λ_2	match	u	uKu	λ_1	λ_2	match
LP	0.5815	1.6408	2.576	2.6317	-	0.7574	0.6441	2.5907	2.6418	-
4 layers	0.9262	1.7637	2.4551	2.4958	98.21 %	1.1815	0.7902	2.4453	2.4904	98.59 %
8 layers	0.7700	1.7468	2.5088	2.5625	99.87 %	0.7995	0.6804	2.5472	2.5949	99.56%
12 layers	0.5829	1.6143	2.5734	2.6286	99.98 %	0.7517	0.6629	2.5854	2.6361	99.91 %

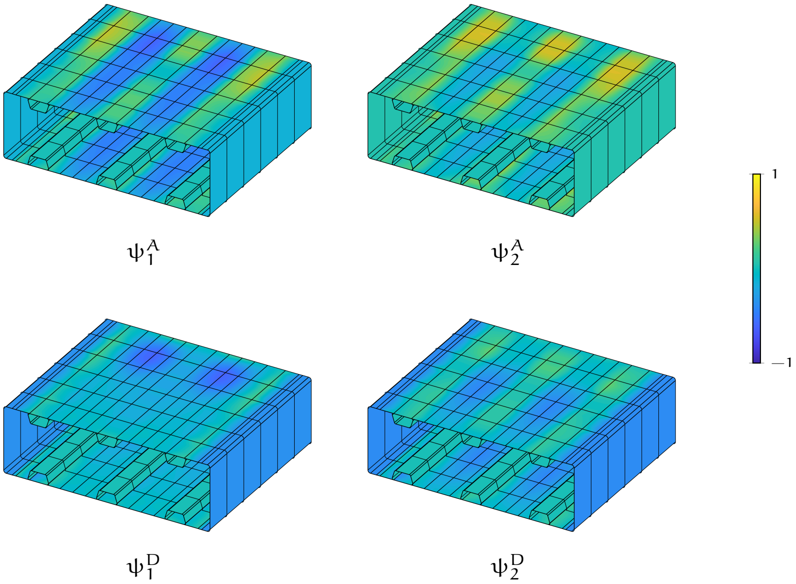

Figure 6.70: Wingbox: optimal distribution of lamination parameters over the domain for case 1.

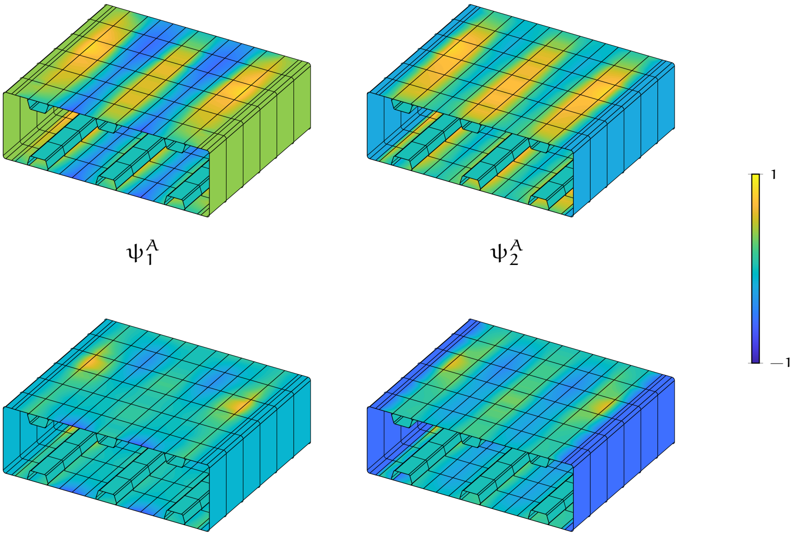

ψ_1^A ψ_2^A

ψ_1^D ψ_2^D

Figure 6.71: Wingbox: optimal distribution of lamination parameters over the domain for case 2.

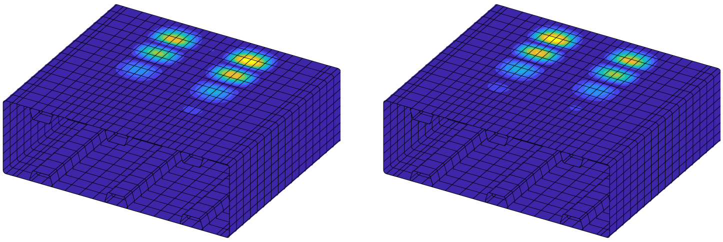

$\lambda_1 = 2.5760$ $\lambda_2 = 2.6317$

Figure 6.72: Wingbox: buckling modes for case 1.

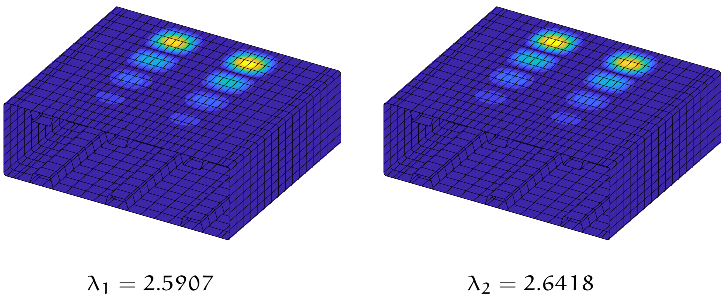

Figure 6.73: Wingbox: buckling modes for case 2.

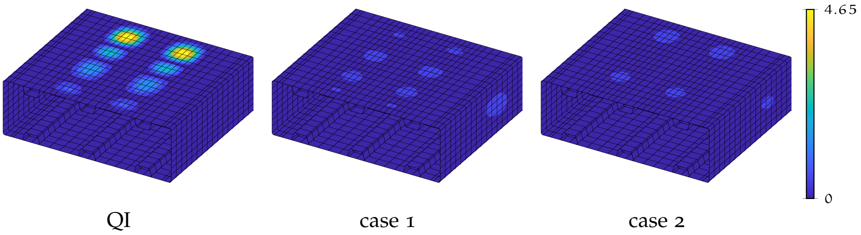

Figure 6.74: Wingbox: nonlinear component of the displacement $\mathbf{d}[\lambda_d] - \lambda_d \hat{\mathbf{d}}$ at design load for the baseline and optimised structures. We remind that $u_{pb} = ||\mathbf{d}[\lambda_d] - \lambda_d \hat{\mathbf{d}}||_\infty$.

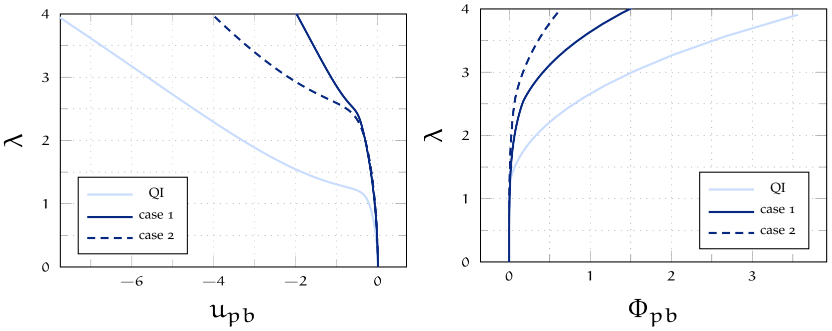

Figure 6.75: Wingbox: equilibrium path in terms of u_{pb} (left) and Φ_{pb} (right) for the baseline structure and the optimised solutions in case 1 and case 2.

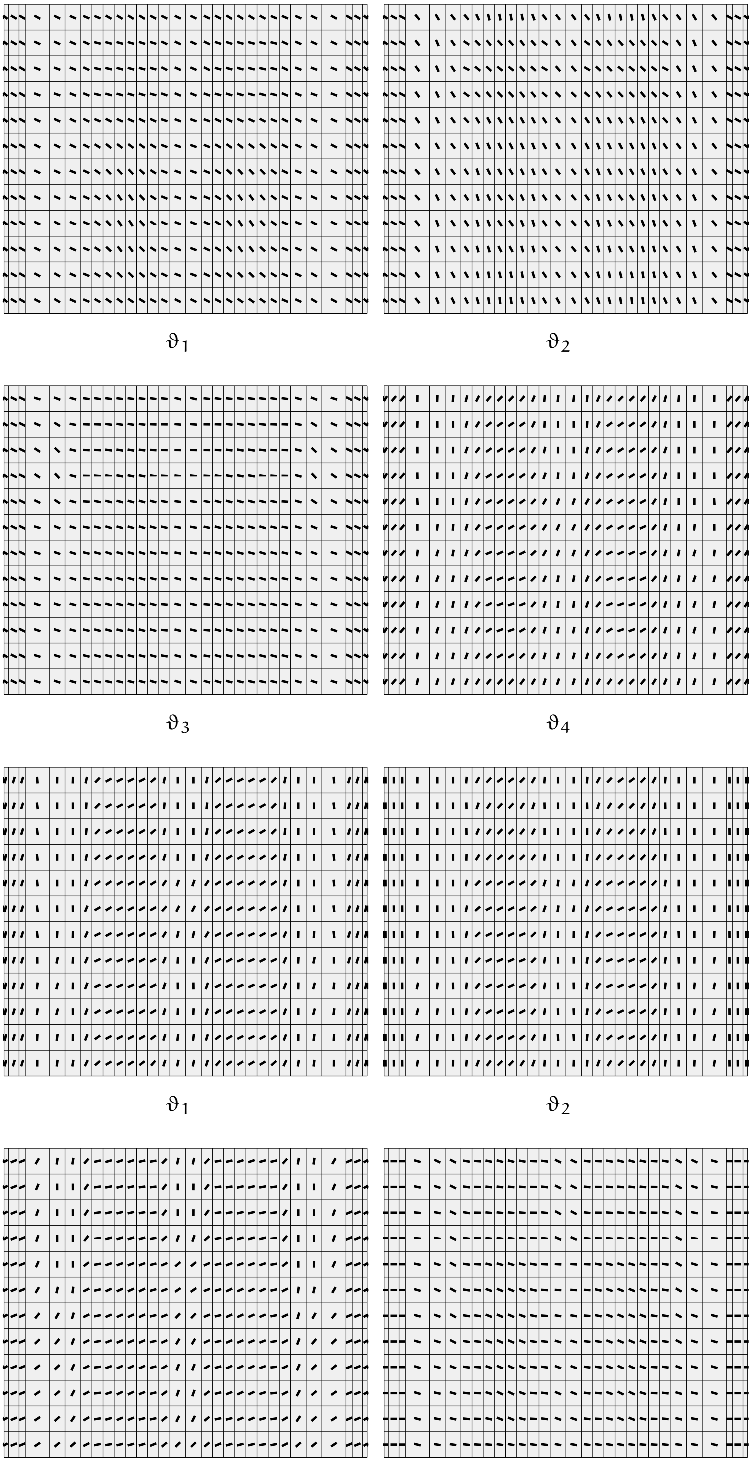

ϑ_1 ϑ_2

ϑ_3 ϑ_4

ϑ_1 ϑ_2

ϑ_3 ϑ_4

Figure 6.76: Wingbox: fibre orientations on the skin obtained from the second optimisation level of case 1 for the stacking sequence $[\pm\vartheta_1, \dots, \pm\vartheta_8]_S$.

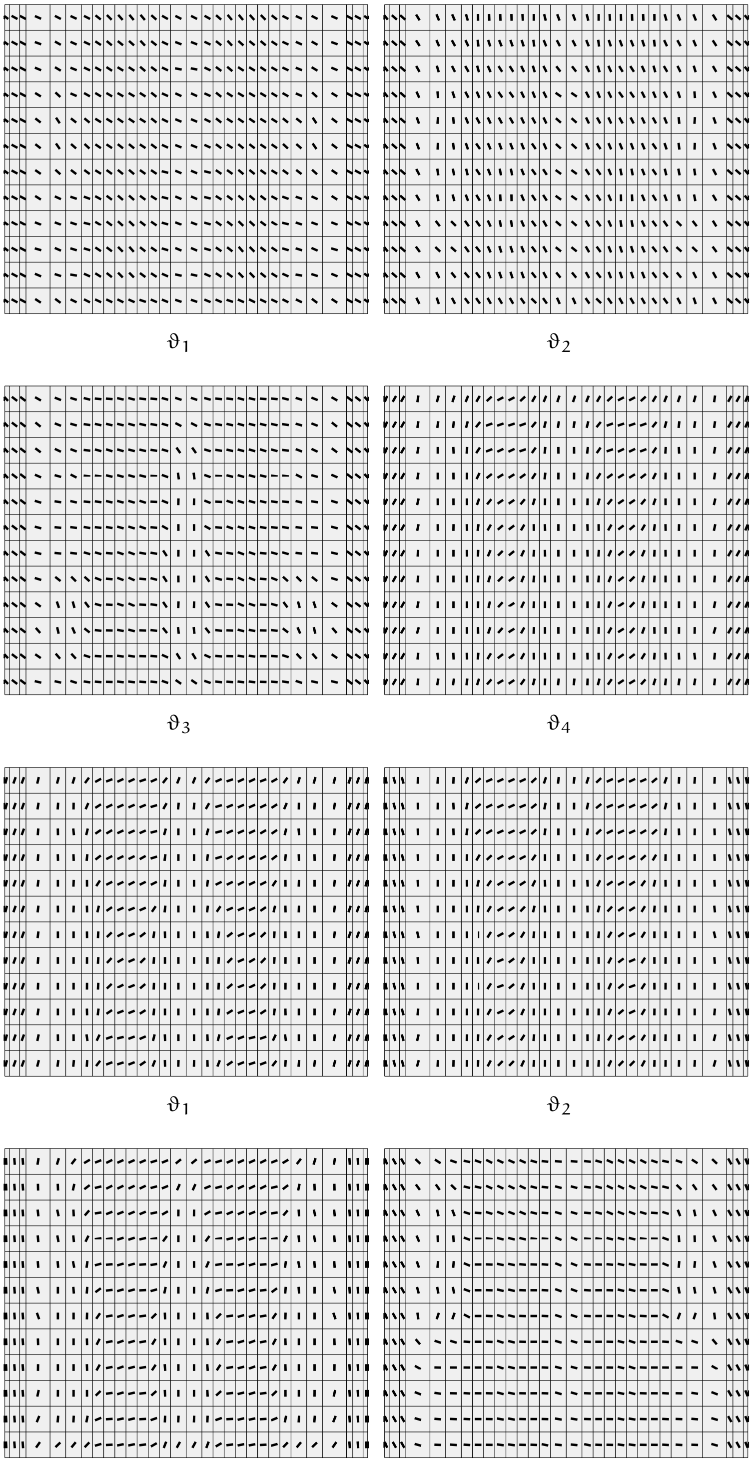

ϑ_1 ϑ_2

ϑ_3 ϑ_4

ϑ_1 ϑ_2

ϑ_3 ϑ_4

Figure 6.77: Wingbox: fibre orientations on the skin obtained from the second optimisation level of case 2 for the stacking sequence $[\pm\vartheta_1, \ldots, \pm\vartheta_8]_S$.

7 CONCLUSIONS

In this thesis we have faced the topic of the optimal design of imperfection sensitive composite shells. We have addressed the subject from different sides. The main purpose has been to propose a numerical tool able to deal with complex geometries and entangled postbuckling behaviour, accounting for the imperfection sensitivity that represents a phenomenon that can drastically deteriorate the structural performance of slender structures. In doing so, we had to keep in mind the features of efficiency and flexibility required by the approach in order that it can be used within optimisation strategies. Therefore, we have devised a solid-shell isogeometric model for the geometrically nonlinear analysis of elastic shells. It gives the chance to use a low number of variables with respect to standard finite elements by exploiting the high continuity of the NURBS interpolation functions. By using the solid-shell description, one can employ only displacement degrees of freedom without making use of finite rotations that complicates the treatment of geometrical nonlinearities in classical shell models. Patch-wise reduced integrations, previously proposed in a linear-elastic framework, have been successfully tested in the nonlinear context. Their use has the double benefit of solving the problem of interpolation locking, that reduces the performance of low-order NURBS especially when employed in large displacement problems, and of reducing the number of integration points thereby improving the overall efficiency. The resulting numerical formulation performs well in classical shell obstacle courses when compared to state-of-art tools.

Another aspect of paramount importance regards the algorithm used to solve the geometrically nonlinear set of equilibrium equations. Beside the standard arc-length method, we have investigated a reduced order model constructed using Koiter's method. The approach is an interesting alternative to path-following strategies and is based on the reduction in the number of unknowns by performing an asymptotic expansion of the equilibrium condition. In this way, it is possible to obtain an accurate estimate of the initial postbuckling response by reducing the number of variables from the degrees of freedom of the isogeometric model to a few tens, namely the number of the significant buckling modes. However, it has been shown in several works how nonlinear solution algorithms require a mixed formulation to guarantee robustness. Unfortunately, due to the high continuity of the displacement interpolation, mixed formulations that improve accuracy should be formulated at patch level, increasing the number of global variables. On the other side, locking phenomena are already eliminated by reduced integration, and we have obtained a satisfactory accuracy using the displacement-based formulation. For this reason, we have adopted a peculiar mixed format that considers as variables the stresses at the integration points. This choice gives the same accuracy of displacement formulation and allows us to easily eliminate the stresses by static condensation at the element level, preserving its efficiency.

Koiter's method has the additional advantage of allowing the effect of many geometrical imperfections to be evaluated at the computational cost of a single analysis. This is of primary importance because gives us the chance to detect the worst-case imperfection, namely the imperfection shape that provides the less safe result. However, the method available in literature is accurate only for small imperfection amplitude and linear prebuckling. Therefore, a new formula for accounting for the effect of geometrical imperfections in Koiter's analysis has been proposed. Numerical results have confirmed the efficacy of the proposed procedure that allows to coherently consider the effect of imperfections up to the second asymptotic order.

Finally, this work has focused on the postbuckling optimisation of variable angle tow composite structures. To this end, two strategy have been proposed, both using Koiter's method to efficiently evaluate the postbuckling response and account for the effect of imperfections. The first one is a random search method based on Monte Carlo algorithm. The second one, that gives improved performance when many layers are optimised, is based on lamination parameters. The isogeometric description used in the numerical model of the shell, is also used to describe the stiffness variation over the structure, thereby reducing the number of optimisation variables. The strategies have been applied for optimising different shell structures, obtaining highly optimised solutions. In particular, a variable angle tow composite wingbox has been successfully optimised, confirming that the procedure is well-suited for designing full-scale structures.

BIBLIOGRAPHY

[1] W. Koiter, *On the stability of elastic equilibrium*. Techische Hooge School at Delft, english transl. nasa tt-f10, 883 (1967) and affdl-tr70-25 (1970) ed., 1945.

[2] E. Barbero, L. Godoy, and I. Raftoyiannis, "Finite elements for three-mode interaction in buckling analysis," *International Journal for Numerical Methods in Engineering*, vol. 39, no. 3, pp. 469–488, 1996.

[3] R. Casciaro, G. Salerno, and A. Lanzo, "Finite element asymptotic analysis of slender elastic structures: A simple approach," *International Journal for Numerical Methods in Engineering*, vol. 35, no. 7, pp. 1397–1426, 1992.

[4] E. Riks, "An incremental approach to the solution of snapping and buckling problems," *International Journal of Solids and Structures*, vol. 15, no. 7, pp. 529–551, 1979.

[5] G. Garcea, A. Bilotta, A. Madeo, and R. Casciaro, *Direct evaluation of the post-buckling behavior of slender structures through a numerical asymptotic formulation*. Springer Verlag, 2014.

[6] E. J. Barbero, E. K. Dede, and S. Jones, "Experimental verification of buckling-mode interaction in intermediate-length composite columns," *International Journal of Solids and Structures*, vol. 37, no. 29, pp. 3919 – 3934, 2000.

[7] G. Raju, Z. Wu, S. White, and P. M. Weaver, "Optimal postbuckling design of variable angle tow composite plates," *AIAA Journal*, vol. 56, pp. 2045 – 2061, 2018.

[8] E. Barbero, A. Madeo, G. Zagari, R. Zinno, and G. Zucco, "Imperfection sensitivity analysis of laminated folded plates," *Thin-Walled Structures*, vol. 90, pp. 128 – 139, 2015.

[9] C. Thill, J. Etches, I. Bond, K. Potter, and P. Weaver, "Morphing skins," *The Aeronautical Journal (1968)*, vol. 112, no. 1129, p. 117–139, 2008.

[10] A. Madeo, R. Groh, G. Zucco, P. Weaver, G. Zagari, and R. Zinno, "Postbuckling analysis of variable-angle tow composite plates using Koiter's approach and the finite element method," *Thin-Walled Structures*, vol. 110, pp. 1–13, 2017.

[11] K. Sze, W. Chan, and T. Pian, "An eight-node hybrid-stress solid-shell element for geometric non-linear analysis of elastic shells," *International Journal for Numerical Methods in Engineering*, vol. 55, no. 7, pp. 853–878, 2002.

[12] J. A. Cottrell, T. J. R. Hughes, and Y. Bazilevs, *Isogeometric Analysis: Toward Integration of CAD and FEA*. 2009.

[13] J. Caseiro, R. Valente, A. Reali, J. Kiendl, F. Auricchio, and R. Alves de Sousa, "Assumed natural strain NURBS-based solid-shell element for the analysis of large deformation elasto-plastic thin-shell structures," *Computer Methods in Applied Mechanics and Engineering*, vol. 284, pp. 861–880, 2015.

[14] D. Magisano, L. Leonetti, and G. Garcea, "Advantages of the mixed format in geometrically nonlinear analysis of beams and shells using solid finite elements," *International Journal for Numerical Methods in Engineering*, vol. 109, no. 9, pp. 1237–1262, 2017.

[15] G. Garcea, G. Salerno, and R. Casciaro, "Extrapolation locking and its sanitization in Koiter's asymptotic analysis," *Computer Methods in Applied Mechanics and Engineering*, vol. 180, no. 1-2, pp. 137–167, 1999.

[16] D. Magisano, L. Leonetti, and G. Garcea, "How to improve efficiency and robustness of the Newton method in geometrically non-linear structural problem discretized via displacement-based finite elements," *Computer Methods in Applied Mechanics and Engineering*, vol. 313, pp. 986 – 1005, 2017.

[17] D. Magisano, L. Leonetti, and G. Garcea, "Koiter asymptotic analysis of multilayered composite structures using mixed solid-shell finite elements," *Composite Structures*, vol. 154, pp. 296–308, 2016.

[18] V. Oliveri, G. Zucco, D. Peeters, G. J. Clancy, R. Telford, M. Rouhi, C. McHale, R. M. O'Higgins, , T. M. Young, and P. M. Weaver, "Design, Manufacture, and Test of an In Situ Consolidated Carbon-Fiber-Reinforced Polyether Ether Ketone Variable-Stiffness Unitized Wingbox ," *AIAA Journal*, 2019.

[19] Z. Wu, G. Raju, and P. M. Weaver, “Postbuckling analysis of variable angle tow composite plates,” *International Journal of Solids and Structures*, vol. 50, no. 10, pp. 1770 – 1780, 2013.

[20] C. H. Thai, H. Nguyen-Xuan, S. P. A. Bordas, N. Nguyen-Thanh, and T. Rabczuk, “Isogeometric Analysis of Laminated Composite Plates Using the Higher-Order Shear Deformation Theory,” *Mechanics of Advanced Materials and Structures*, vol. 22, no. 6, pp. 451–469, 2015.

[21] Y. Guo and M. Ruess, “A layerwise isogeometric approach for NURBS-derived laminate composite shells,” *Composite Structures*, vol. 124, pp. 300 – 309, 2015.

[22] A. Eriksson, C. Pacoste, and A. Zdunek, “Numerical analysis of complex instability behaviour using incremental-iterative strategies,” *Computer Methods in Applied Mechanics and Engineering*, vol. 179, no. 3, pp. 265 – 305, 1999.

[23] M. Deml and W. Wunderlich, “Direct evaluation of the ‘worst’ imperfection shape in shell buckling,” *Computer Methods in Applied Mechanics and Engineering*, vol. 149, no. 1, pp. 201 – 222, 1997. Containing papers presented at the Symposium on Advances in Computational Mechanics.

[24] R. Groh, D. Avitabile, and A. Pirrera, “Generalised path-following for well-behaved nonlinear structures,” *Computer Methods in Applied Mechanics and Engineering*, vol. 331, pp. 394 – 426, 2018.

[25] S. White and P. Weaver, “Towards imperfection insensitive buckling response of shell structures-shells with plate-like post-buckled responses,” *Aeronautical Journal*, vol. 120, no. 1224, pp. 233–253, 2016.

[26] S. White, G. Raju, and P. Weaver, “Initial post-buckling of variable-stiffness curved panels,” *Journal of the Mechanics and Physics of Solids*, vol. 71, pp. 132 – 155, 2014.

[27] K. Liang, M. Ruess, and M. Abdalla, “The Koiter-Newton approach using von Karman kinematics for buckling analyses of imperfection sensitive structures,” *Computer Methods in Applied Mechanics and Engineering*, vol. 279, pp. 440–468, 2014.

[28] K. Liang, M. Abdalla, and Z. Gürdal, “A Koiter-Newton approach for nonlinear structural analysis,” *International Journal for Numerical Methods in Engineering*, vol. 96, no. 12, pp. 763–786, 2013.

[29] G. Zagari, A. Madeo, R. Casciaro, S. De Miranda, and F. Ubertini, "Koiter analysis of folded structures using a corotational approach," *International Journal of Solids and Structures*, vol. 50, no. 5, pp. 755–765, 2013.

[30] E. Barbero, A. Madeo, G. Zagari, R. Zinno, and G. Zucco, "Koiter asymptotic analysis of folded laminated composite plates," *Composites Part B: Engineering*, vol. 61, pp. 267–274, 2014.

[31] T. Rahman and E. Jansen, "Finite element based coupled mode initial post-buckling analysis of a composite cylindrical shell," *Thin-Walled Structures*, vol. 48, no. 1, pp. 25–32, 2010.

[32] T. Rahman, S. Ijsselmuiden, M. Abdalla, and E. Jansen, "Postbuckling analysis of variable stiffness composite plates using a finite element-based perturbation method," *International Journal of Structural Stability and Dynamics*, vol. 11, no. 4, pp. 735–753, 2011.

[33] A. D. Lanzo, G. Garcea, and R. Casciaro, "Asymptotic post-buckling analysis of rectangular plates by HC finite elements," *International Journal for Numerical Methods in Engineering*, vol. 38, no. 14, pp. 2325–2345, 1995.

[34] T. Rahman and E. Jansen, "Finite element based coupled mode initial post-buckling analysis of a composite cylindrical shell," *Thin-Walled Structures*, vol. 48, no. 1, pp. 25–32, 2010.

[35] F. Flores and L. Godoy, "Elastic post-buckling analysis via finite element and perturbation techniques. Part 1: Formulation," *International Journal for Numerical Methods in Engineering*, vol. 33, no. 9, pp. 1775–1794, 1992.

[36] E. Barbero, I. Raftoyiannis, and L. Godoy, "Finite elements for post-buckling analysis. II-Application to composite plate assemblies," *Computers and Structures*, vol. 56, no. 6, pp. 1019–1028, 1995.

[37] E. Boutyour, H. Zahrouni, M. Potier-Ferry, and M. Boudi, "Asymptotic-numerical method for buckling analysis of shell structures with large rotations," *Journal of Computational and Applied Mathematics*, vol. 168, no. 1-2, pp. 77–85, 2004.

[38] N. Silvestre and D. Camotim, "Asymptotic-numerical method to analyze the postbuckling behavior, imperfection-sensitivity, and mode interaction in frames," *Journal of Engineering Mechanics*, vol. 131, no. 6, pp. 617–632, 2005.

[39] B. Schafer and L. Graham-Brady, “Stochastic post-buckling of frames using Koiter's method,” *International Journal of Structural Stability and Dynamics*, vol. 6, no. 3, pp. 333–358, 2006.

[40] H. Chen and L. Virgin, “Finite element analysis of post-buckling dynamics in plates-Part I: An asymptotic approach,” *International Journal of Solids and Structures*, vol. 43, no. 13, pp. 3983–4007, 2006.

[41] N. L. Rizzi, V. Varano, and S. Gabriele, “Initial postbuckling behavior of thin-walled frames under mode interaction,” *Thin-Walled Structures*, vol. 68, pp. 124 – 134, 2013.

[42] G. Garcea, “Mixed formulation in Koiter analysis of thin-walled beams,” *Computer Methods in Applied Mechanics and Engineering*, vol. 190, no. 26-27, pp. 3369–3399, 2001.

[43] R. Casciaro, “Computational Asymptotic Post-Buckling Analysis of Slender Elastic Structures,” *CISM Courses and Lectures NO. 470*, p. ., 2005.

[44] A. D. Lanzo and G. Garcea, “Koiter's analysis of thin-walled structures by a finite element approach,” *International Journal for Numerical Methods in Engineering*, vol. 39, no. 17, pp. 3007–3031, 1996.

[45] G. Garcea, L. Leonetti, D. Magisano, R. Gonçalves, and D. Camotim, “Deformation modes for the post-critical analysis of thin-walled compressed members by a Koiter semi-analytic approach,” *International Journal of Solids and Structures*, vol. 110-111, pp. 367–384, 2017.

[46] G. Garcea, A. Madeo, and R. Casciaro, “The implicit corotational method and its use in the derivation of nonlinear structural models for beams and plates,” *J. Mech. Mater. Struct.*, vol. 7, no. 6, pp. 509–539, 2012.

[47] G. Garcea, A. Madeo, and R. Casciaro, “Nonlinear FEM analysis for beams and plate assemblages based on the implicit corotational method,” *J. Mech. Mater. Struct.*, vol. 7, no. 6, pp. 539–574, 2012.

[48] G. Garcea, A. Madeo, G. Zagari, and R. Casciaro, “Asymptotic post-buckling FEM analysis using corotational formulation,” *International Journal of Solids and Structures*, vol. 46, no. 2, pp. 377–397, 2009.

[49] G. Garcea, G. Trunfio, and R. Casciaro, “Mixed formulation and locking in path-following nonlinear analysis,” *Computer Methods in Applied Mechanics and Engineering*, vol. 165, pp. 247–272, NOV 2 1998.

[50] G. Garcea, G. A. Trunfio, and R. Casciaro, "Path-following analysis of thin-walled structures and comparison with asymptotic post-critical solutions," *International Journal for Numerical Methods in Engineering*, vol. 55, no. 1, pp. 73–100, 2002.

[51] R. Peek and M. Kheyrkhahan, "Postbuckling behavior and imperfection sensitivity of elastic structures by the Lyapunov-Schmidt-Koiter approach," *Computer Methods in Applied Mechanics and Engineering*, vol. 108, no. 3-4, pp. 261–279, 1993.

[52] G. Zagari, G. Zucco, A. Madeo, V. Ungureanu, R. Zinno, and D. Dubina, "Evaluation of the erosion of critical buckling load of cold-formed steel members in compression based on Koiter asymptotic analysis," *Thin-Walled Structures*, vol. 108, pp. 193–204, 2016.

[53] G. Garcea, F. S. Liguori, L. Leonetti, D. Magisano, and A. Madeo, "Accurate and efficient a posteriori account of geometrical imperfections in Koiter finite element analysis," *International Journal for Numerical Methods in Engineering*, vol. 112, no. 9, pp. 1154–1174, 2017. nme.5550.

[54] S. Klinkel, F. Gruttmann, and W. Wagner, "A robust non-linear solid shell element based on a mixed variational formulation," *Computer Methods in Applied Mechanics and Engineering*, vol. 195, no. 1-3, pp. 179–201, 2006.

[55] M. Schwarze and S. Reese, "A reduced integration solid-shell finite element based on the EAS and the ANS concept—Geometrically linear problems," *Computer Methods in Applied Mechanics and Engineering*, no. 80, pp. 1322–1355, 2009.

[56] L. Vu-Quoc and X. G. Tan, "Optimal solid shells for non-linear analyses of multilayer composites. I Statics," *Computer Methods in Applied Mechanics and Engineering*, vol. 192, no. 9-10, pp. 975–1016, 2003.

[57] Q. Li, Y. Liu, Z. Zhang, and W. Zhong, "A new reduced integration solid-shell element based on EAS and ANS with hourglass stabilization," *International Journal for Numerical Methods in Engineering*, pp. 1885–1891, 2015.

[58] K. Sze, "Three-dimensional continuum finite element models for plate/shell analysis," *Prog. Struct. Engng. Mater*, vol. 4, pp. 400–407, 2002.

[59] S. Klinkel, F. Gruttmann, and W. Wagner, "Continuum based three-dimensional shell element for laminated structures," *Computers and Structures*, vol. 71, no. 1, pp. 43–62, 1999.

[60] M. Schwarze and S. Reese, "A reduced integration solid-shell finite element based on EAS and the ANS concept: Large deformation problems," *International Journal for Numerical Methods in Engineering*, no. 85, pp. 289–329, 2011.

[61] K. Sze and A. Ghali, "Hybrid hexahedral element for solids, plates, shells and beams by selective scaling," *International Journal for Numerical Methods in Engineering*, vol. 36, no. 9, pp. 1519–1540, 1993.

[62] L. Vu-Quoc and X. Tan, "Efficient Hybrid-EAS solid element for accurate stress prediction in thick laminated beams, plates, and shells," *Computer Methods in Applied Mechanics and Engineering*, vol. 253, pp. 337–355, 2013.

[63] K. Sze, X. Liu, and S. Lo, "Hybrid-stress six-node prismatic elements," *International Journal for Numerical Methods in Engineering*, vol. 61, no. 9, pp. 1451–1470, 2004.

[64] K. Sze and L. Yao, "A hybrid stress ANS solid-shell element and its generalization for smart structure modelling. Part I - Solid-shell element formulation," *International Journal for Numerical Methods in Engineering*, vol. 48, no. 4, pp. 545–564, 2000.

[65] T. H. H. Pian and C.-C. Wu, *Hybrid and Incompatible Finite Element Methods*. New-York: Chapman & All, CRC, 1969.

[66] K. Sze, S.-J. Zheng, and S. Lo, "A stabilized eighteen-node solid element for hyperelastic analysis of shells," *Finite Elements in Analysis and Design*, vol. 40, no. 3, pp. 319–340, 2004.

[67] V. P. Nguyen, C. Anitescu, S. P. Bordas, and T. Rabczuk, "Isogeometric analysis: An overview and computer implementation aspects," *Mathematics and Computers in Simulation*, vol. 117, pp. 89 – 116, 2015.

[68] K. A. Johannessen, "Optimal quadrature for univariate and tensor product splines," *Computer Methods in Applied Mechanics and Engineering*, vol. 316, pp. 84 – 99, 2017. Special Issue on Isogeometric Analysis: Progress and Challenges.

[69] C. Adam, T. Hughes, S. Bouabdallah, M. Zarroug, and H. Maitournam, "Selective and reduced numerical integrations for NURBS-based isogeometric analysis," *Computer Methods in Applied Mechanics and Engineering*, vol. 284, pp. 732–761, 2015.

[70] G. Garcea, R. Gonçalves, A. Bilotta, D. Manta, R. Bebiano, L. Leonetti, D. Magisano, and D. Camotim, "Deformation modes of thin-walled members: A comparison between the method of generalized eigenvectors and generalized beam theory," *Thin-Walled Structures*, vol. 100, pp. 192–212, 2016.

[71] R. Echter, B. Oesterle, and M. Bischoff, "A hierarchic family of isogeometric shell finite elements," *Computer Methods in Applied Mechanics and Engineering*, vol. 254, pp. 170–180, 2013. cited By 61.

[72] R. Bouclier, T. Elguedj, and A. Combescure, "Efficient isogeometric NURBS-based solid-shell elements: Mixed formulation and B-method," *Computer Methods in Applied Mechanics and Engineering*, vol. 267, pp. 86–110, 2013. cited By 20.

[73] J. F. Caseiro, R. A. F. Valente, A. Reali, J. Kiendl, F. Auricchio, and R. J. Alves de Sousa, "On the Assumed Natural Strain method to alleviate locking in solid-shell NURBS-based finite elements," *Computational Mechanics*, vol. 53, no. 6, pp. 1341–1353, 2014.

[74] W. T. Les Piegl, *The NURBS book*. 1997.

[75] M. L. Bucalem and K.-J. Bathe, "Higher-order MITC general shell elements," *International Journal for Numerical Methods in Engineering*, vol. 36, no. 21, pp. 3729–3754, 1993.

[76] S. Hosseini, J. J. C. Remmers, C. V. Verhoosel, and R. de Borst, "An isogeometric solid-like shell element for nonlinear analysis," *International Journal for Numerical Methods in Engineering*, vol. 95, no. 3, pp. 238–256, 2013.

[77] R. Hauptmann and K. Schweizerhof, "A systematic development of 'solid-shell' element formulations for linear and non-linear analyses employing only displacement degrees of freedom," *International Journal for Numerical Methods in Engineering*, vol. 42, no. 1, pp. 49–69, 1998.

[78] K. Sze, X. Liu, and S. Lo, "Popular benchmark problems for geometric nonlinear analysis of shells," *Finite Elements in Analysis and Design*, vol. 40, no. 11, pp. 1551 – 1569, 2004.

[79] S. Henrichsen, P. Weaver, E. Lindgaard, and E. Lund, "Post-buckling optimization of composite structures using Koiter's method," *International Journal for Numerical Methods in Engineering*, 2016.

[80] S. G. Castro, R. Zimmermann, M. A. Arbelo, and R. Degenhardt, "Exploring the constancy of the global buckling load after a critical geometric imperfection level in thin-walled cylindrical shells for less conservative knock-down factors," *Thin-Walled Structures*, vol. 72, pp. 76 – 87, 2013.

[81] D. Magisano, K. Liang, G. Garcea, L. Leonetti, and M. Ruess, "An efficient mixed variational reduced-order model formulation for nonlinear analyses of elastic shells," *International Journal for Numerical Methods in Engineering*.

[82] P. Dinis and D. Camotim, "Post-buckling behaviour and strength of cold-formed steel lipped channel columns experiencing distortional/global interaction," *Computers and Structures*, vol. 89, no. 3-4, pp. 422–434, 2011.

[83] P. B. Dinis and D. Camotim, "Cold-formed steel columns undergoing local-distortional coupling: Behaviour and direct strength prediction against interactive failure," *Computer & Structures*, vol. 147, pp. 181–208, JAN 15 2015.

[84] R. Khakimova, C. J. Warren, R. Zimmermann, S. G. P. Castro, M. A. Arbelo, and R. Degenhardt, "The single perturbation load approach applied to imperfection sensitive conical composite structures," *Thin-Walled Structures*, vol. 84, pp. 369–377, NOV 2014.

[85] S. G. P. Castro, R. Zimmermann, M. A. Arbelo, R. Khakimova, M. W. Hilburger, and R. Degenhardt, "Geometric imperfections and lower-bound methods used to calculate knock-down factors for axially compressed composite cylindrical shells," *Thin-Walled Structures*, vol. 74, pp. 118–132, JAN 2014.

[86] M. A. Arbelo, R. Degenhardt, S. G. P. Castro, and R. Zimmermann, "Numerical characterization of imperfection sensitive composite structures," *Composite Structures*, vol. 108, pp. 295–303, FEB 2014.

[87] R. Casciaro, G. Garcea, G. Attanasio, and F. Giordano, "Perturbation approach to elastic post-buckling analysis," *Computers & Structures*, vol. 66, no. 5, pp. 585–595, 1998.

[88] D. Dubina and V. Ungureanu, "Instability mode interaction: From Van der Neut model to ECBL approach," *Thin-Walled Structures*, vol. 81, pp. 39–49, 2014.

[89] K. Ikeda and K. Murota, "Asymptotic and probabilistic approach to buckling of structures and materials," *Applied Mechanics Reviews*, vol. 61, pp. 040801 – 040801–16, 2008.

[90] C. Kassapoglou, "Design and analysis of composite structures," *John Wiley and Sons*, vol. Ltd.

[91] A. Cooper, "Trajectorial fiber reinforcement of composite structures," *Department of Mechanical and Aerospace Engineering, Washington University*, 1972.

[92] Z. Gurdal and R. Olmedo, "In-plane response of laminates with spatially varying fiber orientations - variable stiffness concept," *AIAA Journal*, vol. 31, no. 4, pp. 751–758, 1993.

[93] Z. Gürdal, B. Tatting, and C. Wu, "Variable stiffness composite panels: Effects of stiffness variation on the in-plane and buckling response," *Composites Part A: Applied Science and Manufacturing*, vol. 39, no. 5, pp. 911 – 922, 2008.

[94] S. Setoodeh, M. M. Abdalla, S. T. IJsselmuiden, and Z. Gürdal, "Design of variable-stiffness composite panels for maximum buckling load," *Composite Structures*, vol. 87, no. 1, pp. 109 – 117, 2009.

[95] Z. Wu, P. M. Weaver, G. Raju, and B. C. Kim, "Buckling analysis and optimisation of variable angle tow composite plates," *Thin-Walled Structures*, vol. 60, no. Supplement C, pp. 163 – 172, 2012.

[96] G. Raju, Z. Wu, B. C. Kim, and P. M. Weaver, "Prebuckling and buckling analysis of variable angle tow plates with general boundary conditions," *Composite Structures*, vol. 94, no. 9, pp. 2961 – 2970, 2012.

[97] B. H. Coburn, Z. Wu, and P. M. Weaver, "Buckling analysis of stiffened variable angle tow panels," *Composite Structures*, vol. 111, no. Supplement C, pp. 259 – 270, 2014.

[98] G. Raju, Z. Wu, and P. M. Weaver, "Buckling and postbuckling of variable angle tow composite plates under in-plane shear loading," *International Journal of Solids and Structures*, vol. 58, pp. 270 – 287, 2015.

[99] L. Leonetti, F. Liguori, D. Magisano, and G. Garcea, "An efficient isogeometric solid-shell formulation for geometrically nonlinear analysis of elastic shells," *Computer Methods in Applied Mechanics and Engineering*, vol. 331, pp. 159–183, 2018.

[100] M. A. Albazzan, R. Harik, B. F. Tatting, and Z. Gürdal, "Efficient design optimization of nonconventional laminated composites using lamination

parameters: A state of the art," *Composite Structures*, vol. 209, pp. 362 – 374, 2019.

[101] M. Montemurro and A. Catapano, "On the effective integration of manufacturability constraints within the multi-scale methodology for designing variable angle-tow laminates," *Composite Structures*, vol. 161, pp. 145 – 159, 2017.

[102] S. Daghighi, M. Rouhi, G. Zucco, and P. M. Weaver, "Bend-free design of ellipsoids of revolution using variable stiffness composites," *Composite Structures*, p. 111630, 2019.

[103] F. S. Liguori, A. Madeo, D. Magisano, L. Leonetti, and G. Garcea, "Post-buckling optimisation strategy of imperfection sensitive composite shells using Koiter method and Monte Carlo simulation," *Composite Structures*, vol. 192, pp. 654 – 670, 2018.

[104] F. S. Liguori, G. Zucco, A. Madeo, D. Magisano, L. Leonetti, G. Garcea, and P. M. Weaver, "Postbuckling optimisation of a variable angle tow composite wingbox using a multi-modal koiter approach," *Thin-Walled Structures*, vol. 138, pp. 183 – 198, 2019.

[105] S. R. Henrichsen, P. M. Weaver, E. Lindgaard, and E. Lund, "Post-buckling optimization of composite structures using Koiter's method," *International Journal for Numerical Methods in Engineering*, vol. 108, no. 8, pp. 902–940, 2016. nme.5239.

[106] Z. Wu, G. Raju, and P. M. Weaver, "Optimization of postbuckling behaviour of variable thickness composite panels with variable angle tows: Towards "buckle-free" design concept," *International Journal of Solids and Structures*, 2017.

[107] G. Clancy, D. Peeters, Vincenzo, D. Jones, R. M. O'Higgins, and P. M. Weaver, "A study of the influence of processing parameters on steering of carbon fibre/peek tapes using laser-assisted tape placement," *Composites Part B: Engineering*, 2018.

[108] D. M. Peeters, S. Hesse, and M. M. Abdalla, "Stacking sequence optimisation of variable stiffness laminates with manufacturing constraints," *Composite Structures*, vol. 125, pp. 596 – 604, 2015.

[109] D. M. Peeters, G. G. Lozano, and M. M. Abdalla, "Effect of steering limit constraints on the performance of variable stiffness laminates," *Computers & Structures*, vol. 196, pp. 94 – 111, 2018.

[110] T. R. Brooks and J. R. Martins, "On manufacturing constraints for tow-steered composite design optimization," *Composite Structures*, vol. 204, pp. 548 – 559, 2018.

[111] R. L. Riche and R. T. Haftka, "Optimization of laminate stacking sequence for buckling load maximization by genetic algorithm," *AIAA Journal*, 1993.

[112] E.Barkanov, O.Ozolins, E.Eglitis, F.Almeida, M.C.Bowering, and G.Watson, "Optimal design of composite lateral wing upper covers. Part I: Linear buckling analysis," *Aerospace Science and Technology*, vol. 38, no. Supplement C, pp. 1 – 8, 2014.

[113] X.-S. Yang, "Nature-inspired metaheuristics algorithm," *Luniver press, Frome, UK*, 2010.

[114] S. L. Tilahun and H. C. Ong, "Prey-predator algorithm: A new metaheuristic algorithm for optimization problems," *International Journal of Information Technology & Decision Making*, vol. 14, p. 1331–1352, 2015.

[115] M. Dorigo and C. Blumb, "Ant colony optimization theory: A survey," *Theoretical Computer Science*, vol. 344, pp. 243 – 278, 2005.

[116] K. Kameyama, "Particle swarm optimization-a survey," *IEICE Transactions on Information and Systems*, vol. 7, p. 1354–1361, 2009.

[117] Z. B. Zabinsky, *Random Search Algorithms*. John Wiley & Sons, Inc., 2010.

[118] K. Deep, K. P. Singh, M. Kansal, and C. Mohan, "A real coded genetic algorithm for solving integer and mixed integer optimization problems," *Applied Mathematics and Computation*, vol. 212, no. 2, pp. 505 – 518, 2009.

[119] K. Deb, "An efficient constraint handling method for genetic algorithms," *Computer Methods in Applied Mechanics and Engineering*, vol. 186, no. 2, pp. 311 – 338, 2000.

[120] Z. Wu, G. Raju, and P. M. Weaver, "Framework for the buckling optimization of variable-angle tow composite plates," *AIAA Journal*, vol. 53, pp. 3788 – 3804, 2015.

[121] D. C. Bloomfield M.W and W. P.M, "On feasible regions of lamination parameters for lay-up optimization of laminated composites," *Proc. R. Soc. A*, vol. 465, 2008.

[122] T. Macquart, V. Maes, M. T. Bordogna, A. Pirrera, and P. Weaver, "Optimisation of composite structures – enforcing the feasibility of lamination parameter constraints with computationally-efficient maps," *Composite Structures*, vol. 192, pp. 605 – 615, 2018.

[123] K. Svanberg, "The method of moving asymptotes—a new method for structural optimization," *International Journal for Numerical Methods in Engineering*, vol. 24, no. 2, pp. 359–373, 1987.

[124] J. R. R. A. Martins, P. Sturdza, and J. J. Alonso, "The complex-step derivative approximation," *ACM Trans. Math. Softw.*, vol. 29, pp. 245–262, Sept. 2003.

[125] T. M. Young, "Performance of the jet transport airplane: analysis methods, flight operations and regulations," *Wiley*, 2017.

[126] G. Zucco, V. Oliveri, D. Peeters, R. Telford, G. J. Clancy, C. McHale, M. Rouhi, R. M. O'Higgins, and P. M. Weaver, "Static test of a thermoplastic compositewingbox under shear and bending moment," *2018 AIAA/ASCE/AHS/ASC Structures, Structural Dynamics, and Materials Conference*, 2018.

[127] L. Leonetti, D. Magisano, F. Liguori, and G. Garcea, "An isogeometric formulation of the Koiter's theory for buckling and initial post-buckling analysis of composite shells," *Computer Methods in Applied Mechanics and Engineering*, vol. 337, pp. 387 – 410, 2018.